PURPLE OF CASSIUS: NANO GOLD OR COLLOIDAL GOLD?

Fathi Habashi[a]

Keywords: Zsigmondy; Stannous chloride; Aqua Regia; Swedish chemists; Thomas Graham; Ultramicroscope.

The purple pigment that is used in colouring molten glass and porcelain known as Purple of Cassius discovered in the 17th century was found by Richard Zsigmondy in 1897 to consist of nano gold with stannic oxide. The preparation of this material involves gold being dissolved in aqua regia, then reacted with a solution of tin(II) chloride. The tin(II) chloride reduces the dissolved gold to elemental gold supported on tin dioxide to give a purple precipitate which is thermally stable and is used as a pigment to give purple colour to glass and porcelain.

*
Corresponding Authors
E-Mail: Fathi.Habashi@arul.ulaval.ca
[a] Department of Mining, Metallurgical, and Materials Engineering, Laval University, Quebec City, Canada

INTRODUCTION

In the 1650's Andreas Cassius a chemist in Hamburg, Germany discovered a purple pigment that can be used in colouring glass and porcelain (Figure 1). It was prepared by adding a solution of stannous chloride to a dilute gold chloride solution. The precipitate was known as Purple of Cassius and was applied in the most famous glass and porcelain factories of Europe in Meissen in Saxony and in Sèvre in France.

Figure 1. Museum pieces of glass coloured with Purple of Cassius

That compounds of gold could impart a red colour to glass had been known for many centuries. Egyptian manuscripts from the Greco-Roman era make reference to it. The great metallurgist Georgius Agricola (1494-1555) knew of it, as did Paracelsus von Hohenheim (1493-1541), in the first half of the sixteenth century, while Benvenuto Cellini (1500-1571) at about the same time refers to a transparent red enamel discovered by an alchemist who was also a goldsmith. Andreas Libavius (*ca.* 1540-1616) the German alchemist who wrote the first text-book of chemistry, *Alchemia,* in 1597 knew also about the purple pigment.

In 1650 few years before Cassius publication Johann Rudolph Glauber (1604-1670) described the purple color of a gold pigment. Another distinguished contemporary alchemist Johann Kunckel (1630-1703) (Figure 2) who was well familiar with the glass technology of his time and in 1678 and was given charge of a glass factory at Potsdam in Germany.

Figure 2. Johann Kunckel (1630-1703)

He produced many products of ruby glass between 1679 and 1689. He published his *Ars Vitraria Experimentalis, oder Vollkommene Glasmacherkunst.* This work remained a standard treatise on glass technology for many years, and it is here that are found references to the production of ruby glass by the use of the purple precipitate described later by Cassius.

ANDREAS CASSIUS

There were two Andreas Cassius: the father (1605-1673) and the son (1645- *ca* 1700). It is quite possible that the elder did devise a process for making the purple precipitate and it was his son who wrote *De Auro* (Figure 3) in which he described the procedure but in the book he made no mention of his father. The full title reads: "Thoughts Concerning That Last and Most Perfect Work of Nature and Chief of Metals, Gold, Its Wonderful Properties, Generation, Affections, Effects and Fitness for the Operations of Art; Illustrated by Experiments".

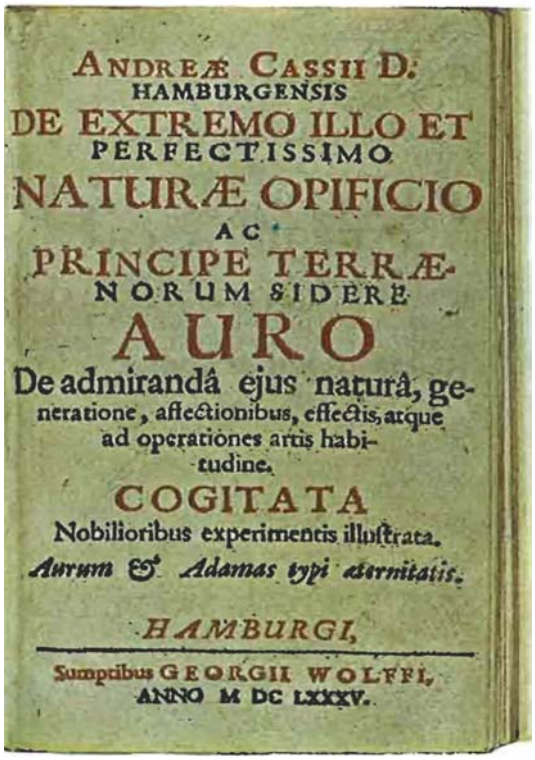
ANDREÆ CASSII D.
HAMBURGENSIS
DE EXTREMO ILLO ET
PERFECTISSIMO
NATURÆ OPIFICIO
AC
PRINCIPE TERRÆ-
NORUM SIDERE
AURO
De admirandâ ejus naturâ, ge-
neratione, affectionibus, effectis, atque
ad operationes artis habi-
tudine,
COGITATA
Nobilioribus experimentis illustrata.
Aurum & Adamas typi æternitatis.
HAMBURGI,
Sumptibus GEORGII WOLFFI,
ANNO M DC LXXXV.

Figure 3. *De Auro* by Andreas Cassius in 1685

LATER WORK

Swedish chemists

The Swedish chemist Carl Wilhelm Scheele (1742-1786) observed that when MnO_2 is dissolved in hydrochloric acid a red color is formed which when diluted precipitates the black MnO_2. The Swedish chemist Jöns Jakob Berzelius (1779-1848) described the yellow colour obtained by passing hydrogen sulfide into arsenious acid. He mentioned that the coloured solution should probably be regarded as a suspension of arsenic sulfide because it settled out. Other examples like the formation of colloidal sulfur when H_2S reacts with SO_2, etc.

Faraday

Michael Faraday (1791-1867) (Figure 4) spent much time in the mid 1850s investigating the properties of light and matter. He made several hundred gold slides and examined them by shining light through them. To make the gold leaf thin enough to be transparent, however, Faraday had to use chemical means rather than mechanical: commercial gold leaf was made by hammering the metal into very thin sheets but this was too thick for his purposes. Part of this process involved washing the films of gold, which Faraday noticed produced a faint ruby coloured fluid.

Figure 4. Michael Faraday (1791-1867)

Figure 5. Thomas Graham(1805-1869)

He shined a beam of light through the liquids and observed a cone was well defined in the fluid by the illuminated particles.

He realized that this cone effect was made because the fluid contained suspended gold particles that were too small to see with the scientific apparatus of the time but which scattered the light. He noted the light scattering properties from suspended small gold particles. It is because of this discovery that Faraday is seen as one of the first researchers into nano science and nano technology.

Graham

Thomas Graham (1805-1869) (Figure 5), Professor of chemistry at University College in London, realized in 1861 that some solutions were different: when the suspended materialdid not precipitate and could not pass through parchment filters. With diffusion rates much slower than normal, Graham suggested these peculiar solutions must consist of larger particles, inventing the terms 'sol' and 'colloid' to describe them. Colloid comes from Greek *Κόλλα* means glue.

Tyndall

British scientist John Tyndall (1820-1893) (Figure 6) described in 1869 light scattering by particles in a colloidal solution. Figure 7 shows light beam passing through a normal solution [right] and then passing through a colloidal solution where scattering is observed.

Figure 6. John Tyndall(1820-1893)

Zsigmondy

The nature and constitution of Purple of Cassius presented scientists with a problem which, throughout the whole of the nineteenth century, was attacked by some of the most distinguished chemists of the time. The formation of the purple precipitate was used to test for trace amounts of gold in solution. Richard Zsigmondy (1865-1929) (Figure 8) a Hungarian chemist in the Austrian Empire also prepared red colloidal gold solutions by the reduction of gold chloride with formaldehyde in a weakly alkaline solution.

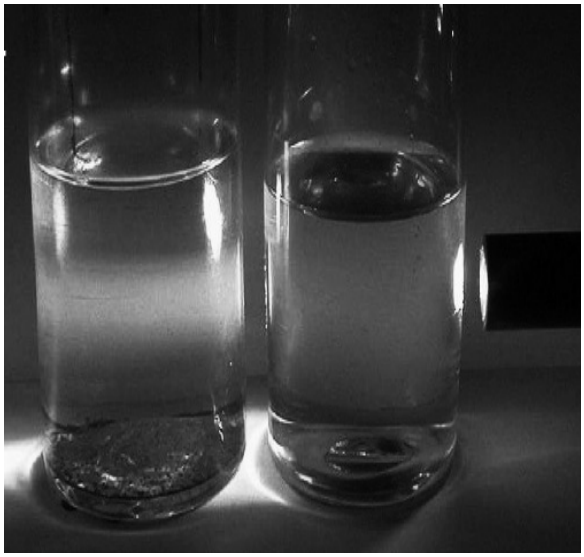

Figure 7. Tyndall effect: scattered light in the colloidal solution to the left

In his own words it was a clear solution like red wine. In dialysis experiments, however, they behaved like colloidal solutions, i.e., gold particles did not pass through the parchment membrane. Blue colloidal gold could also be obtained from dilute gold chloride solution by reduction with hydrazine or hydroxylamine.

Figure 8. Richard Zsigmondy (1865-1929)

It was Zsigmondy, who had spent some years studying gold colours and had joined the Schott Glassworks in Jena in 1897, developed the ultramicroscope (Figure 9) for the examination of colloids. He showed that the *Purple of Cassius* consisted of very finely divided gold with stannic oxide and that a mixture is capable of behaving like a chemical compound. For this investigation, he was awarded the Nobel Prize in Chemistry in 1925.

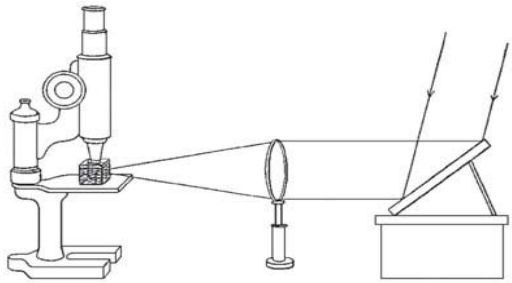

Figure 9. The ultramicroscope: illuminating colloidal particles from the side scatters light, making them visible

The reaction taking place is an oxidation-reduction process:

$$Au^{3+} + 3e^- \rightarrow Au$$

$$Sn^{2+} \rightarrow Sn^{4+} + 2e^-$$

and the overall reaction is

$$2Au^{3+} + 3Sn^{2+} \rightarrow 2Au + 3Sn^{4+}$$

In addition to the precipitation of ultra fine gold particles, the hydrolysis and the precipitation of stannic oxide in the reaction mixture

$$Sn^{4+} + 2H_2O \rightarrow SnO_2 + 4H^+$$

is essential for stabilizing the colloidal gold. The purple precipitate is then used in colouring porcelain or glass.

CONCLUSIONS

Colloidal solutions are heterogeneous in nature and are closely related to nano chemistry. They consist of particles between 40 and 900 nanometers in a liquid too small to be visible to the naked eye or through conventional microscopes. On the other hand nano particles are between 1 and 100 nm in size and may be in colloidal suspension or in the solid state. They are smaller than the wavelength of visible light which is 400 - 700 nm (Figure 10).

Materials change as their size approaches the nano scale mainly due to their large surface area. They often possess unexpected optical properties. Gold colloidal solution appears deep-red to blue in solution depending on their size (Figure 11).

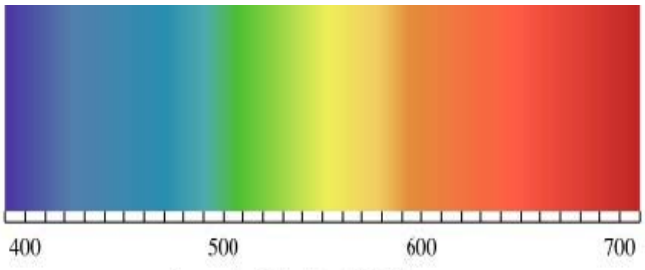

Figure 10. Wave length of visible light

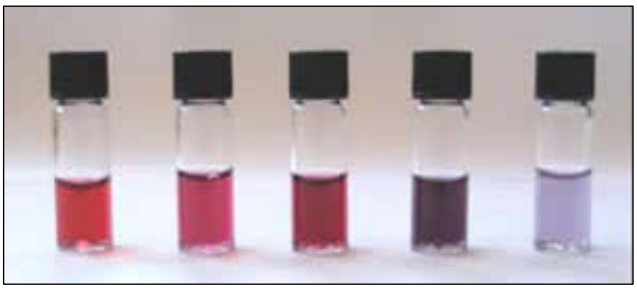

Figure 11. Effect of particle size on nanogold**.** Particle size increasesfrom left to right [https://en.wikipedia.org/wiki/Colloidal_gold]

Purple of Cassius are nano gold particles supported on colloidal tin oxide and is capable of coloring glass and porcelain deep red in color although gold is yellow in color.

Recently, gold nano particles are utilized in organic photo voltaics, sensory probes, therapeutic agents, drug delivery in biological and medical applications, electronic conductors, and catalysis.

ACKNOWLEDGEMENT

This paper has been presented at the 4th International Conference “Nanotechnologies”, October 24 – 27, 2016, Tbilisi, Georgia (Nano – 2016).

REFERENCES

[1]Hunt, L. B., *Gold Bull.,* **1976**, *9(4)*, 134-139

[2]Zsigmondy, R. A. and Thiessen, P. A.,*Das Kolloide Gold,***1925**

[3]Zsigmondy, R. A., “Properties of Colloids", *Nobel Lectures, Chemistry 1922-1941,* Elsevier, Amsterdam **1966**

Received: 04.11.2016.
Accepted: 26.11.2016.

TRIBOCHEMISTRY VERSUS NANO-TRIBOLOGY I. THEORETICAL CONSIDERATIONS ON MAKING A TANDEM NANOSCOPE

K. P. Thiessen[a]

Keywords: tribochemistry, nanoscope, SPM, AFM, STM.

Previous tribochemical studies showed that the high activation energy of reactions between solids covered by mechanical energy has not exclusively be thermally origined as that had been adopted formerly. For studying of tribochemical elemental effects, some theoretical considerations of combination atomic force microscope (AFM) and scanning tunneling microscope (STM) techniques using one dual tip cantilever have been discussed to develop a solid baseto make experimental setup called *Tandem Nanoscope.*

* Corresponding Authors
E-Mail: thiessenkarsten@gmail.com
[a] Hochschule für Technik und Wirtschaft Berlin, University of Applied Sciences, Berlin, Germany

Introduction

Tribochemistry is a branch of chemistry dealing with the chemical and physico-chemical changes of solids due to the influence of mechanical energy.[1-12] Nano-tribology is a branch of tribology dealing with friction and wear processes in nanometer scale using scanning probe microscopy (SPM) methods.

The most fascinating discovery of tribochemical studies performed worldwide in the last decades was that the high activation energy of reactions occuring between solids and covered by mechanical energy do not exclusively originate from thermal sources as that had been adopted formerly. In order to study the elements of these tribochemical effects, some theoretical considerations of combination atomic force microscope (AFM) and scanning tunneling microscope (STM) techniques using one dual tip cantilever have been discussed in order to develop a solid base to make experimental setup called *Tandem NanoScope*. The article here present these theoretical considerations and conclusions about making possibility of a *Tandem nanoscope*.

Tribochemistry

Definitions

Tribochemical synthesis, sometimes called mechanosynthesis including the current state of the art, as well as opportunities and challenges to it becoming a mainstream synthetic technique. It nowadays covers industrial aspects, inorganic materials, cocrystals, pharmaceutical applications, organic synthesis, discrete metal complexes, extended metal-organic materials[13] (MOFs) and has very close connections to nanotechnologies

Mechanical activation of chemical reactions

The general course of mechanically activated chemical reactions, observed in many experiments, for instance in a ball mill, can be described by following principal diagram:

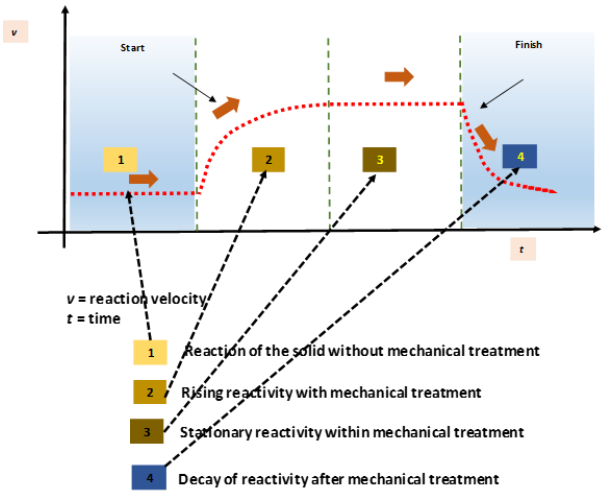

Figure 1. The course of tribochemical reactions[3]

At the beginning there is the low, only thermally activated reactivity, followed by the rising activity with mechanical treatment arriving to a stationary high level. Subsequent to the mechanical treatment there is decay of the reaction velocity and after treatment remains the state of the so called mechanically activated solid at some higher level.

There are tribochemical reactions with positive affinity, which are thermally activated reactions, as for instance HgS (Cinnabar) decomposition by trituration in a Cu mortar by a Cu pestle with a little amount of acetic acid producing elemental mercury [ancient Greece 400 BC].

$$HgS + Cu + (E_{mech}) \rightarrow Hg + CuS \ (\Delta G \text{ is negative}) \quad (1)$$

There are also tribochemical reactions with negative affinity, that are non-thermally activated reactions, such as milling of rocksalt (NaCl) in presence of Hg produces elemental sodium (as amalgam) and chlorine.[12]

$$NaCl+(x+1)Hg+(E_{mech}) \rightarrow$$

$$NaHg_x + HgCl_2\,(\Delta G \text{ is positive}) \qquad (2)$$

One can see that for a set of tribochemical reactions in "statu deformandi" (in time of mechanical activation) it can be said that characteristically they are proceeding whilst producing non-equlibrium negative affinities (Table 1).

Table 1. Some Tribochemical reactions with negative affinity (positive free enthalpy)[7]

No.	Reaction	A_{298K} kJ mol^{-1}
1	$BaO_2 \rightarrow BaO + ½\ O_2$	-55.2
2	$SiC + 2H_2 \rightarrow Si + CH_4$	-58.9
3	$C + 2H_2O \rightarrow CO_2 + 2H_2$	-62.4
4	$2Cu + CO_2 \rightarrow 2CuO + C$	-140.2
5	$Au + ¾\ CO_2 \rightarrow 1/2Au_2O_3 + ¾C$	-311.5
6	$Fe_3O_4 + 2C \rightarrow 2CO_2 + 3Fe$	-330.2
7	$2MgO + C \rightarrow CO_2 + Mg$	-744.9

In the mechanically induced electrochemical deposition of metals without external current, contrary to the electromotive series, the "Tribogalvanic Effect" has a minimal affinity of -300 kJ mol^{-1}.[14] It has been shown that the negative affinity of tribochemical reactions does not decrease with rising temperature, as it might be expected, but increases instead (Table 2).

Table 2. Temperature dependence of the *negative*affinity for twotribochemial oxidation reactions of coppercalculated by the 1st UHLICH approximation

	Basic Affinity, A^0_T kJ. mol^{-1}		
Temperature	**298K**	**1000K**	**2000K**
$4Cu+CO_2 \rightarrow 2Cu_2O+C$	101.7	199.6	342.3
$2Cu+CO_2 \rightarrow 2CuO+C$	138.9	271.1	466.1

The experimental results suggest that a common thermal activation can be excluded with high probability. Following the principle of least contradictions the hypothesis of the "Magma-Plasma-Model" was developed.[3] The "Magma-Plasma-Model" proposes that local temperatures greater than 10^4 K in ultra-short-time can be generated at mechanical impact points, associated with transient (tribo-) plasmas and the ejection of energetic species including free electrons.[14]

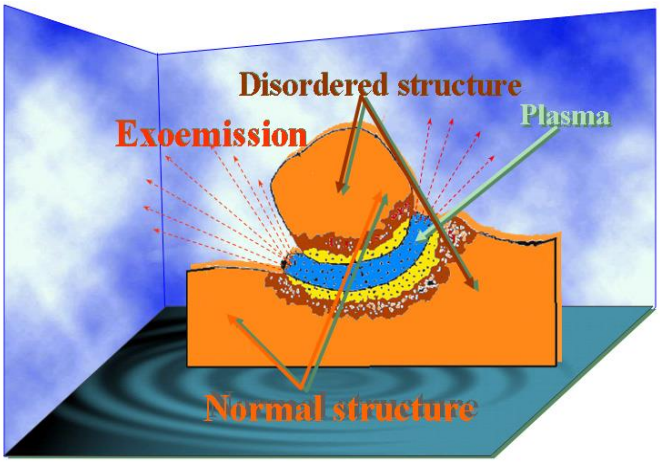

Figure 2. Magma Plasma Model (MPM) „Triboplasmas"

The energetic relaxation of triboplasmas was described by the following stages.

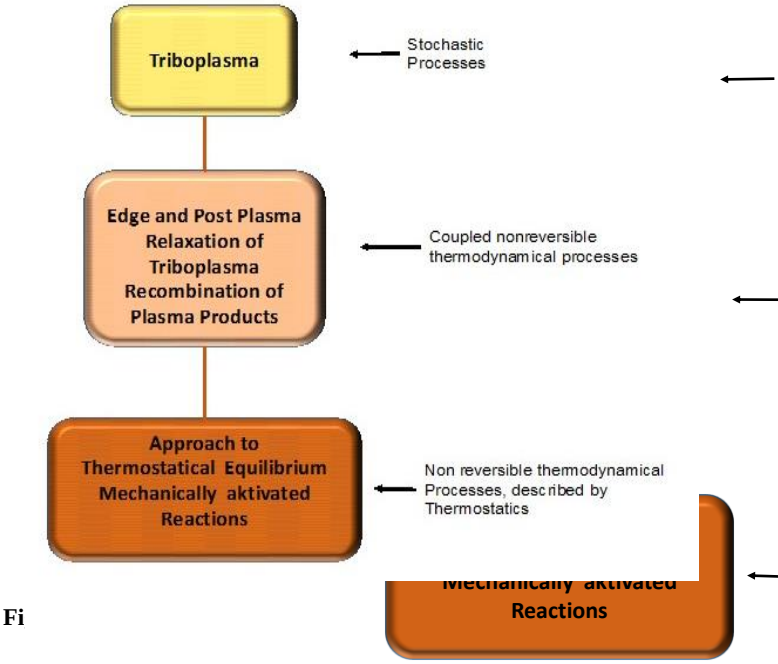

Fi

Scanning Probe Microscopy (SPM) for Nano-Tribochemisty

There are many universal scanning probe microscopes combining the use of AFM or STM.[13] Precisely such types of nano-analytical devices appear to be useful for the examination of elemental effects of tribochemical reactions. For this purpose a device must be designed, which can generate a tribochemical reaction "just in time" and observe directly possible magma plasmas or their relaxation processes respectively.

The idea is to use simultaneously an atomic force microscope (AFM) for the nano-tribological impacting of a metallic surface and a scanning tunnelling microscope (STM) for the examination of tribochemical reactions with atomic scale resolution.

Tandem Nanoscope

How should such a dual function device be designed? There must be a dual tip cantilever, where one tip will function as AFM that is touching the metallic surface and generating the tribomechanical action under the required circumstances. This tip must be electrically insulating. The other tip, being electrically conductive, does not touch the surface to be examined. It serves as STM analyzing the physical and chemical conversions with atomic resolution.

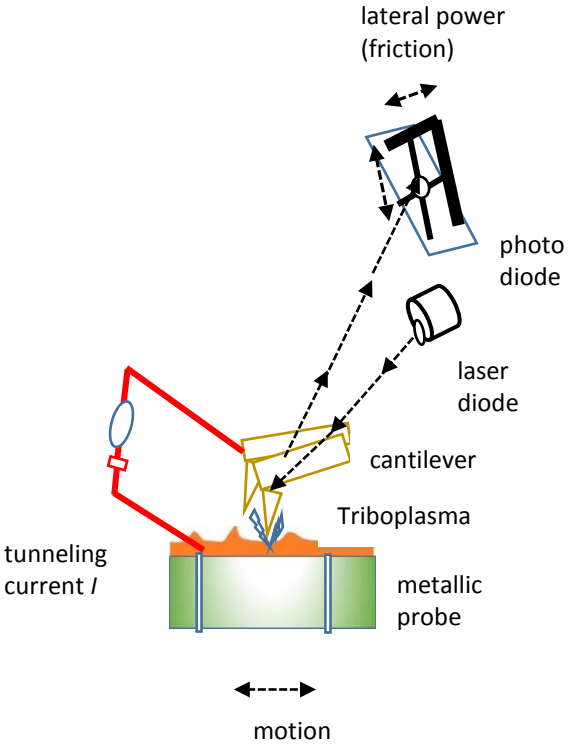

Figure 3. Tandem Nanoscope.

The device called by us **"Tandem NanoScope"**. A functional sketch with a dual tip cantilever is follows:

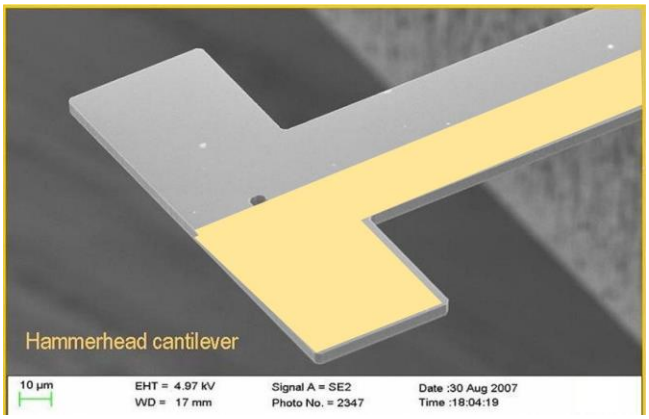

Figure 4. „Hammerhead" cantilever - NIST

The dual tip device may look as shown below using an idea from the National Institute of Standards NIST, a so called "Hammerhead". One tip serves as AFM, touching the sample surface, the other tip, coated with gold and moving in some nanometer distance to the surface will be the "watching" STM.

Discussion

The principle of "Tandem Nanoscope" opens new perspectives to scanning probe microscopes with novel abilities for direct watching of tribochemical reactions, maybe also triboplasmas, with atomic resolutions and opens a way before building it experimentally.

Acknowledgement

This paper has been presented at the 4th International Conference "Nanotechnologies", October 24 – 27, 2016, Tbilisi, Georgia (Nano – 2016).

References

[1]Carey-Lea, M.,*Phil. Mag*., **1893**, *36*, 350-351

[2]Bushan,B.,*Wear*, **2005**, *259(7)*, 1507 -153

[3]Heinicke G., *Tribochemistry*, Akademie-Verlag Berlin**1984**; (Preface P.A. Thiessen)

[4]Garkunov, D.N.,*The selective transport effect at points of friction* (Moscow, **1985**, in Russian)

[5]Thiessen, P.A., Meyer, K., Heinicke, G.,*Grundlagen der Tribochemie*, Akademie-Verlag Berlin,**1967**, 7-22

[6]Thiessen, K.P.,*Z. Chem*., **1976**, *16*, 1-9

[7]Thiessen, K.P.,*J. Chim. Phys*., **1986**, *63*, 717

[8]Bottomley, L.A., *Anal.Chem.*,**1998**, *70*, 425R-475R

[9]Bushan, B., Int. Mat. Rev.,**1999**, 105-117

[10]Jacobs, T. Gotsman, B. Lantz M.A. and Carpick, R., *Tribol. Lett*.,**2010**, *39(3)*, 257 -271

[11]Kajdas, C.K., *Tribology Int*., **2005**, *38(3)*, 2005, 337–353

[12]Thiessen, K..P., Mber. dtsch. Akad. Wiss.,**1968**, *10*, 200

[13]James,S.L. Adams, C.J., Bolm, C., Braga, D., Collier, P., Friscic, T., Grepioni F., Harris, K.D.M., Hyett, G., Jones, W., Krebs, A., Mack,J. Maini, L., Orpen, A.G., Parkin, I.P., Shearouse, W.C., Steed,J.W., Waddell, D.C. L.,*Chem. Soc. Rev*., **2012**, *41*, 413–447

[14]Thiessen,K.P.,*Isv. Sib. Otdel. AN SSSR*, **1988**, *4*, 63

Received: 22.10.2016.
Accepted: 30.11.2016.

ECO-SAFE METHOD FOR PROCESSING OF TECHNOLOGICAL RESISTANT ANTHROPOGENIC MINERAL RESOURCE

Tsisana Gagnidze[a]* and Rusudan Chagelishvili[a]

Keywords: Electrochemical processing; gold-containing ores; flotation tails; barite-polymetallic.

The possibility of gold extraction from the concentrate obtained by secondary enrichment of flotation tails of Madneuli gold-containing barite-polymetallic ore has been studied. Such concentrate contains the gold in the mineral in finely-impregnated form and is considered as difficult-to-process material. It was shown that by the use of $Fe_2(SO_4)_3$ as an oxidizer in thiourea acidic solution, the concentrate preliminary milling and roasting at 400 ^{0}C is necessary for the 90 % extraction of gold. By electrochemical method, the 90 % extraction is reached at the system "soft" oxidation in the conditions of Red/Ox potential of 0.4 V in temperature range of 25-35 ^{0}C.

* Corresponding Authors
Phone: + 995 593 74 08 43
E-Mail: ts.gagnidze@mail.ru
[a] I. JavakhiSvili Tbilisi State University, R.Agladze Institute of Inorganic Chemistry and Electrochemistry, Georgia, Tbilisi, Mindeli str.11, 0182

INTRODUCTION

The problem of gold extraction from resistant anthropogenic mineral resources may be considered as the most important ones which face modern gold-mining industry. Complex multistage schemes of enriching of mentioned ores do not allow the extraction of the ultra-dispersed gold in full measure. Therefore, in the most cases such mineral resources cannot be processed economically and ecologically-acceptable criteria.

Among anthropogenic waste, the enriched tails of the majority of sulfide ores, as the source of noble metals, are of significant interest. Moreover, their storage has a severe impact to the environment. The flows of natural and artificial leaching appear in underground and surface water.

The problem of processing of the above-mentioned mineral resources is topical for Georgia also. In tailing dumps of Madneuli Mining-Processing Combine up to 120 million tons of anthropogenic mineral resource is collected among which up to 27 million tons are flotation tails of enriching of sulfide mineral (barite-polymetallic and chalcopyrite) which contain more than 10 tons of gold and up to 120 tons of silver. Processing of such mineral by profitable technology is a prospective problem and hence investigations in this direction is topical.

EXPERIMENTAL

The objects of our research were gold-containing flotation tails of processing of barite-polymetallic ore. They contain 0.5 and 1.8 g ton^{-1} of gold and silver respectively.

In addition, Cu, Zn, Pb, S, Fe, Cd and Al_2O_3 are also present in amounts varying from 0.02 to 1.7 %. These tails contain 80-90 % quartzite, 3-6 % barite, 3 % pyrite, 3 % alunite 22 % kaolin, 1 % sericite and 2-3 % iron hydroxides. On the basis of mineralogical composition of those tails the procedure for secondary flotation enriching was selected. Flotation was carried out at laboratory flotation machine of mechanical type and at the test bench of flotation machine. Flotation of primary tails of barite-polymetallic ore was carried out by technological scheme presented in figure 1.

The tails were crushed in a wet mill for 5 min at a ratio of L:S = 1:1. Thereafter the suspension was delivered to a flotation machine of mechanical type where the flotation was performed in a the presence of collector ,butyl xanthate (60 g ton^{-1}) and foaming agent T-80 (50 g ton^{-1}). Reagents were delivered twice, at beginning of the process and after 10 min. Flotation duration was18-20 min. Cleaning was performed by butyl xanthate (20 g ton^{-1}) and foaming agent T-80 (50 g ton^{-1}). Cleaned general concentrate was dried in a thermostat, crushed and sieved. Determination of elements concentration in enriching products was carried out by atomic absorption method. In table 1 the composition of secondary enriching flotation tails of barite polymetallic ore of Madneuli deposit is presented.

Table 1. Chemical composition of secondary concentrate of flotation tails of barite-polymetallic ore.

Au, g ton^{-1}	Ag	Zn %	Cu %	Fe %	S_{Tot} %	Sso_4 %	Ba, %
2.53	25.8	0.46	0.57	4.45	4.4	4.25	7.9

For gold extraction from flotation tails of secondary enriching of barite-polymetallic concentrate the researches were carried out by means of electro-chlorination and of chlorination by gaseous chlorine as well as by concentrate treatment by thiourea solutions.

RESULTS AND DISCUSSION

We have used electro-chlorination method earlier at processing of gold-containing secondary quartzite with gold extraction up to 85 %.[1] Advantages of this method lies in the fact that generation of the oxidant, chlorine, is performed directly in the process of concentrate leaching. In electro-chlorination an intensification of mineral opening is carried out at the expense of its dissolving in cracks and structural imperfections and oxidation of sulfide sulfur.

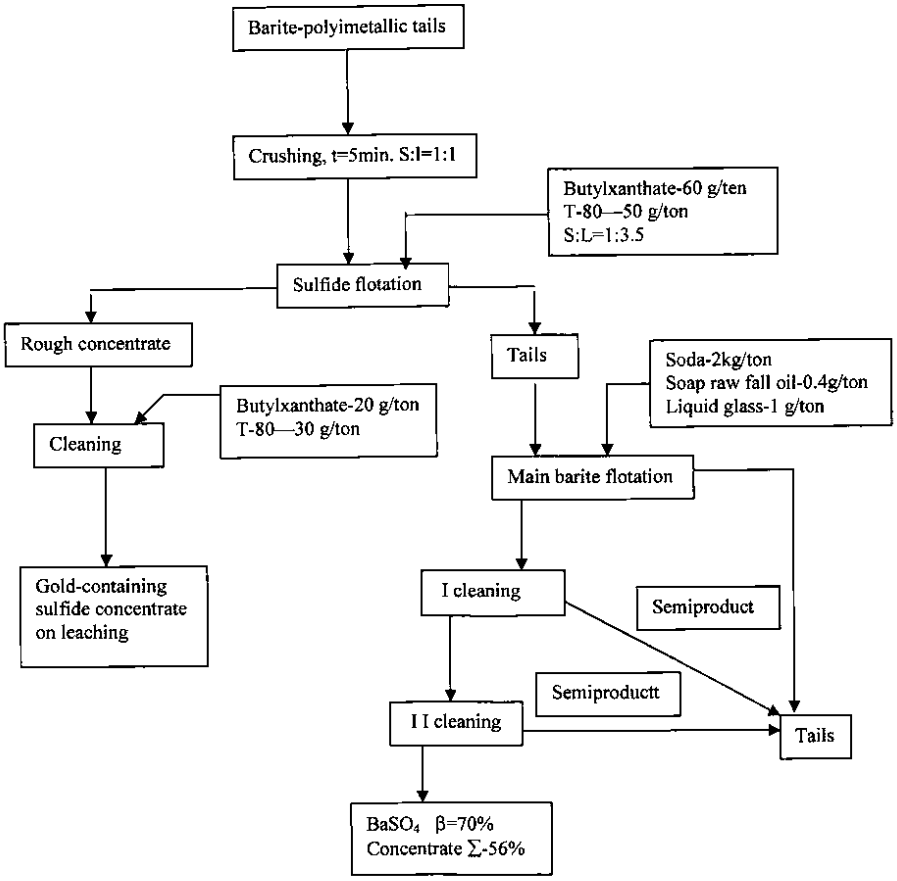

Figure 1. Scheme of flotation of primary tails of barite-polymetallic ore.

This process allows the access to deeply impregnated gold. The method was also tested at leaching of gold-containing concentrate of secondary enriching of barite tails. Their chemical composition is presented in table 1.

Electro-chlorination of the concentrate of the tails secondary enriching was performed by the procedure described previously for researches on treatment of gold-containing secondary quartzite.[1] The results are given in table 2.

As evident from table 2, leaching duration has no unambiguous regular effect on the process of extraction of gold and other components from the concentrate. The results remain within experimental reproducibility. Low gold extraction may be explained by incomplete opening of sulfide mineral. The comparison of the results obtained at leaching of mentioned concentrate by chlorination as well as by electro-chlorination methods are partly indicative of thereof (Table 3) .

As evident from table 3, five-hour chlorination treatment of enriching tails in acid solutions gives lesser gold extraction than electro-chlorination treatment in the same conditions. This difference is more appreciable in alkaline solutions.

As evident from the data of table 1, concentrate, obtained by enriching of tails of barite - polymetallic ore, contains all components practically only in the form of sulfates. It may be suggested that among them non-soluble sulfates (Ba, Ca etc.) may be also presented which do not interact with oxidants (including anode ones) as well as with acids, bases and which may cause the gold passivity.

Hence, obtained results show that concentrate of tails of barite-polymetallic ore belongs to the group of rather resistant minerals and gold extraction by chlorination and electro-chlorination methods doesn't exceed 40-50 % which is indicative of the limit of capability of those methods for concentrate of given type.

Table 2. Effect of duration of electro-chlorination leaching of concentrate of flotation tails of enriching of barite - polymetallic ore.

No.	Duration, h	Power consumption, A h^{-1}	Red/Ox potential, mV	Extraction degree of components, %				
				Au, g ton^{-1}	Ag, g ton^{-1}	Cu	Zn	Fe
1	2.5	8.15	675.0	48.5	61.0	61.0	58.0	46.0
2	2.5	5.32	880.0	-	57.0	38.0	36.0	42.0
3	5.0	10.75	688.0	40.6	57.0	43.0	40.0	38.0
4	5.0	11.5	805.0	48.5	57.0	46.0	48.0	42.0
5	8.0	22.33	855.0	54.4	65.0	67.0	69.0	38.0

Experimental conditions: electrolyte - NaCl-150 g L^{-1}; sample-200 g; temperature - 30 ^{0}C; pH - 0.5

Table 3. Chlorination and electro-chlorination treatment of concentrate of flotation tails of enriching of barite-polymetallic ore.

No.	Systems	Process	pH	Red/Ox, mV	Degree of component extraction, %				
					Au, g ton^{-1}	Ag, g ton^{-1}	Zn	Cu	Fe
1	NaCl+HCl	Electro-chlorination	0.5±0.05	1052±50	48.6	85.0	73.0	67.0	54.0
2	NaCl+HCl	Chlorination	0.5±0.05	1069±45	40.7	85.0	77.0	63.0	50.0
3	NaOCl	Electro-chlorination	11±0.05	663±45	58.0	96.0	73.0	27.0	25.0
4	NaCl+NaOH	Chlorination	11±0.05	683±35	31.0	70.0	75.0	14.0	17.0

Experiment duration 5 h, temperature 40 ^{0}C.

It is suggested that concentrate resistance is caused by physical depression of gold by non-soluble barium sulfates. For gold extraction from gold-containing concentrate of barite tails the researches were also carried out by means of thiocarbamide solutions. This method was tested by authors of the work at leaching of secondary quartzite and high degrees of gold extraction were obtained (83 %).[2] Researches, performed on thiocarbamide leaching of concentrate of barite tails at room temperature, did not give desired results. Gold extraction degree slightly increased in comparison with above-mentioned methods and comprised 66 %, but the index is as yet low. Preliminary leaching of concentrate by solution of sulfuric acid at 70-80 ^{0}C causes the increase of gold extraction degree only by 3-4 % and comprised 69.8 %.

Table 4. Effect of roasting temperature on gold extraction degree from concentrate of barite tails at pre-treatment and at no-treatment .

No.	Roasting temp., ^{0}C	Degree of gold extraction without pre-leaching by sulfuric acid, %	Degree gold extraction at pre-leaching by sulfuric acid, %
1	400	89.2	82.3
2	500	86.4	72.0
3	600	88.0	79.7
4	700	75.6	73.6
5	800	86.3	66.5

Experimental conditions: roasting duration 2 h, sample 20 g, leaching duration- 4 h, *S:L*=1:5, concentration: Thiourea 2 %, $Fe_2(SO_4)_3$ 1 %, H_2SO_4 1 %.

Table 5. Voltammetric characteristics of platinum electrode in various systems

No.	Current density mA cm^{-2}	Systems, Red/Ox, V		
		A	B	C
1	0	0.338	0.229	0.270
2	5	1.402	0.382	0.377
3	10	1.398	0.200	0.391
4	15	1.400	0.411	0.393
5	20	1.418	0.417	0.404
6	30	1.558	0.427	0.643
7	50	1.698	0.444	0.648

System A = 0.5 N KCl, B = 0.5 N KCl + 0.5 N Thiourea, C = 0.5 N KCl + 0.5 N Thiourea + 0.5 N HCl

Table 6. Electrochemical treatment of flotation concentrates of tails of barite- polymetallic ore

Parameter	Solution composition, g L^{-1}		
	KCl-100	KCl-100; urea - 15	KCl-100, thiourea - 18
Red/Ox, V	1.0 ± 0.15	1.0 ± 0.15	0.4 ± 0.04
Gold extraction degree, %	54.0	64.3	87.1

Experimental conditions: t – 25 ^{0}C; I_a - 0.75 A cm^{-2}; m - 200 g, duration 5 h.

Table 7. Electrochemical treatment of gravitational concentrates of chalcopyrite tails

No.	τ , h	*T*, ^{0}C	Red/Ox, V	Gold extraction degree, %
1	1.0	25.0	0.4 ± 0.04	30.0
2	3.0	25.0	0.4 ± 0.04	55.0
3	5.0	25.0	0.4 ± 0.04	86.0
4	5.0	30.0	0.4 ± 0.04	86.8
5	5.0	35.0	0.4 ± 0.04	87.4

Experimental conditions: KCl 100 g L^{-1}, Thiourea 18 g L^{-1}, I_a 0.75 A cm^{-2}, m 200 g.

For complete removal of physical and chemical depressants of gold the roasting of secondary concentrate at temperature range from 400 ^{0}C to 800 ^{0}C and cinder leaching by thiourea solution was performed. After concentrate roasting at 400 ^{0}C gold extraction increased to 89 % and at further temperature growth gold extraction degree is slightly reduced.

In following series roasted concentrate was treated by acid before thiourea leaching. Experimental results are presented in Table 4. As evident, gold extraction degree from concentrate, roasted at 400 ^{0}C, reduced and comprised 82.3 %. At further growth of temperature reduction of gold extraction degree is more appreciable, at 800 ^{0}C this value reduced to 66 %. Experimental results have shown that pre-treatment of cinder by acid is non-productive. Because of the fact that roasting of gold containing concentrate of barite tails at 400 ^{0}C gives the best results, in the following series of experiments roasting was carried out in temperature range from 350 ^{0}C to 500 ^{0}C at additional grinding of concentrate. Results have shown that after roasting at 400 ^{0}C and fine grinding of concentrate (0.16 mm) and cinder treatment by thiocarbamide solution, gold extraction degree is notably increases and attains 93.4 %. At temperatures of 350 ^{0}C, 450 ^{0}C and 500 ^{0}C this value is roughly same i.e. 88-89 %

Experimental results have shown that re-grinding and roasting of concentrate is reasonable for complete opening of gold surface which is favorable for efficiency of further operations of gold extraction. But the use of pre-treatment (grinding, roasting) of concentrate under study before leaching with further extraction of noble metals from the solution is associated with a high power consumption.

Therefore for simplification of technology of processing of resistant sulfide ores and concentrates and for elaboration of eco-safe and highly efficient method of their processing the two methods, electrochemical and thiourea one, were combined. From the viewpoint of electrochemical dissolution of metals the resistant sulfide ores must be considered as system of sulfides in which fine-dispersed gold is impregnated. At the action of electrochemical reactions the electronegative elements of this system will be dissolved primarily. As a result of electrochemical dissolution of sulfides in anode space the destruction of mineral structure and opening of fine-dispersed mineralization of gold proceeds. By selective complex formation with free thiourea, present in the electrolyte, gold will pass to the solution in the form of cation complex (eqn.1).

$$Au + 2H_2NC(S)NH_2 + HCl \rightarrow Au[H_2NC(S)NH_2]_2Cl + H^+ + e^- \quad (1)$$

At the cathode the complex discharges and precipitation of metal results. This method provides the electrochemical treatment of resistant sulfide mineral (in the form of suspension or pulp) in chloride electrolyte, containing organic ligand for complex formation, thiourea.[3,4] Variation of potentials at polarization of Pt - electrode in this solution is presented in Table 5.

Introduction of thiourea in chloride solution is favorable for reduction of system Red/Ox potential from 0.8-1.2 to 0.35-0.45 V (Table 6). In accordance with,[5] standard potential of reaction (eqn. 2).

$$2CS(NH_2)_2 \leftrightarrows 2CS(N_2H_3) + 2H^+ \quad (2)$$

is equal to + 0.42 V. Standard potentials of reactions,[6]

$$S^{2-} \rightarrow S + 2e^- \qquad E_0 = +0.006 \text{ V} \quad (3)$$

$$S_2^{2-} \rightarrow 2S + 2e^- \qquad E_0 = +0.476 \text{ V} \quad (4)$$

At the values of Red/Ox potentials of electrolyte systems under study (Table 5) passing of the following reactions is highly possible:

$$2CuS + 4HCl - 4e^- \rightarrow 2CuCl_2 + S_2 + 4H^+ \quad (5)$$

$$FeS_2 + 2HCl - 2e^- \rightarrow FeCl_2 + S_2 + 2H^+ \quad (6)$$

In Table 6 the results of the research of gold-containing concentrates of barite - polymetallic flotation by the use of various chloride systems are listed.

As evident, efficiency of gold extraction from given concentrate is attained only from electrolytes containing thiourea as a complex former. It also should be noted that electrochemical treatment of the 3-rd system was performed without ore pre-grinding and roasting of concentrate.

Similar results were obtained at electrochemical treatment of resistant gold-containing gravitational concentrates of chalcopyrite tails in mentioned systems (Table 7).

Conclusion

On the basis of results obtained, it may be concluded that resistant gold-containing flotation tails of enriched of barite-polymetallic ore may be efficiently processed by thiourea method (by grinding and pre-roasting of concentrate) with 94 % gold extraction as well as by electrochemical method (without grinding and pre-roasting of concentrate) with 90 % gold extraction. In the latter case an acid chloride electrode, pH 0.5-2 was used, containing 15-20 g L^{-1} of selective organic complexing agent for noble metals, thiourea.

The process takes place in the conditions of "soft" oxidation regime, Red/Ox = 0.38-0.42 V, without separation of molecular chlorine and without environmental contamination. It should be noted that the latter method is reassuring, therefore, further the researche will be continued in mentioned direction.

References

[1]Gvelesiani, J., Gagnidze, Ts. Mamporia, M., Adamia, T., *Sak. Mets. Akad. Matsne, Khimii ser*., **2006**, *32 (1-2)*, 167-175.

[2]Gvelesiani, G., Gaprindashvili, V., Mechurchlishvili, T., Shavgulidze, V., Chagelishvili, R., *Sak. Mets. Akad. Matsne. Khimii ser.*, **2000**, *25 (3-4)*, 315-328.

[3]Gagnidze, Ts., Gvelesiani, J., Mamporia, M., *Khsnari okroshemcveli sulfiduri nedleulis gadamushavebisatvis, Sakpatenti*, **2011**, 5220.

[4]Gagnidze, Ts., Chagelishvili, R., Khavtasi, N., Nadareishvili., M., International Scintific Conference, *Modern Res. Prospects Use Chem., Chem. Eng. Related Fields,* September, 21-23, **2016**, Ureki, Georgia.

[5]Preisler, P., *J. Am. Chem. Soc*., **1949**, *71*, 2840.

[6]Spravochnik Khimika, v.III. Izdat. ".Khimia". M., **1965**, 750.

Received: 01.11.2016.
Accepted: 02.12.2016.

SYNTHESIS AND ANTIMICROBIAL ACTIVITY OF IMINES AND THEIR METAL COMPLEXES

Ram U. Ambhure[a], Sunil R. Mirgane[b], Devidas U. Thombal[c],Suresh U. Shisodia[d], Sudam S. Pandule[d], László Kótai[e] and Rajendra P. Pawar[d]*

Keywords: Imines, metal complexes & microbial activity.

Two new schiff bases (*E*)-(4-chlorophenyl)-(4-chlorobenzylidene)acetohydrazide and *(E)*-(4-chlorophenyl)-(1-methoxynaphthalen-2-ylmethylene)acetohydrazide and their metal complexes were synthesized. All of the synthesized imines and their metal complexes were characterized and screened for antimicrobial activity.

* Corresponding Authors
E-Mail: rppawar@yahoo.com
Tel:+91-240-2334577
Fax: +91-240-2487284
[a] AAEFs College of Engineering, Pimple, Koregaon Bhima, Pune, Maharashtra, INDIA.
[b] Department of Chemistry, JES College, Jalna-431001, Maharashtra, INDIA.
[c] Department of Chemistry, LBS College, Partur-431501, Maharashtra, INDIA.
[d] Department of Chemistry, Deogiri College, Aurangabad-431005, Maharashtra, INDIA.
[e] Research Centre for Natural Sciences, Hungarian Academy of Sciences, Budapest, 1171, Magyar Tudósok krt. 2.

Introduction

Schiff bases, characterized by the azomethine group (–R-C=N–), form a significant class of compounds in medicinal and pharmaceutical chemistry and are known to have biological applications due to their antibacterial,[1-6] antifungal,[3-6] and antitumor[7,8] activity. Schiff base ligands are considered "privileged ligands" because they are easily prepared by the condensation between aldehydes and amines. The incorporation of transition metals into these compounds leads to the enhancement of their biological activities and decrease in the cytotoxicity of both metal ion and schiff base ligand.[9-11]

Schiff bases with donors (N, O, S, etc.) have structural similarities with neutral biological systems and due to presence of imine group are utilized in elucidating the mechanism of transformation of racemization reaction in biological system.[12-14]

Coordination chemistry, a study of metal complexes is an important research area in inorganic chemistry. Detail reviews regarding Schiff base metal complexes and their applications have been published by several scientist in recent years, Neelima Mishra et al.[15]and S. Arulmurugan et al.[16] on biological activities, Katarzyna Brodowska et al.[17] on using invarious fields of science, Ahmed M. Abu-Dief et al.[18] on versatile applications, and Kavita Rana et al.[19] on analgesic, anti-inflammatoryeffect.

Experimentals

Synthesis of Schiff base

In order to prepare Schiff base firstly esters of substituted phenylacetic acid were prepared, which were further reacted with hydrazine hydrate to obtain hydrazides from which Schiff base were prepared.

a) General procedure for the synthesis of esters

To a magnetically stirred ice cold solution of carboxylic acid (20 mmol) in methanol (20 mL), a catalytic amount of concentrated H_2SO_4 (2-3 drops) was added dropwise. The contents were gently warmed to room temperature and then refluxed for 2-3 h. After completion of the reaction as indicated by TLC (20% ethyl acetate: n-hexane); excess methanol was removed under reduced pressure on rotary evaporator. The reaction mixture was cooled to 0°C, basified with saturated aqueous $NaHCO_3$ and finally extracted with dichloromethane (3x15 mL). The combined organic layer was washed with water, separated, dried over sodium sulphate and concentrated on rotary evaporator to afford the corresponding esters as oily liquids.

b) General procedure for the synthesis of hydrazides

A mixture of carboxylic ester (20 mmol) and hydrazine hydrate (100 mmol) was refluxed at 100 °C for 1h. Progress of the reaction was monitored by TLC (50 % ethyl acetate: n-hexane).After completion of reaction; the excess amount of hydrazine hydrate was evaporated under reduced pressure. The crude product was triturated with petroleum ether under ice-cold condition, washed several times with water and dried by toluene azeotrope to get the corresponding hydrazide as the crystalline white solid.

c) General procedure for the synthesis of Schiff base

In equimolar mixture of aldehyde (2 mmol) and hydrazide (2 mmol) in ethanol (5 mL), 2-3 drops of glacial acetic acid were added at room temperature and the contents were refluxed till completion of reaction for appropriate time.

After completion of the reaction as monitored by TLC (3:7 ethyl acetate:n-hexane), excess of ethanol was evaporated on rotary evaporator and the contents of the flask poured over crushed ice. The solid obtained was filtered, washed with cold water, dried and finally recrystallized from chloroform: hexane (1:1).

Table 1. List of synthesized Schiff base ML_2 type metal complexes

	Schiff base aldehyde component, R=4-Cl	Metal	Time, h	Yield, %
A1	4-Cl-benzaldehyde	Zn	6.0	91
A2	4-Cl-benzaldehyde	Pd	6.5	87
A3	4-Cl-benzaldehyde	Co	7.5	81
A4	4-Cl-benzaldehyde	Cu	7.0	80
A5	4-Cl-benzaldehyde	Fe	6.0	84
A6	1-MeO-2-naphthaldehyde	Zn	6.5	89
A7	1-MeO-2-naphthaldehyde	Pd	6.0	82
A8	1-MeO-2-naphthaldehyde	Co	7.5	84
A9	1-MeO-2-naphthaldehyde	Cu	6.0	92
A10	1-MeO-2-naphthaldehyde	Fe	6.5	91

B) General procedure for preparation of Schiff bases metal-complexes

A mixture of Schiff bases (2 mmol) and nitrates of metal (1 mmol) in ethanol (5 ml) was refluxed for 6-8 hours. The pH of solution is adjusted to 7-8 by using alcoholic ammonia solution. The progress of reaction was monitored on thin layer chromatography (TLC) using petroleum ether: ethyl acetate (7:3 ml) eluent. The products were isolated after reduction of volume by evaporation. It was filtered, washed with ethanol, dried under vacuum and further recrystallized in ethanol. The reaction time and yield of complexes prepared are specified in Table 1.

Spectral analysis of Schiff bases

(4-Chlorophenyl)-(4-chlorobenzylidene)acetohydrazide

IR *v* max cm-1: 735, 812, 1012, 1087, 1140, 1296, 1393, 1491, 1612, 1668, 1896, 2862, 2966, 3083. ^{1}H NMR: δ 2.50 (s, 2H, Ar-CH_2-), δ 4.0 (b, 1H, -NH-N-), δ 7.30-7.80 (m, 8H, Ar-H), δ 8.0 (s, 1H, -N=CH). ^{13}C NMR: 40, 128.56, 128.86, 129.10, 129.35, 131.43, 131.79, 133.61, 134.64, 134.89, 135.03, 135.14, 145.81, 166.75, 172.47. EI-MS: 308.2 (M+, 65 %), 307.2 (80 %), 305.2 (100%).

(4-Chlorophenyl)-(1-methoxynaphthalen-2-ylmethylene)aceto-hydrazide

IR *v* max cm-1: 745, 806, 977, 1050, 1199, 1255, 1336, 1474, 1557, 1665, 2840, 3057, 3198. ^{1}H NMR: δ 2.52 (s, 3H, Ar-OCH_3), δ 3.90 (s, 2H, Ar-CH_2-), δ 4.2 (s, 1H, -NH-N-), δ 7.40-8.10 (m, 10H, Ar-H), δ 8.85 (s, 1H, -N=CH). ^{13}C NMR: 40, 57.13, 113.86, 124.40, 124.84, 125.49, 126.21, 127.59, 128.38, 129.211, 131.03, 132.54, 132.82, 133.12, 133.89, 135.04, 141.59, 158.05, 165.39, 170.95. EI-MS: 353 (M+, 45 %), 351.3 (100%).

Analysis of metal complexes

Characterization of all the prepared hydrazone-based Schiff base ligands complexes with metals Zn(II), Pd(II), Co(II), Cu(II), and Fe(II) were done. Their elemental analysis confirmed the ML_2 nature of complexes. The IR data of some complexes are given in the supplementary material.

Table 2. Anti-bacterial activity of ligand and complexes (in mm)

Compound	Inhibition zone, in mm		
	Escherichia coli	Bacillus subtilis	Pseudomonas aeruginosa
L1	14	20	17
L2	11	29	12
A1	21	25	20
A2	20	25	20
A3	18	20	17
A4	25	22	29
A5	19	26	18
A6	11	16	14
A7	19	22	18
A8	08	10	11
A9	24	31	27
A10	18	21	20
Penicillin	23	30	28

Antibacterial activity

Antibacterial activity of synthesized Schiff bases and their complexes has been screened against bacteria *Escherichia coli, Bacillus subtilis &Pseudomonasaeruginosa.* Results of the ligands and complexes prepared were showed moderate to excellent activity as compare to standard Penicillin Table 2.

Conclusion

In conclusion we synthesized novel Schiff bases and metal complexes.These ligands and metal complexes were screened for antibacterial activity. Ligand L2 showed good activity against *Bacillus subtilis.* Complex A1, A4 and A9 showed better activity against *Escherichia coli,* Bacillus *subtilis andPseudomonas aeruginosa*. All other compound were have variable but less than standard antibacterial activity.

Acknowledgment

The authors are thankful to the principal Dr. S. N. Thore, Deogiri College, Aurangabad for providing laboratory facilities and continue his encouragement during the said work.

References

[1]Abu-Hussen, A. A. A., *J. Coord. Chem.,***2006**, *59(2),* 157–176.

[2]Karthikeyan, M. S., Prasad, D. J., Poojary, B., Subrahmanya Bhat, K., Holla, B. S. and Kumari, N. S., *Bioorg. Med. Chem.,* **2006,** *14(22),* 7482–7489.

[3]Singh, K., Barwa, M. S. and Tyagi, P., *Eur. J. Med. Chem.,* **2006,** *41(1),* 147–153.

[4]Panneerselvam, P., Nair, R. R., Vijayalakshmi, G., Subramanian, E. H. and Sridhar, S. K., *Eur. J. Med. Chem.,***2005,** *40(2),* 225–229.

[5]Sridhar, S. K., Saravanan, M. and Ramesh, A., *Eur. J. Med. Chem.,,***2001,** *36(7-8),* 615–625.

[6]Pandeya, S. N., Sriram, D., Nath, G. and Declercq,E., *Eur. J.. Pharm. Sci.,* **1999,** *9(1),* 25–31.

[7]Mladenova, R., Ignatova, M., Manolova, N., Petrova, T. and Rashkov, I., *Eur. Polym. J.,* **2002,** *38(5),* 989–999.

[8]Walsh, O. M., Meegan, M. J., Prendergast, R. M. and Nakib, T. A., *Eur. J. Med. Chem.,* **1996,** *31(12),* 989–1000.

[9]Travnıcek, Z., Malon, M., Sindelar, Z., Dolezal, K., Rolcik, J., Krystof, V., Strnad, M., Marek, J., *J. Inorg. Biochem.,* **2001,** *84(1-2),* 23–32.

[10]El-Ayaan, U. and Abdel-Aziz, A. A. M., *Eur. J. Med. Chem.,* **2005,** *40(12),* 1214–1221.

[11]Sonmez, M., Berber, I. and Akbas, E., *Eur. J. Med. Chem.,* **2006,** *41(1),* 101–105.

[12]Keskioglu, E., Gunduzalp, A. B., Ete, S. C., Hamurcu, F. and Erk, B., *Spectrochimica Acta—Part A,* **2008,** *70(3),* 634–640.

[13]Wu, J. Z. and Yuan, L., *J. Inorg. Biochem.,* **2004,** *98(1),* 41–45.

[14]Balasubramanian, K. P., Parameswari, K., Chinnusamy, V., Prabhakaran, R. and Natarajan, K., *Spectrochim. Acta—Part A,* **2006,** *65(3-4),* 678–683.

[15]Mishra, N., Poonia, K., and Dinesh, K., *Int. J. Adv. Res. Technol.* (*IJOART*), **2013,** *2,* 52-66.

[16]Arulmurugan, S., Kavitha, H. P. and Venkatraman, B. R., *Rasayan J. Chem,* **2010,** *3,* 385-410.

[17]Brodowska , K., Łodyga-Chruścińska, E., *CHEMIK,* **2014,** *68*, 129-134.

[18]Ahmed, M., Ibrahim. A. D., Mohamed, M. A., *Beni-Suef Univ. J. Basic Appl. Sci.,* **2015,** *4,* 119-133.

[19]Rana, K., Pandurangan, A., Singh, N., Tiwari, A. K., *Int. J. Curr. Pharm. Res.,* **2012,** *4,* 5-11.

Received: 02.10.2016.
Accepted: 02.12.2016.

EXCHANGE SPATIAL-ENERGY INTERACTIONS

G. A. Korablev[a]*

Keywords: Lagrangian equations; wave functions; spatial-energy parameter; electron density; elementary particles; quarks.

The notion of spatial-energy parameter (*P*-parameter) is introduced based on the modified Lagrangian equation for relative motion of two interacting material points, and is a complex characteristic of important atomic values responsible for interatomic interactions and having the direct connection with electron density inside an atom. Wave properties of *P*-parameter are found, its wave equation having a formal analogy with the equation of ψ-function is given. With the help of *P*-parameter technique, numerous calculations of exchange structural interactions have been performed and the applicability of the model for the evaluation of the intensity of fundamental interactions has been demonstrated. Initial theses of quark screw model are also discussed.

* Corresponding Authors
E-Mail: korablevga@mail.ru

[a] Department of Physics, Izhevsk State Agricultural Academy

SPATIAL-ENERGY PARAMETER

When oppositely charged heterogeneous systems interact, a certain compensation of the volume energy takes place, which results in the decrease in the resultant energy e.g. during the hybridization of atom orbitals.[1] But this is not a direct algebraic deduction of corresponding energies. The comparison of numerous regularities of physical and chemical processes leads us to assume that in such and similar cases the principle of adding reverse values of volume energies or kinetic parameters of interacting structures are observed. For instance, during the ambipolar diffusion, when joint motion of oppositely charged particles is observed in the given medium (in plasma or electrolyte), the diffusion coefficient (*D*) is found as follows:

$$\frac{\eta}{D} = \frac{1}{a_+} + \frac{1}{a_-}$$

where

a_+ and a_- are the charge mobility of both atoms and η is the constant coefficient.

Total velocity of the topochemical reaction (υ) between the solid and gas is found as follows:

$$\frac{1}{v} = \frac{1}{v_1} + \frac{1}{v_2}$$

where

υ_1 is the diffusion velocity of the reagent and

υ_2 is the velocity of reaction between the gaseous reagent and solid.

Change in the light velocity (Δv) when moving from the vacuum into the given medium is calculated by the principle of algebraic deduction of reverse values of the corresponding velocities:

$$\frac{1}{\Delta v} = \frac{1}{v} - \frac{1}{c}$$

where c is the velocity light in vacuum.

Lagrangian equation for relative motion of the system of two interacting material points with masses m_1 and m_2 in coordinate x is as follows:

$$m_{\text{np}} x'' = \frac{\partial U}{\partial x} \qquad (1)$$

where

$$\frac{1}{m_{\text{r}}} = \frac{1}{m_1} + \frac{1}{m_2} \qquad (1a)$$

here U is the mutual potential energy of material points, m_r is the reduced mass and $x'' = a$ (characteristic of system acceleration).

For elementary interaction areas Δx, $\frac{\partial U}{\partial x} \approx \frac{\Delta U}{\Delta x}$ then

$$m_{\text{r}} a \Delta x = -\Delta U$$

$$\frac{1}{1/(a\Delta x)} \times \frac{1}{(1/m_1 + 1/m_2)} \approx \Delta U$$

or

$$\frac{1}{1/(m_1 a\Delta x) + 1/(m_2 a\Delta x)} \approx \Delta U$$

Since in its physical sense the product $m_i a \Delta x$ equals the potential energy of each material point ($-\Delta U_i$), then

$$\frac{1}{\Delta U} \approx \frac{1}{\Delta U_1} + \frac{1}{\Delta U_2} \qquad (2)$$

Thus the resultant energy characteristic of the interaction system of two material points is found by the principle of adding the reverse values of initial energies of interacting subsystems.

Therefore assuming that the energy of atom valence orbitals (responsible for interatomic interactions) can be calculated by the principle of adding the reverse values of some initial energy components, the introduction of *P*-parameter as the averaged energy characteristic of valence orbitals is postulated based on the following equations.

$$\frac{1}{q^2/r_\mathrm{i}} + \frac{1}{W_\mathrm{i} n_\mathrm{i}} = \frac{1}{P_\mathrm{E}} \tag{3}$$

$$\frac{1}{P_0} = \frac{1}{q^2} + \frac{1}{(Wrn)_\mathrm{i}} \tag{4}$$

$$P_\mathrm{E} = P_0/r_\mathrm{i} \tag{5}$$

here

W_i is the orbital energy of electrons,[2]

r_i is orbital radius of *i*–orbital,[3]

$q=Z^*/n^*$,[4,5]

n_i is the number of electrons of the given orbital,

Z^* and n^* are the effective charge of the nucleus and effective main quantum number, and

r is the bond dimensional characteristics.

The term P_0 will be called spatial-energy parameter (SEP), and e P_E as effective *P*–parameter (effective SEP). Effective SEP has a physical sense of some averaged energy of valence electrons in the atom and is measured in the energy units e.g., in electron-volts (eV).

Values of P_0-parameter are tabulated constant values for the electrons of the atom given orbital.

For the dimensionality, SEP can be written as follows:

$$[P_0] = [q^2] = [E] \times [r] = [h] \times [\upsilon] = \frac{kg\ m^3}{s^2} = Jm$$

where $[E]$, $[h]$ and $[\upsilon]$ are the dimensionalities of energy, Plank's constant and velocity respectively.

The introduction of *P*-parameter should be considered as further development of quasi-classic notions using quantum-mechanical data on the atom structure to obtain the energy conditions criteria of phase-formation. At the same time, for similarly charged systems (e.g. orbitals in the given atom) and homogeneous systems the principle of algebraic addition of these parameters will be preserved.

$$\sum P_\mathrm{E} = \sum (P_0/r_\mathrm{i}) \tag{6}$$

$$\sum P_\mathrm{E} = \frac{\sum P_0}{r} \tag{7}$$

$$\sum P_0 = P_0' + P_0'' + P_0''' + \cdots, \tag{8}$$

$$r \sum P_\mathrm{E} = \sum P_0 \tag{9}$$

Here *P*-parameters are summed for the valence orbitals of all atoms.

To calculate the values of P_E-parameter at the given distance from the nucleus either atomic radius (R) or ionic radius (r_i) can be used instead of r depending on the bond type.

Applying the equation (8) to hydrogen atom we can write down the following

$$K\left(\frac{e}{n}\right)_1^2 = K\left(\frac{e}{n}\right)_2^2 + mc^2\lambda \tag{10}$$

where e is the elementary charge, n_1 and n_2 are the main quantum numbers, m is the electron mass, c is the velocity of electromagnetic wave, λ is the wave length, K is a constant.

Using the known correlations $\nu = c/\lambda$ and $\lambda = h/mc$ (where h is Plank's constant, ν is the wave frequency) from the formula (10), the equation of spectral regularities in hydrogen atom can be obtained, in which $2\pi^2e^2/hc = K$.

EFFECTIVE ENERGY OF VALENCE ELECTRONS IN AN ATOM AND ITS COMPARISON WITH THE STATISTIC MODEL

The modified Thomas-Fermi equation, converted to a simple form by introducing dimensionless variables,[6] can be written as eqn. (11).

$$U = e(V_\mathrm{i} - V_0 + \tau_0^2) \tag{11}$$

where

V_0 is the countdown potential,

e is the elementary charge,

τ_0 is the exchange and correlation corrections,

V_i is the interatomic potential at the distance

r_i from the nucleus and

U is the total energy of valence electrons.

For some elements, the comparisons of the given value U with the values of P_E-parameter are given in Table 1.

As it is seen form the Table 1 the parameter values of U and P_E are practically the same (in most cases with the deviation not exceeding 1-2 %) without any transition coefficients. Multiple corrections introduced into the statistic model are compensated with the application of simple rules of adding reverse values of energy parameters, and SEP quite precisely conveys the known solutions of Thomas-Fermi equation for interatomic potential of atoms at the distance r_i from the nucleus. Namely the following equality takes place:

$$U = P_\mathrm{E} = e(V_\mathrm{i} - V_0 + \tau_0^2) \tag{12}$$

Using the known correlation[6] between the electron density (β_i) and interatomic potential (V_i) we have Eqn. (13).

Table 1. Comparison of total energy of valence electrons in atom calculated in Thomas-Fermi statistic atom model (*U*) and with the help of approximation.

Atom	Valence electrons	r_i (Å)	*X*	φ(X)	*U* (eV)	W_i(eV)	*n*	q^2(eV Å)	P_E (eV)
Ar	$3P^4$	0.639	3.548	0.09-	35.36-	12+	4	73.196	33.45
				0.084	33.02				
	$3S^2$	0.607	3.268	0.122-	47.81	34.8 (*t*)	2	96.107	48.44
				0.105	44.81	29.0	2	96.107	42.45
	$2P^4$	0.146	0.785	0.47	834.25	246	4	706.3	817.12
V	$4S^2$	1.401	8.508	0.0325	7.680	7.5	2	22.33	7.730
			8.23	0.0345	8.151				
Cr	$4S^2$	1.453	8.95	0.0295	7.013	7	2	23.712	7.754
			8.70	0.0313	7.440				
Mn	$4S^2$	1.278	7.76	0.0256	10.89	6.6 (*t*)	2	25.12	7.895
						7.5	2	25.12	10.87
Fe	$4S^2$	1.227	7.562	0.0282	8.598	8.00	2	26.57	9.201
						7.20 (*t*)	2	26.57	8.647
Co	$4S^2$	1.181	7.565	0.02813	9.255	8	2	27.98	10.062
			7.378	0.03075	10.127	7.5 (*t*)	2	27.98	9.187
Ni	$4S^2$	1.139	7.2102	0.02596	9.183	9	2	29.348	10.60
						7.7 (*t*)	2	29.348	9.640
Cu	$4S^2$	1.191	7.633	0.0272	9.530	7.7	2	30.717	9.639
In	$5S^2$	1.093	8.424	0.033	21.30	11.7	2	238.3	21.8
			8.309	0.03415	22.03*				
	$4d^{10}$	0.4805	3.704	0.106	155.6	20	10	258.23	145.8
Te	$5p^4$	1.063	8.654	0.0335	23.59	9.8	4	67.28	24.54
			8.256	0.0346	24.37*				
	$5S^2$	0.920	7.239	0.0326	26.54	19	2	90.577	27.41
			7.146	0.0341	27.72*	17	2	90.537	25.24

Note: (1) Bond energies of electrons W_i are obtained: "*t*" – theoretically (by Hartry-Fock method), "+" – by XPS method, all the rest – by he results of optic measurements; (2) "*" – energy of valence electrons (*U*) calculated without Fermi-Amaldi amendment.

$$\beta^{2/3}{}_i \approx (3e/5) \times (V_i - V_0);$$

$$\beta^{2/3}{}_i \approx Ae \times (V_i - V_0 + \tau^2{}_0) = [Ae \times r_i \times (V_i - V_0 + \tau^2{}_0)]/r_i \quad (13)$$

where A is a constant.

According to the Eqns. (12) and (13) we have the following correlation (Eqn. 14), setting the connection between P_0-parameter and electron density in the atom at the distance r_i from the nucleus.

$$\beta_i^{\frac{2}{3}} = \frac{AP_0}{r_i} \quad (14)$$

Since in the value $e(V_i - V_0 + \tau_0^2)$ in Thomas-Fermi model there is a function of charge density, P_0-parameter is a direct characteristic of electron charge density in atom.

This is confirmed by an additional check of equality correctness (14) using Clementi function.[7] A good correspondence between the values of β_i calculated via the value of P_0 and obtained from atomic functions is observed.

Wave equation of *P*-parameter

For the characteristic of atom spatial-energy properties two types of *P*-parameters with simple correlation between them are introduced, $P_E = P_0/R$, where R is the dimension characteristic of the atom. Taking into account additional quantum characteristics of the sublevels in the atom, this equation in coordinate x can be written down as follows:

$$\Delta P_E \approx \frac{\Delta P_0}{\Delta x}$$

or

$$\partial P_E \approx \frac{\partial P_0}{\partial x}$$

where

the value ΔP equals the difference between P_0-parameter of *i*-orbital and

P_{CD}–countdown parameter (parameter of basic state at the given set of quantum numbers).

According to the established rule[8] of adding *P*-parameters of similarly charged or homogeneous systems for two orbitals in the given atom with different quantum characteristics and in accordance with the law of energy conservation we have

$$\Delta P''_{\mathrm{E}} - \Delta P'_{\mathrm{E}} = P_{\mathrm{E},\lambda}$$

where $P_{E,\lambda}$ is the spatial-energy parameter of quantum transition.

Taking as the dimension characteristic of the interaction $\Delta\lambda=\Delta x$, we have

$$\frac{\Delta P''_0}{\Delta\lambda} - \frac{\Delta P'_0}{\Delta\lambda} = \frac{P_0}{\Delta\lambda} \text{ or } \frac{\Delta P'_0}{\Delta\lambda} - \frac{\Delta P''_0}{\Delta\lambda} = -\frac{P_0\lambda}{\Delta\lambda}$$

If we divide termwise by $\Delta\lambda$, we get

$$\frac{\left(\frac{\Delta P'_0}{\Delta\lambda} - \frac{\Delta P''_0}{\Delta\lambda}\right)}{\Delta\lambda} \sim \frac{d^2P_0}{\Delta\lambda^2}$$

i.e.,

$$\frac{d^2P_0}{d\lambda^2} + \frac{P_0}{\Delta\lambda^2} \approx 0$$

Taking into account the interactions where $2\pi\Delta x = \Delta\lambda$ (closed oscillator), we have the following equation

$$\frac{d^2P_0}{dx^2} + 4\pi^2 \times \frac{P_0}{\Delta\lambda^2} \approx 0$$

then:

, $\Delta\lambda = h/m\upsilon$

$$\frac{d^2P_0}{dx^2} + 4\pi^2 \frac{P_0}{h^2} m^2v^2 \approx 0 \text{ or}$$

$$\frac{d^2P_0}{dx^2} + \frac{8\pi^2m}{h^2} P_0E_{\mathrm{k}} = 0 \qquad (15)$$

where $E_{\mathrm{k}}=mv^2/2$ electron kinetic energy.

Schrödinger equation for stationary state in coordinate x is

$$\frac{d^2\psi}{dx^2} + \frac{8\pi^2m}{h^2}\psi E_{\mathrm{k}} = 0 \qquad (16)$$

Comparing the Eqns. (15) and (16) we can see that P_0-parameter correlates numerically with the value of ψ function i.e., $P_0 \approx \psi$ and in general it is proportional to it, $P_0 \propto \psi$. Taking into account wide practical application of *P*-parameter methodology, we can consider this criterion as the materialized analog of ψ-function.

Since P_0-parameters, like ψ-function possess wave properties, the principles of superposition should be executed for them, thus determining the linear character of equations of adding and changing *P*-parameters.

Wave properties of *P*-parameters and principles of their addition

Since *P*-parameter possesses wave properties (by analogy with ψ-function) the regularities of the interference of corresponding waves should be executed mainly with structural interactions.

Minimum interference, oscillation attenuation (in anti-phase), takes place if the difference in wave motion (Δ) equals the odd number of semi-waves:

$$\Delta = (2n+1)\frac{\lambda}{2} = \lambda\left(n + \frac{1}{2}\right),$$

where n = 0, 1, 2, 3, … (17)

As applied to *P*-parameters this rules means that minimum interaction occurs if *P*-parameters of interacting structures are also "in anti-phase" i.e, there is an interaction either between oppositely charged systems or heterogeneous atoms (for example, during the formation of valence-active radicals CH, CH_2, CH_3, NO_2 …, etc).

In this case the summation of *P*-parameters takes place by the principle of adding the reverse values of *P*-parameters as in Eqns. (3) and (4).

The difference in wave motion (Δ) for *P*-parameters can be evaluated via their relative value ($\gamma = P_2/P_1$) or via the relative difference in *P*-parameters (coefficient α), which with the minimum of interactions produce an odd number:

$$\gamma = \frac{P_2}{P_1} = \left(n + \frac{1}{2}\right) = \frac{3}{2}, \frac{5}{2} \ldots \qquad (18)$$

when n = 0 (main state), P_2/P_1 = ½

Let us mention that for stationary levels of one-dimensional harmonic oscillator the energy of these levels $\varepsilon = h\nu(n+½)$, therefore in quantum oscillator, in contrast to a classical one, the minimum possible energy value does not equal zero.

In this model the minimum interaction does not produce the zero energy, corresponding to the principle of adding the reverse values of *P*-parameters (Eqns. 3 and 4). Maximum interference, oscillation amplification (in the phase), takes place if the difference in wave motion equals the even number of semi-waves:

$\Delta = 2n\frac{\lambda}{2} = \lambda n$ or $\Delta=\lambda(n+1)$

As applied to *P*-parameters the maximum amplification of interactions in the phase corresponds to the interactions of similarly charged systems or systems homogeneous in their properties and functions (for example, between the fragments and blocks of complex organic structures, such as CH_2 and NNO_2 in octogen). Then

$$\gamma = \frac{P_2}{P_1} = (n+1) \qquad (19)$$

By the analogy, for "degenerated" systems (with similar values of functions) of two-dimensional harmonic oscillator the energy of stationary states: $\varepsilon = h\nu(n+1)$.

In this model, the maximum interaction corresponds to the principle of algebraic addition of *P*-parameters (Eqns. 6-8). When $n = 0$ (basic state) we have $P_2 = P_1$, or maximum interaction of structures takes place when their *P*-parameters equal. This postulate can be used as the main condition of isomorphic replacements.[8]

STRUCTURAL EXCHANGE SPATIAL-ENERGY INTERACTIONS

In the process of solution formation and other structural interactions the single electron density should be set in the points of atom-component contact. This process is accompanied by the redistribution of electron density between the valence areas of both particles and transition of the part of electrons from some external spheres into the neighbouring ones. Apparently, frame atom electrons do not take part in such exchange.

Obviously, when electron densities in free atom-components are similar, the transfer processes between boundary atoms of particles are minimal, this is favourable for the formation of a new structure. Thus the evaluation of the degree of structural interactions in many cases means the comparative assessment of the electron density of valence electrons in free atoms (on averaged orbitals) participating in the process.

The less is the difference $(P'_0/r'_i - P''_0/r''_i)$, the more favourable is the formation of a new structure or solid solution from the energy point.

In this regard, the maximum total solubility, evaluated via the coefficient of structural interaction, α, is determined by the condition of minimum value α, which represents the relative difference of effective energies of external orbitals of interacting subsystems:

$$\alpha = \frac{P'_0/r'_i - P''_0/r''_i}{(P'_0/r'_i + P''_0/r''_i)/2} 100\ \% \qquad (20)$$

$$\alpha = \frac{P'_S - P''_S}{P'_S + P''_S} 200\ \% \qquad (20a)$$

where P_S, the structural parameter, is found by Eqn. (20).

$$\frac{1}{P_S} = \frac{1}{N_1 P'_E} + \frac{1}{N_1 P''_E} + \cdots \qquad (20b)$$

here N_1 and N_2 are the number of homogeneous atoms in subsystems.

The nomogram of the dependence of structural interaction degree (ρ) on the coefficient α, unified for the wide range of structures was prepared based on all the data obtained. Figure 1 presents such a nomogram obtained using P_E-parameters calculated via the bond energy of electrons (w_i) for structural interactions of isomorphic type.

The mutual solubility of atom-components in many (over a thousand) simple and complex systems have been evaluated earlier using this technique. The calculation results are in compliance with theoretical and experimental data.[8]

Isomorphism as a phenomenon is used to be considered as applicable to crystalline structures. But similar processes can obviously take place between molecular compounds, where their role and importance are not less than those of purely coulomb interactions.

In complex organic structures during the interactions the main role can be played by separate "blocks" or fragments. Therefore, it is necessary to identify these fragments and evaluate their spatial-energy parameters. Based on the wave properties of *P*-parameter, the overall *P*-parameter of each fragment can be found by the principle of adding the reverse values of initial *P*-parameters of all atoms. The resultant *P*-parameter of the fragment block or all the structure is calculated by the rule of algebraic addition of *P*-parameters of the fragments constituting them.

The role of the fragments can be played by valence-active radicals, e.g. CH, CH_2, OH^-, NO, NO_2, SO_4^{2-}, etc. In complex structures the given carbon atom usually has two or three side bonds. During the calculations by the principle of adding the reverse values of *P*-parameters, the priority belongs to those bonds, for which the condition of minimum interference is better performed. Therefore the fragments of the bond C-H (for CH, CH_2, CH_3 …) are calculated first, then separately the fragments N-R, where *R* is the binding radical (for example – for the bond C-N).

Apparently spatial-energy exchange interactions (SEI) based on equalizing electron densities of valence orbitals of atom-components have in nature the same universal value as purely electrostatic coulomb interactions, but they supplement each other. Isomorphism, known from the time of E. Mitscherlich (1820) and D.I. Mendeleev (1856), is only a particular manifestation of this general natural phenomenon. The numerical side of the evaluation of isomorphic replacements of components both in complex and simple systems rationally fit in the frameworks of *P*-parameter methodology. More complicated is to evaluate the degree of structural SEI for molecular, including organic structures. The technique for calculating *P*-parameters of molecules, structures and their fragments has been successfully implemented.

But such structures and their fragments are frequently not completely isomorphic with respect to each other. Nevertheless there is SEI between them, the degree of which in this case can be evaluated only semi-quantitatively or qualitatively. By the degree of isomorphic similarity all the systems can be divided into the following three types.

(1) Systems mainly isomorphic to each other i.e., systems with approximately identical number of dissimilar atoms and nearly similar geometrical shapes of interacting orbitals.

(2) Systems with the limited isomorphic similarity i.e, systems which either (a) differ by the number of dissimilar atoms but have nearly similar geometrical shapes of interacting orbitals, or (b) have definite differences in geometrical shapes of orbitals but have identical number of interacting dissimilar atoms.

(3) Systems not having isomorphic similarity i.e., systems, which differ considerably both by the number of dissimilar atoms and geometric shapes of their orbitals.

Then taking into account the experimental data, all types of SEI can be approximately classified as follows.

Systems (1): (i) α < 0-6 %, ρ = 100 %. Complete isomorphism, there is complete isomorphic replacement of atom-components, (ii) 6 % < α < 25-30 %, ρ = 98 – (0-3) %. There is either a wide or limited isomorphism according to nomogram 1. (iii) α > 25-30 %, no SEI.

Systems (2): (i) α < 0-6 %, (a) there is the reconstruction of chemical bonds, can be accompanied by the formation of a new compound, (b) breakage of chemical bonds can be accompanied by separating a fragment from the initial structure, but without attachments or replacements. (ii) 6 % < α < 25-30 %, limited internal reconstruction of chemical bonds without the formation of a new compound or replacements is possible and (iii) α > 20-30 %, no SEI.

Systems (3): (i) α < 0-6 %, (*a*) limited change in the type of chemical bonds of the given fragment, internal regrouping of atoms without the breakage from the main part of the molecule and without replacements, (*b*) change in some dimensional characteristics of the bond is possible. (ii) 6 % < α < 25-30 %, very limited internal regrouping of atoms is possible and (iii) α > 25-30 %, no SEI.

Nomogram (Figure 1) is obtained for isomorphic interactions for systems of types (1) and (2).

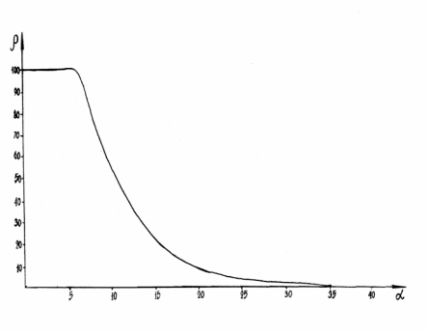

Figure 1. Dependence of the structural interaction degree (ρ) on the coefficient α

In all other cases the calculated values α and ρ refer only to the given interaction type, the nomogram of which can be clarified by reference points of etalon systems. If we take into account the universality of spatial-energy interactions in nature, this evaluation can be significant for the analysis of structural rearrangements in complex biophysical-chemical processes.

Fermentative systems contribute a lot to the correlation of structural interaction degree. In this system the ferment structure active parts (fragments, atoms, ions) have the value of P_E-parameter that is equal to P_E-parameter of the reaction final product. This means the ferment is structurally "tuned" via SEI to obtain the reaction final product, but it will not induced into it due to the imperfect isomorphism of its structure in accordance with (3).

The most important characteristics of atomic-structural interactions (mutual solubility of components, energy of chemical bond, energetics of free radicals, etc) were evaluated in many systems using this technique.[8-15]

TYPES OF FUNDAMENTAL INTERACTIONS

According to modern theories, the main types of interactions of elementary particles, their properties and specifics are mainly explained by the availability of special complex currents e.g., electromagnetic, proton, lepton, etc. Based on the foregoing model of spatial-energy parameter the exchange structural interactions finally come to flowing and equalizing the electron densities of corresponding atomic-molecular components. The similar process is obviously appropriate for elementary particles as well. It can be assumed that in general case interparticle exchange interactions come to the redistribution of their energy masses, *M*.

The elementary electrostatic charge associated with the electron as a carrier is the constant of electromagnetic interaction. Therefore for electromagnetic interaction we will calculate the system proton-electron.

For strong internucleon interaction that comes to the exchange of π-mesons, let us consider the systems nuclides-π-mesons. Since the interactions can take place with all three mesons (π^-, π^0 and π^+), we take the averaged mass in the calculations ($\langle M \rangle$ = 136,497 MeV s^{-1}).

Rated systems for strong interaction are

$$P - (\pi^-, \pi^0, \pi^+), (P\text{-}n) - (\pi^-, \pi^0, \pi^+)$$

and

$$(n\text{-}P\text{-}n) - (\pi^-, \pi^0, \pi).$$

Neutrino (electron, muonic) and its antiparticles were considered as the main representatives of weak interaction.

Dimensional characteristics of elementary particles (*r*) were evaluated in femtometer units (1 fm = 10^{-15} m) by the data presented earlier.[16]

At the same time, the classic radius, $r_e=e^2/m_e s^2$, was used for electron, where e is the elementary charge, m_e is the electron mass and s is the speed of light in vacuum. The fundamental Heisenberg length (6.690×10^{-4} fm) was used as the dimensional characteristic of weak interaction for neutrino.[16]

The gravitational interaction was evaluated via the proton P-parameter at the distance of gravitational radius (1.242×10^{-39} fm).

In the initial eqn. (3) for free atom, P_0-parameter is found by the principle of adding the reverse values q^2 and w_r, where q is the nucleus electric charge, w is the bond energy of the valence electron. Modifying the Eqn. (3), as applied to the interaction of free particles, we receive the addition of reverse values of parameters $P = Mr$ for each particle by Eqn. (21).

$$1/P_0=1/(Mr)_1 + 1/(Mr)_2+ \quad (21)$$

where M is the energy mass of the particle (MeV s^{-2}).

By using Eqn. (21) and the earlier data,[16] P_0-parameters of coupled strong and electromagnetic interactions were calculated in nuclides-π-mesons (P_n-parameters and proton-electron , P_e-parameter).

For weak and gravitational interactions only the parameters $P_\upsilon = Mr$ and $P_r = Mr$ were calculated, as in accordance with the Eqn. (21), the similar nuclide parameter with greater value does not influence the calculation results.

The relative intensity of interactions (Table 2) was found by the equations for the following interactions.

$$\text{Strong } \alpha_B =< P_n >/P_n >= P_n/P_n = 1 \quad (22a)$$

$$\text{Electromagnetic } \alpha_B = P_e/< P_n >= 1/136.983 \quad (22b)$$

$$\text{Weak } \alpha_B = P_e/< P_n >,$$

$$\alpha_B = 2.04 \times 10^{-10}, 4.2 \times 10^{-6} \quad (22c)$$

$$\text{Gravitational } \alpha_B = P_e/< P_n > = 5.9 \times 10^{-39} \quad (22d)$$

In the calculations for $\alpha_в$, the value of P_n-parameter was multiplied by the value equaled $2\pi/3$, i.e. $<P>=(2\pi/3)P_n$. Number 3 for nuclides consisting of three different quarks is "a magic" number (see the next section for details). As it is known, number 2π has a special value in quantum mechanics and physics of elementary particles. In particular, only the value of 2π correlates theoretical and experimental data when evaluating the sections of nuclide interaction with each other.[17]

As it has been reported,[18] nuclear interactions are distinguished as very strong, strong and moderately strong. For all particles in the large group with relatively similar mass values of mass, unitary multiplets or supermultiplets, very strong interactions are similar.[18] In the frames of the given model a very strong interaction between the particles corresponds to the maximum value of P-parameter, $P = Mr$ (coupled interaction of nuclides). Taking into consideration the equality of dimensional characteristics of proton and neutron, by eqn. (21), we obtain the values of P_n-parameter as 401.61; 401.88 and 402.16 (MeVfm s^{-2}) for coupled interactions *p-p*, *p-n* and *n-n*, respectively, thus obtaining the average value $\alpha_B = 4.25$. It is a very strong interaction. For eight interacting nuclides $\alpha_B \approx 1.06$ i.e., a strong interaction.

When the number of interacting nuclides increases, α_B decreases – moderately strong interaction. Since the nuclear forces act only between neighbouring nucleons, the value α_B cannot be very small.

The expression of the most intensive coupled interaction of nuclides is indirectly confirmed by the fact that the life period of double nuclear system appears to be much longer than the characteristic nuclear time.[19]

Thus it is established that the intensity of fundamental interactions is evaluated via P_n-parameter calculated by the principle of adding the reverse values in the system nuclides-π-mesons. Therefore, it has the direct connection with Plank's constants.

$$(2\pi/3)P_n \approx Er = 197.3 \text{ MeVfms}^{-2} \quad (23)$$

$$(2\pi/3)P_т \approx M_n\lambda_k = 197.3 \text{ MeVfms}^{-2} \quad (23a)$$

where

E and r, Plank's energy and Plank's radius are calculated via the gravitational constant,

M_n, λ_k, energy mass and nuclide Compton wave-length.

In Eqn. (21), the exchange interactions are evaluated via the initial P-parameters of particles equaled to the product of mass by the dimensional characteristic i.e., $P = Mr$.

Since these P-parameters can refer to the particles characterizing fundamental interactions, their direct correlation defines the process intensity degree (α_B):

$$\alpha_B = \frac{P_i}{P_n} = \frac{(Mr)_i}{(Mr)_n} \quad (24)$$

The calculations by the Eqn. (24), using the known Plank's values and techniques are given in table 3. As before, the energy and dimensional characteristics are taken from the literature.[16]

The results obtained are in accordance with theoretical and experimental data.[20,21]

ON QUARK SCREW MODEL

Let us proceed from the following theses and assumptions:

(i) By their structural composition macro- and micro world resemble. One part has some similarity with the other: solar system – atom – atom nucleus – quarks.

(ii) All parts of this "matroshka" are structural formations.

Table 2. Types of fundamental interactions

Interaction type		M, $\langle M \rangle$ MeVs^{-2}	r fm	Elementary particles	M, $\langle M \rangle$ MeVs^{-2}	r fm	P_n, P_e, P_ν, P_g *MeVfms*$^{-2}$	$2\pi/3P_n = \langle P_n \rangle$	α_B , $\langle \alpha_B \rangle$ (Eqn. 22)	α_B (experimental)
Electromagnetic	*P*	938.28	0.856	e^-	0.5110	2.8179	P_e=1.4374	-	1/136.983	1/137.04
Strong	*P*	938.28	0.856	π^-, π^0, π^+	136.497	0.78	P_n=94.0071	196.89	1	1
	P-n	938.92	0.856	π^-, π^0, π^+	136.497	0.78	P_n=94.015	196.90	1	1
	n-P-n	939.14	0.856	π^-, π^0, π^+	136.497	0.78	P_n=94.018	196.91	1	1
Weak				υ_e, $\overline{\upsilon_e}$	$<6 \times 10^{-5}$	6.69×10^{-4}	P_ν=4.014·10^{-8}		$<2.04 \times 10^{-10}$	10^{-10} - 10^{-14}
				υ_μ, $\overline{\upsilon_e}$	<1.2	6.69×10^{-4}	P_ν=8.028 ×10^{-4}		$<4.2 \times 10^{-6}$	10^{-5} - 10^{-6}
Gravitational	*P*	938.28	1.242×10^{-39}				P_c=1.17 × 10^{-36}		5.9×10^{-39}	10^{-38} - 10^{-39}

Table 3. Evaluation of the intensity of fundamental interactions using Plank's constants and parameter $P = Mr$.

Interaction type	Particles, constants	M MeVs^{-2}	r fm	Mr MeVs^{-2}	$\alpha_B = Mr/(Mr)_p$ (calculated)	α_B (experimental)
Strong	Proton	938.28	λ=0.2103	197.3	1	1
	Plank's values	1.221×10^{22}	1.616×10^{-20}	197.3		
Electromagnetic	electron	0.5110	2.8179	1.43995	1/137.02	1/137.036
Weak	$U_e\overline{\upsilon_e}$	$<6 \times 10^{-5}$	6.69×10^{-4}	$<4.014 \times 10^{-8}$	$<2.03 \times 10^{-10}$	10^{-10}- 10^{-14}
	$U_u\overline{\upsilon_e}$	<1.2	$6.69 \cdot 10^{-4}$	$<8.028 \cdot 10^{-4}$	$<4.07 \cdot 10^{-6}$	10^{-5} - 10^{-6}
Gravitational	Proton	938.28	1.242×10^{-39} Gravitational radius	1.165×10^{-36}	5.91×10^{-39}	10^{-38} - 10^{-39}

(iii) Main property of all systems is motion, translatory, rotary and oscillatory.

(iv) Description of these motions can be done in Euclid three-dimensional space with coordinates *x*, *y* and *z*.

(v) Exchange energy interactions of elementary particles are carried out by the redistribution of their energy mass *M* (MeVs^{-2}).

Based on these theses we suggest discussing the following screw model of the quark.

(i) Quark structure is represented in certain case as a spherical one, but in general quark is a flattened (or elongated) ellipsoid of revolution. The revolution takes place around the axis (*x*) coinciding with the direction of angular speed vector, perpendicular to the direction of ellipsoid deformation.

(ii) Quark electric charge (*q*) is not fractional but is an integer, but redistributed in three-dimensional space with its virtual concentration in the directions of three coordinate axes. Each axis having an electric charge = *q*/3.

(iii) Quark spherical or deformed structure has all three types of motion. Two of them, rotary and translator, are in accordance with the screw model, which beside these two motions, also performs an oscillatory motion in one of three mutually perpendicular planes, xoy, xoz, yoz (Figure 2).

(iv) Each of these oscillation planes corresponds to the symbol of quark color, e.g. red for *xoy*, blue for *xoz* and green for *yoz*.

(v) Screw can be "right" or "left". This directedness of screw rotation defines the sign of quark electric charge. Let us assume that the left screw corresponds to positive and right to negative quark electric charge.

(vi) Total number of quarks is determined by the following scheme: for each axis (*x*, *y* and *z*) of translator motion two screws (right and left) with three possible oscillation planes.

(vii) We have 3 × 2 × 3 = 18 quarks. Besides, there are 18 antiquarks with opposite characteristics of screw motions. In all there are thus 36 types of quarks.

These quark numbers can be considered as realized degrees of freedom of all three motions (3 translatory + 2 rotary + 3 oscillatory).

Translatory motion is preferable by its direction, coinciding with the direction of angular speed vector. Such elementary particles constitute our World. The reverse direction is less preferable, this is "Antiworld".

Motion along axis x in the direction of the angular speed vector, perpendicular to the direction of ellipsoid deformation, is apparently less energy consumable and corresponds to the quarks *U* and *d*, forming nuclides.

Such assumption is in accordance with the values of energy masses of quarks in the composition of andirons, 0.33. 0.33, 0.51, 1.8, 5 in $GeVs^{-2}$ for *d, u, s, c, b, t* types of quarks, respectively.

The quark screw model can be proved by other calculations and comparisons also.

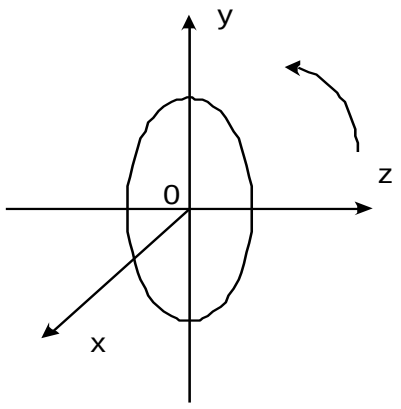

Figure 2. Structural scheme of quark in section *yoz*.

CALCULATION OF ENERGY MASS OF FREE NUCLIDE (TAKING NEUTRON AS AN EXAMPLE)

Neutron has 3 quarks d_1-*u*-d_2 with electric charges -1, +2, -1, distributed in three spatial directions, respectively. Quark *u* cements the system electrostatically. Translatory motions of the screws d_1-*u*-d_2 proceed along axis x, but oscillatory ones proceed in three different mutually perpendicular planes (Pauli principle is realized).

Apparently, in the first half of oscillation period *u*-quark oscillates in the phase with d_1-quark, but in the opposite phase with d_2-quark. In the second half of the period everything is vice versa. In general such interactions define the geometrical equality of directed spatial-energy vectors, thus providing the so-called quark discoloration.

The previously formulated rules of adding *P*-parameters spread to both types of *P*-parameters (P_0 and P_E). In this case, there is an additional energy P_E-parameters, since the subsystems of interactions possess similar dimensional characteristics. As both interactions are realized inside the overall system, P_E-parameters are added algebraically, and more accurately, in this case, geometrically by the following formula

$$\frac{M}{2} = \sqrt{m_1^2 + m_2^2}$$

where, *M* is the energy mass of free neutron, $m_1 = m_2 = 330$ $MeVs^{-2}$ masses of quarks *u* and *d* (in the composition of androns).

The calculation gives $M = 933.38$ $MeVs^{-2}$. This is for strong interactions. Taking into account the role of quarks in electromagnetic interactions,[21] we get the total energy mass of a free neutron as M=933.38+933.38/137=940.19 $MeVs^{-2}$. With the experimental value $M = 939.57$ $MeVs^{-2}$ the relative error in calculations is 0.06 %.

CALCULATION OF BOND ENERGY OF DEUTERON VIA THE MASSES OF FREE QUARKS

The particle deuteron is formed during the interaction of a free proton and neutron. The bond energy is usually calculated as the difference of mass of free nucleons and mass of a free deuteron. Let us demonstrate the dependence of deuteron bond energy on the masses of free quarks. The quark masses are added algebraically in the system already formed, in proton $m_1 = 5 + 5 + 7 = 17$ $MeVs^{-2}$, in neutron $m_2 = 7 + 7 + 5 = 19$ $MeVs^{-2}$. As a dimensional characteristic of deuteron bond we take the distance corresponding to the maximum value of nonrectangular potential pit of nucleon interaction. By the graphs experimentally obtained we know that such distance approximately equals 1.65 fm. Exchange energy interactions of proton and neutron heterogeneous systems are evaluated based on the Eqn. (21). Then we have:

$$1/ (M_C\, 1.65\, K) = 1/(17 \cdot 0.856) + 1/(19 \cdot 0.856),$$

where $K = 2\pi/3$. Based on the calculations we have $M_C = 2.228$ $MeVs^{-2}$, this practically coincides with reference data[20] ($M_C = 2.225$ $MeVs^{-2}$).

After modification, the basic theses of quark screw model can be applied to other elementary particles (proton, electron, neutron, etc) also. For instance, an electrically neutral particle neutron can be considered as a mini-atom, the analog of hydrogen atom.

CONCLUSIONS

(1) The notion of spatial-energy parameter (*P*-parameter) is introduced based on the simultaneous accounting of important atomic characteristics and modified Lagrangian equation.

(2) Wave properties of *P*-parameter are found, its wave equation formally similar to the equation of ψ-function is obtained.

(3) Applying the methodology of *P*-parameter

(a) most important characteristics of exchange energy interactions in different systems have been calculated

(b) intensities of fundamental interactions have been calculated and

(c) initial theses of quark screw model have been given.

REFERENCES

[1]Batsanov, S. S., Zvyagina, R. A., *Overlap integrals and challenge of effective charges*, Novosibirsk, Nauka, **1966**, 386.

[2]Fischer, C. F., *Atomic Data Nucl. Data Tables*, **1972**, *4*, 301-399.

[3]Waber, J. T., Cromer, D. T., *J. Chem. Phys*., **1965**, *42 (12)*, 4116-4123.

[4]Clementi, E., Raimondi, D. L., *J. Chem. Phys*., **1963**, *38 (11)*, 2686-2689.

[5]Clementi, E., Raimondi, D. L., *J. Chem. Phys*., **1967**, *47 (4)*, 1300-1307.

[6]Gombash, P., *Atom statistic theory and its application*, M., **1951**, 398.

[7]Clementi, E., *J. B. M. S. Res. Develop. Suppl*., **1965**, *9 (2)*, 76.

[8]Korablev, G. A., *Spatial Energy Principles of Complex Structures Formation*, Leiden, Brill Academic Publishers and VSP, Netherlands, **2005**, 426.

[9]Korablev, G. A., Kodolov, V. I., Lipanov, A. M., Chem. Phys. Mesoscopy. **2004**, *6*, 5-18.

[10]Korablev, G. A., Zaikov G. E., *J. Appl. Poly. Sci*., **2006**, *101*, 2101-2107.

[11]Korablev, G. A., Zaikov, G. E., *Reactions and Properties of Monomers Polymers*, Nova Science Publishers, Inc., New York, **2007**, 203-213.

[12]Korablev, G. A., Zaikov, G. E., *Success Gerontol.*, **2008**, *21 (4)*, 535-563.

[13]Korablev, G. A., Zaikov, G. E., *Mechanics of composition materials and constructions*, **2009**, *15 (1)*, 106-118.

[14]Korablev, G. A., Zaikov, G. E., *Chem. Phys., RAS*, M.: **2006**, *25 (7)*, 24-28.

[15]Korablev, G. A., Zaikov, G. E., *Monomers, Oligomers, Polymers, Composites and Nanocomposites Research*, Nova Science Publishers, USA, **2008**, 441-448.

[16]Murodyan, R. M., *PEChAYa, M., Atomizdat.*, **1977**, *8 (1)*, 175-192.

[17]Barashenkov, V. S., *Sections of interactions of elementary particles*, Nauka, Moscow, **1966**, 532.

[18]Yavorsky, B. M., Detlav, A. A., *Reference-book in physics*, Nauka, Moscow, **1968**, 940.

[19]Volkov, V. V., *PEChAYa, M., Atomizdat*., **1975**, *6*, 1040-1104.

[20]Bukhbinder, I. L., *Sorov Educ. J.*, **1997**, 5, http://nuclphys.sinp.msu.ru /mirrors/fi.htm.

[21]Okun, L. B., *Weak interactions*, http://www.book-site.ru/fulltext/1/001/008/ 103/ 116.htm.

Received: 09.10.2016.
Accepted: 04.12.2016.

OPTIMIZATION OF SUCROSE LOSS FROM SUGAR INDUSTRY

Jibril Goli[a] and Omprakash Sahu[b]*

Keywords: Boiling, crystallizer, economical, Massecuite, purity.

The aim of work is process optimization of a milling plant in order to minimize sucrose loss with final bagasse as another option. The experiment was carried out with design expert software. By identifying main factors i.e. imbibitions of water and hydraulic pressure effect on response variable i. e percentage sucrose in bagasse, it was applied to the process optimization in order to get the optimum process condition in which the sucrose loss is minimum. This is achieved at maximum imbibitions of water (62.6 $m^3 h^{-1}$) and maximum hydraulic pressure (110 kg cm^{-2}). Under these optimum conditions, the minimum sucrose in bagasse is 3.4 % unit. This results in sucrose saving of 0.04 ton h^{-1}.

* Corresponding Authors
Phone: +251933520653
E-Mail: ops0121@gmail.com
[a] Department of Chemical Engineering, KIOT, Wollo University, South Wollo, Ethiopia
[b] School of Chemical and Food Engineering, Bihar Dar Institute of Technology, Bahir Dar, Ethiopia

INTRODUCTION

Sugar industry is one of the major agro-industries and competitive sectors for the Ethiopian economy. The country has suitable weather conditions at different areas for cane plantation and sugar production.[1] There are three sugar factories with total production of about 3000,000 tons of plantation white sugar per year. Nowadays there are a number of projects in Ethiopia to expand the existing and to install new sugar factories (Metahara Sugar Factory Strategic Plan Manual, 2008). The goal of sugar cane factory is to have an efficient and profitable operation with the required sugar quality and maximum sugar recovery. One of the biggest problems in sugar industries is the loss of sucrose in different forms. The monetary value of the losses of sucrose is of extreme importance because of the direct impact on profitability. Generally, two types of sucrose losses exist in sugar factory, namely known/determined and unknown/undetermined losses.[2] The determined loss consists of losses of sucrose with by-products i.e. losses in bagasse, losses in filter cake losses in molasses. Undetermined sucrose losses include chemical (inversion), biological and mechanical losses (i.e. sucrose that is unaccounted for when completing a mass balance over the mill). All of these components need to be minimized to maximize sugar recovery. The sucrose loss in molasses is particularly important because it is normally by far the largest of the four components of total loss.[3]

For the sugar factory to be competitive and profitable, more attention must be paid to overall recovery of sugar. The cost of production of sugar is increasing from time to time due to escalating cost of spare parts and chemicals. The establishment of new sugar factories in Ethiopia and the globalization issues, including the COMESA agreement, may result in high competition among sugar factories. Therefore, the existing sugar factories need to improve their internal efficiency, particularly the recovery of sucrose, to become competitive, profitable and to assure sustainability.[4]

One of the biggest problems in the sugar industries which challenge their profitability is the loss of sucrose with bagasse, with filter cake and with final molasses. At present, in Metahara Sugar Factory (MSF) 9.1 to 9.3 % of the sugar that enters the factory with the cane are lost with final molasses. This is a big loss which should be minimized.[5] The company is losing sugar that is expected to be recovered and there is a need to increase the efficiency of sugar factory. The causes of the high sucrose loss with final molasses are not clearly identified for MSF. The aim of this project is therefore to identify the most significant loss areas and apply process optimization and equipment modification techniques to minimize the losses.

The main objective of this work is to investigate and study the process conditions at milling plant and D-massecuite processing line and finding the optimum point at low grade boiling, crystallization, reheating and centrifugal plant to reduce sucrose loss with final molasses.

EXPERIMENTALS

Cooling temperature, reheating temperature, brix, polarization (*pol*), and purity of final molasses, D massecuite and of liquor extracted from D massecuite at different steps were the study variables.

The study was conducted in two parts. First, assessment of the existing purity drop across each unit of D massecuite processing line (boiling, cooling, reheating and centrifugal separation) was conducted. This was done by intensive nutch filtration and analysis. After identifying the most significant loss areas, process optimization options were applied for each step.

MATERIALS

Samples of D–massecuite, final molasses and D-fore worker magma, seed for D-massecuite boiling were taken from different process steps. The study was conducted on-line using the existing D-vacuum pans, cooling crystallize, massecuite re-heater and D-centrifugal machines at MSF.

Optimization of D-massecuite boiling

Response surface methodology (RSM) was adopted in the design of experimental combinations.

The main advantage of RSM is the reduced number of experimental runs needed to provide sufficient information for statistically acceptable results.[6] A three-variable (three levels of each variable) Box Behnken experimental design was employed.[6] The parameters and their levels were chosen based on the practical experience and related literature available on molasses exhaustion. The independent variables included massecuite final brix (98-102), purity (54 – 58), and seed volume (1000-2000 mL) each at three levels. Higher the brix and seed volume the higher the purity drop, but the viscosity also increases. It was practically observed that discharging from pan is difficult with brix of more than 1020. With seed volume higher than 2000 mL, the grain size of the massecuite becomes very small which can pass through the centrifugal sieves and will cause high sucrose loss with molasses. It is also difficult to handle in crystallizers and pumps due high solidity of the massecuite. Hence seed volume of 2000 mL and massecuite brix of 102 are taken as maximum practical values.[7] Response variables were purity drop between the massecuite and its mother liquor, mother liquor purity and massecuite viscosity. By inserting minimum and maximum values into Design expert response surface Box Behnken program, the following combinations of the factors have been obtained.

Optimization of D-massecuite cooling

The effect of cooling temperature (43 – 49 ^{0}C) and time (18 – 36 h) on purity drop is studied. Cooling of final massecuite is usually done in the temperature range of 40-50 ^{0}C depending on the nature of the massecuite. Based on this fact, cooling experiment was aimed to be done in continuous crystallizers at massecuite temperatures of 40 – 50 ^{0}C by controlling the cooling water flow rate. But it was found that nutsch filtration was difficult with the existing compressed air pressure (6.0 bars) for massecuite temperature less than 43 ^{0}C. Therefore, a minimum temperature of 43 ^{0}C was kept for the experiment. Maximum and minimum limit of cooling time is taken from Mauritius experience. The experimental design was using design expert response surface.

Optimization on reheater

Two factors, cooling temperature of massecuite (43 – 49 ^{0}C) and reheating temperature (50 – 56 ^{0}C) each at three levels and three responses (purity rise across the re-heater, nutsch purity after reheater and massecuite flow rate) were considered. Reheating time is calculated from flow rate and reheater volume. Design Expert-Response surface- 'User Defined' is applied to analyze the data and to find optimum solution.

Optimization on centrifugal separation

The amount of water has been optimized based on the final molasses purity and D-fore worker sugar purity. Amount of spray water in flow % Massecuite (1 – 10 %) is a factor, and the responses are purity rise across DFW centrifugal machine and DFW magma purity. Design Expert-Response surface- One Factor Design is employed to analyze the data. With given minimum and maximum values of the factor.

Sample preparation and analysis

All analyses have been conducted according to International Commission for Uniform Methods of Sugar Analyses (ICUMSA) method for pol, brix and viscosity. Relative Viscosity of massecuite at discharge from pan has been done using the new HAAKE 6Plus viscometer. Purity is obtained from calculation of pol and brix. Infrared temperature sensor and thermometer were used temperature measurements. Horne's Dry Lead acetate, watch glass, and Whattmann No. 91 filter paper were used to clarify the samples for analysis of polarization. Weighing balance, Brix hydrometer, 200 mm polarization tubes, saccharometer, were used for measurement of the samples. Nutch bomb was used for pressure filtration (5.5-6 bar) of mother liquor from D-massecuite at different steps to study the purity drop. HAAKE 6Plus viscometer was used to measure viscosity of massecuite.

RESULTS AND DISCUSSION

Purity drop for the existing conditions

Sampling and purity analyses for massecuite and its respective mother liquor at pan discharge, inlet and outlet of each continuous crystallizers, reheaters and centrifugal machine were done. About 15 experiments were executed for each point to get reliable average values. The average values are given in Tables 1-3.

Table 1. Average purity drop across 1st battery of crystallizers.

S.No.	Unit	Temp. °C	Nutch Purity	Pty drop
1	*Discharge from pan (average massecuite purity= 57.35, brix = 101.3)	65.3	36.0	21.35
2	12 outlet/13 inlet	54.7	33.72	2.28
3	13 outlet /14 inlet	51.2	32.18	1.54
4	14 outlet /reheater inlet	48.8	31.66	0.52
5	Reheater outlet	53.6	32.52	-0.86
6	Centrifugal machine outlet (final molasses)	52.5	34.09	-1.57

Table 2. Average purity drop across 2nd battery of crystallizers

S.No.	Unit	Temp. °C	Nutch Purity	Pty drop
1	Pan	65.3	36.10	21.25
2	15 outlet/16 inlet	58.50	33.13	2.97
3	16 outlet /17 inlet	52.10	32.48	0.65
4	17outlet /reheater inlet	50.60	32.02	0.46
5	Reheater outlet	55.82	33.09	-1.07
6	Centrifugal machine outlet	55.60	35.61	-2.52

Table 3. Average purity drop for both the batteries of crystallizers.

S.No.	Unit	Temp. °C	Nutch purity	Pty drop
1	Pan	65.3	36.05	21.30
2	1st crystallizer	56.6	34.425	2.625
3	2nd crystallizer	51.65	32.33	1.1
4	3rd crystallizer	49.7	31.84	0.49
5	Reheater	54.71	32.81	-0.97
6	Centrifugal machine	54.05	34.86	-2.05

From the assessment it is seen that the purity drop across crystallizers is lower, only about 4.21 against standard of 5 – 7 in modern vertical crystallizers. The purity rise across centrifugal machine is acceptable (less than 2). The purity rise across the reheater is also higher than the standard values of less than 0.5 units. Assessment of the existing operation shows that there was lose control of the operation parameters at all D-massecuite processing steps and resulted in high loss of sucrose with final molasses. The average brix and purity of D-massecuite after boiling were 101.3 and 57.35 respectively, and the purity of mother liquor extracted from this massecuite (nutch purity at pan discharge) was 36.05. The massecuite was boiled with slurry volume of 2000 mL. The nutch purity obtained was higher than the required and ultimately contributed to the increase in final molasses purity. Therefore, optimization of boiling parameters (massecuite purity, seed volume and massecuite brix) was necessary to minimize the nutch purity on boiling.

At massecuite cooling, the final cooled temperature of the massecuite was only 49 °C, which resulted in low purity drop across crystallizers (only 4.21 units against the standard of more than 6 units). Here, the assessment results indicated that there was room for improvement at massecuite cooling to minimize sucrose loss with final molasses by increasing purity drop across cooling crystallizers. This can be achieved by cooling the massecuite to lower possible temperatures. Based on this fact, process optimization was carried out on massecuite cooling to obtain optimum cooling temperature and time at which high purity drop is achieved.

Considering the assessment study of D-massecuite reheating, there was an average mother liquor purity rise of 0.97 across reheater at reheating temperature of 54.71 ^{0}C. The purity rise obtained was higher than the required standard of 0 – 0.50 units. The purity rise should be reduced by controlling and optimizing the necessary parameters (cooling and reheating temperatures).[8]

For D-massecuite centrifugal separation, the average purity rise across centrifugal machines was 2.05 units. Purity rise in the “D” centrifuges should not be higher than 3 and it is better if it is lower than 2. The purity rise obtained from the assessment study was acceptable value when compared with the standard limits recommended on literatures. But during this test, the DFW sugar purity was on the low side (82 – 83), which will cause high recirculation of non-sucrose back to the boiling house. Therefore, optimization was required to improve the DFW magma (sugar) purity to the standard value of 84 or more without incurring high purity rise the mother liquor across centrifugal machines. The final molasses purity during the assessment study was also 34.86 which show a high sucrose loss.

Optimization of D-massecuite boiling

Based on the factors combination, series of experiment was done and the values of the responses at each factor level combination were taken. Boiling of D- massecuite was done in one pan, the massecuite and its mother liquor was analyzed for purity. The corresponding viscosity was also measured.

Data were modelled by multiple regression analysis and the statistical significance of the terms was examined by analysis of variance for each response. The adequacy of regression model was checked by R^2, Adj R^2, Pred R^2, Adeq Precision and *F*-test.[9] The significance of F value was judged at 95 % confidence level. Quadratic model is suggested by the design program for this response to test for its adequacy and to describe its variation with independent variables. From ANOVA test the Model F-value of 15363.10 implies the model is significant. There is only a 0.01 % chance that a "Model F-Value" this large could occur due to noise.

The graph indicates (Figure 1a) that purity drop increases with increase in massecuite brix at constant massecuite purity and seed volume (optimum seed volume and optimum massecuite purity). Examination of the response surface plots indicates that, purity drop increases with increase in seed volume and massecuite brix. At higher brix, more sucrose in the solution will be absorbed to the crystals due to high supersaturation and this will increase purity drop between the massecuite and its mother liquor (nutsch). More seed volume implies that there is Response surface plot for purity drop at boiling (with constant massecuite brix) large number of sugar crystals available in the solution for the sucrose molecule to be absorbed to. This is why the purity drop increases with seed volume (Figure 1b). From this graph we interpreted that, at constant massecuite brix and seed volume, as massecuite purity increase the purity drop is increased.The Model F-value of 2099.52 implies the model is significant. There is only a 0.01 % chance that a "Model F-Value" this large could occur due to noise. Values of "Prob > *F*" less than 0.0500 indicate model terms are significant.In this case *A*, *B*, *C*, *AB*, *BC*, A^2, B^2, C^2 are significant model terms. Values greater than 0.1000 indicate the model terms are not significant. The "Lack of Fit *F*-value" of 2.07 implies the Lack of Fit is not significant relative to the pure error. There is a 24.68 % chance that a "Lack of Fit *F*-value" this large could occur due to noise. Non-significant lack of fit is shown in the good-fit model (Figure 1c).

Model equation for nutch purity at boiling

Equation in terms of coded factors:

$$\text{Nutch purity} = 36.47 + 0.21A - 0.49B - 0.39C - 0.040AB + 3.750\text{x}10^{-3}AC - 0.060BC + 0.52A^2 - 0.082B^2 + 0.044C^2 \quad (1)$$

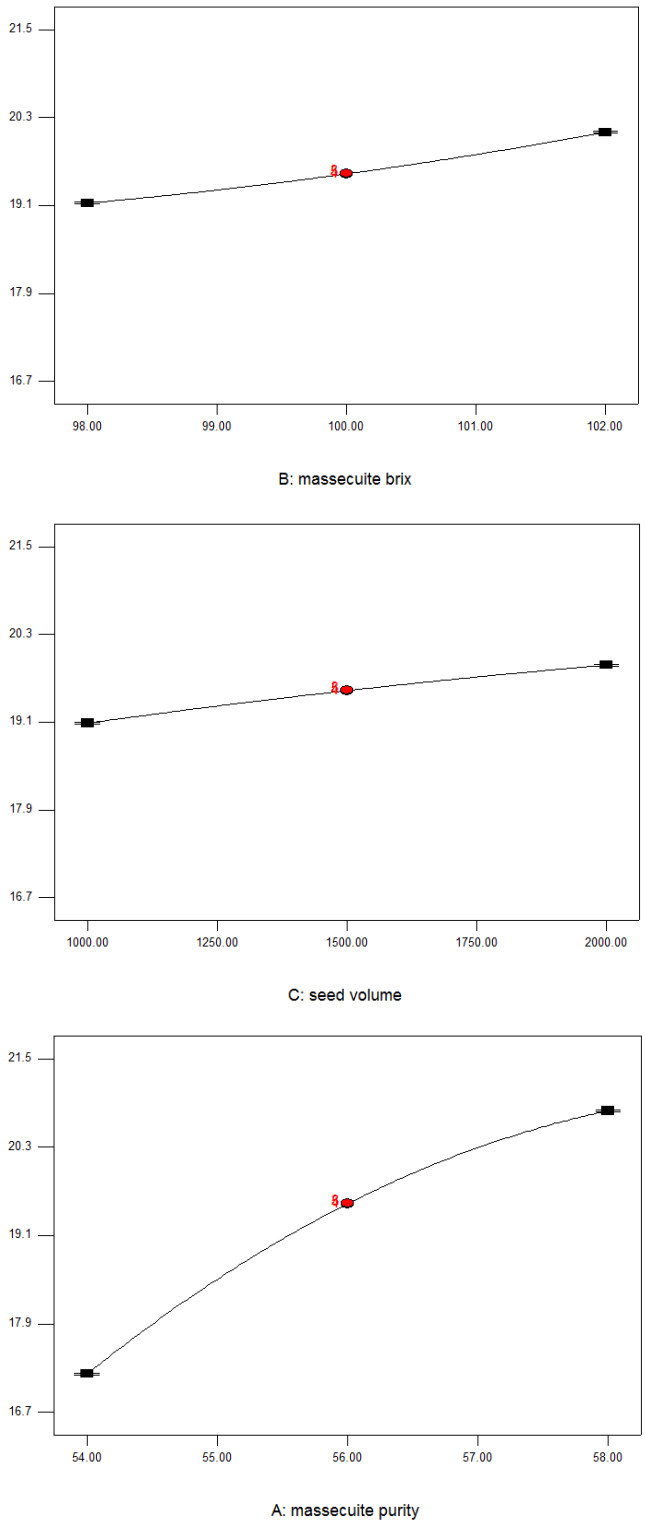

Figure 1. (a) Effect of massecuite brix on purity drop at constant seed volume and masseciute purity, (b) Effect of seed volume on purity drop, (c) Effect of massecuite purity on purity drop

Equation in terms of actual factors:

Nutch purity = 197.35225 – 13.57644*Pty* + 4.51375*Bx* +4.4717x10^{-3}*S*'– 0.01000*PtyBx*+3.75x10^{6}*PtyS*-6x10^{-5}*BxS* + 0.13103*Pty* ^{2}- 0.020531*Bx*^{2} + 1.76500x10^{-7}*S*^{2}

(2)

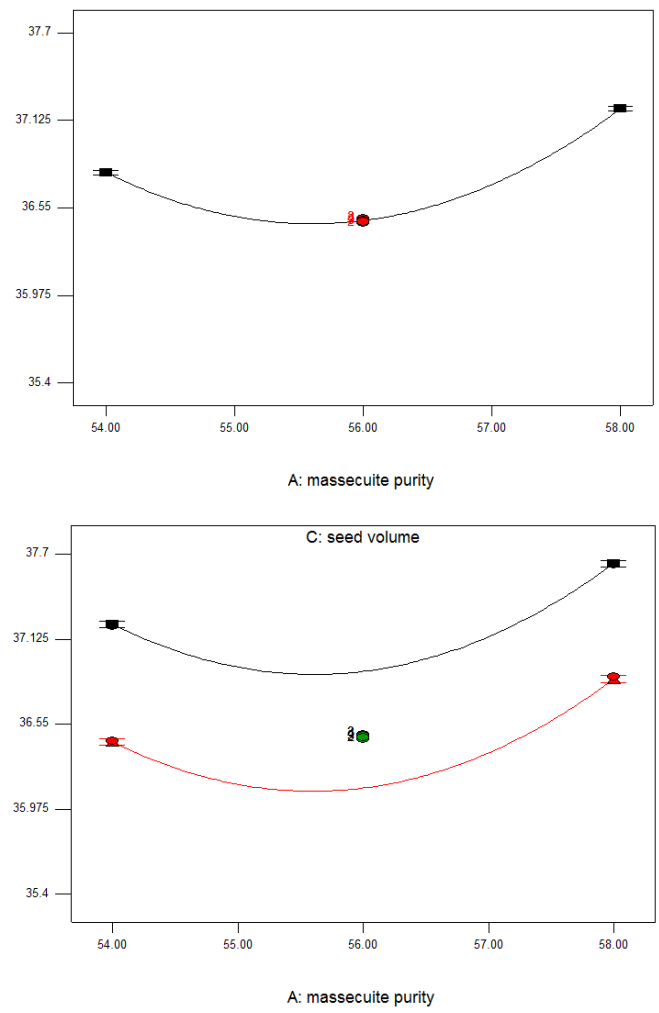

Figure2. (a) Effect of massecuite purity on nutch purity (b) Effect of seed volume and massecuite brix on nutch purity.

Analysis for nutch purity

The effects variation of factors on nutch purity is also observed, which showed in Figure 2a and b. At constant massecuite brix and seed volume, the nutch purity decreases with increases in massecuite purity for the massecuite purity of up to 56 and then increases with increase in massecuite purity. Minimum nutch purity is obtained at massecuite purity of about 56.

Analysis for massecuite viscosity

Linear model is suggested by the design program for this response. All statistical analysis including ANOVA test, post ANOVA statistics, lack of fit test are done for the Nutch purity data. All the tests indicated that the model is statistically acceptable.[10] All the Data analyses results indicate that the data are statistically valid, which presented in Table 4.

Model equation for viscosity optimization

Equation in terms of coded factors:

Relative viscosity = 201.39 -58.10*A*+31.58*B* + 35.43*C* (3)

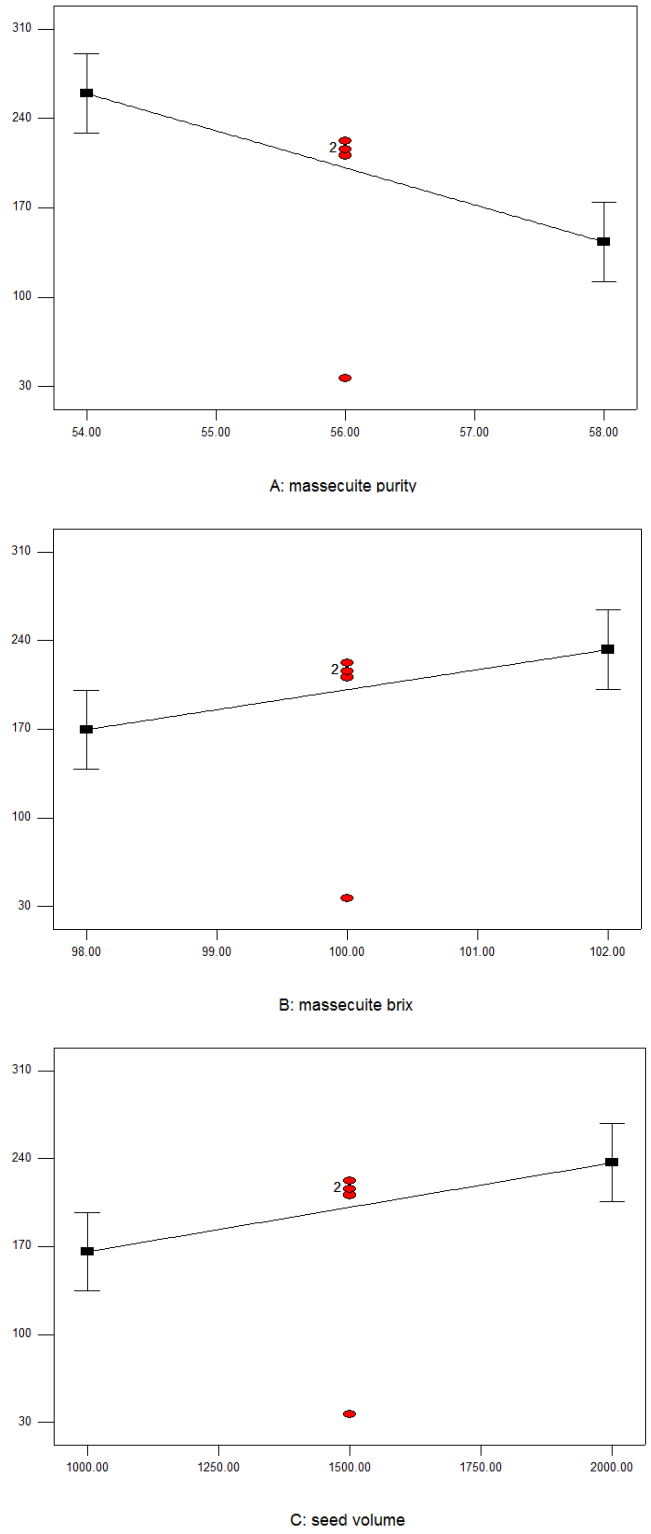

Figure3. (a) Effect of massecuite purity on viscosity, (b) Effect of seed volume on viscosity and (c) Effect of massecuite brix on viscosity

Equation in terms of actual factors:

$$\text{Relative viscosity} = 143.16676 - 29.05000Pty + 15.78750Bx + 0.070850S \quad (4)$$

The effects variation of factors on massecuite viscosity was also observed from the model equations and response surface plots shown in Figure 3. It is observed that the viscosity of the massecuite has a linear relationship with all the factors. It increases linearly with brix and seed volume and decreases with the purity of massecuite. The viscosity of D-massecuite increases almost linearly with increase in brix and decrease in purity. At low purity the proportion of non-sucrose impurities is high causing increase in the viscosity of the massecuite.

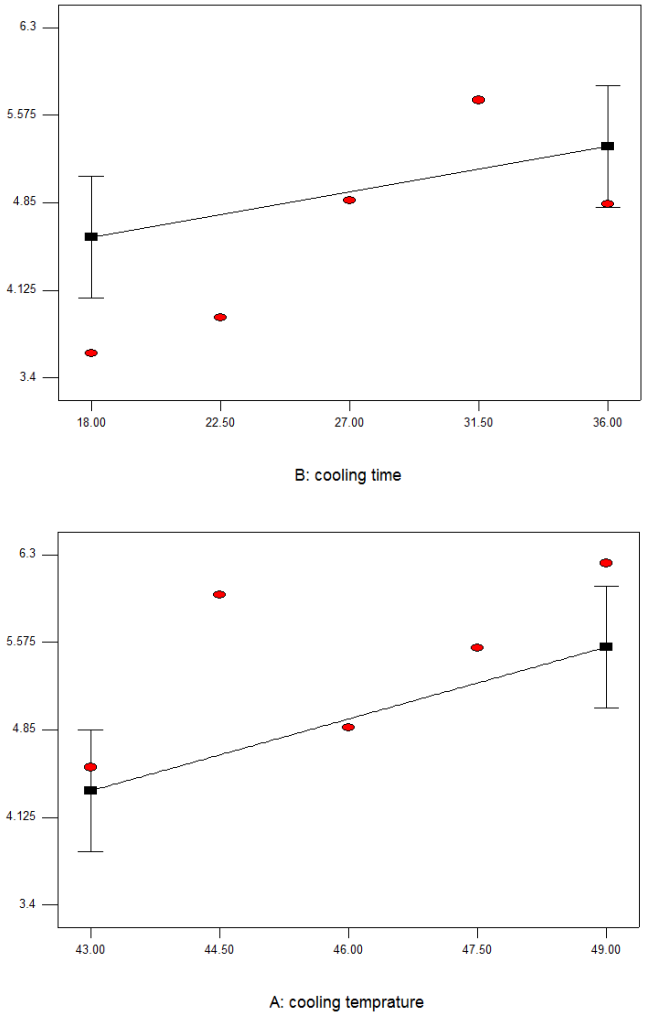

Figure 4. (a) The effect of cooling time on purity drop and (b) **E**ffect of cooling temperature on purity drop.

Optimization solution for D- massecuite boiling

The optimization was to get maximum purity drop, minimum nutch purity and minimum viscosity as much as possible. The Second response (nutch purity at boiling) was considered as an important response and more weight is given to it since it is the major determining factor of the final molasses purity. Six solutions are obtained. The solution with maximum desirability is selected as an optimum solution (with desirability of 58.8 %). Massecuite purity of 57.18^0, brix of 102^0 and seed volume of 2000 mL are selected as optimum parameters to obtain optimum purity drop of 21.41, nutch purity of 35.77 and massecuite relative viscosity of 244.332 Pa.s.

Table 4. Fit summary for massecuite viscosity.

S.No.	Source	*SD*	R^2	Adjusted R^2	Predicted R^2	Press	Remarks
1	Linear	47.68	0.6037	0.5123	0.5346	34707.30	Suggested
2	2FI	54.29	0.6048	0.3677	0.4830	38549.92	
3	Quadratic	61.25	0.6478	0.1950	0.3848	045878.45	
4	Cubic	80.51	0.6523	-0.3907		+	Aliased

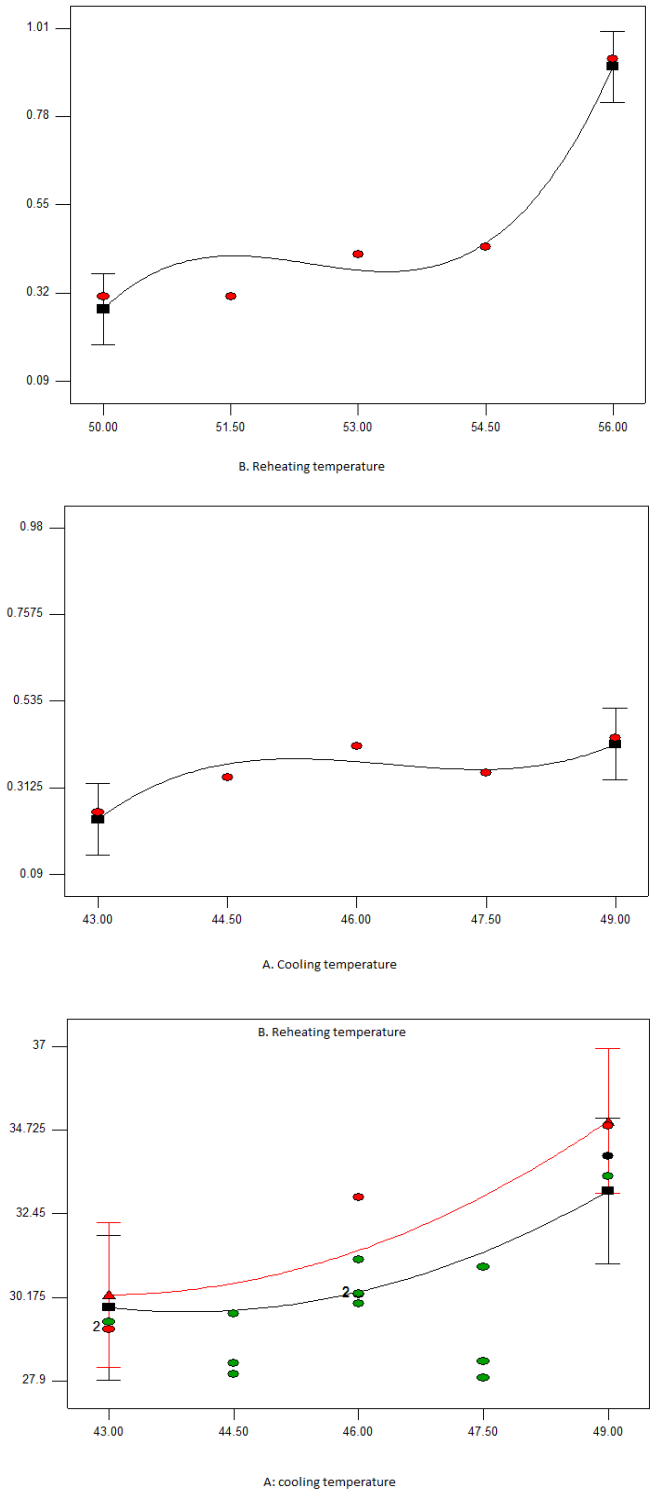

Figure 5. (a) Effect of reheater temperature on purity rise on reheater, (b) Effect of cooling temprature on purity rise across reheater (c) Response surface Plots Analysis for nutch purity after reheater.

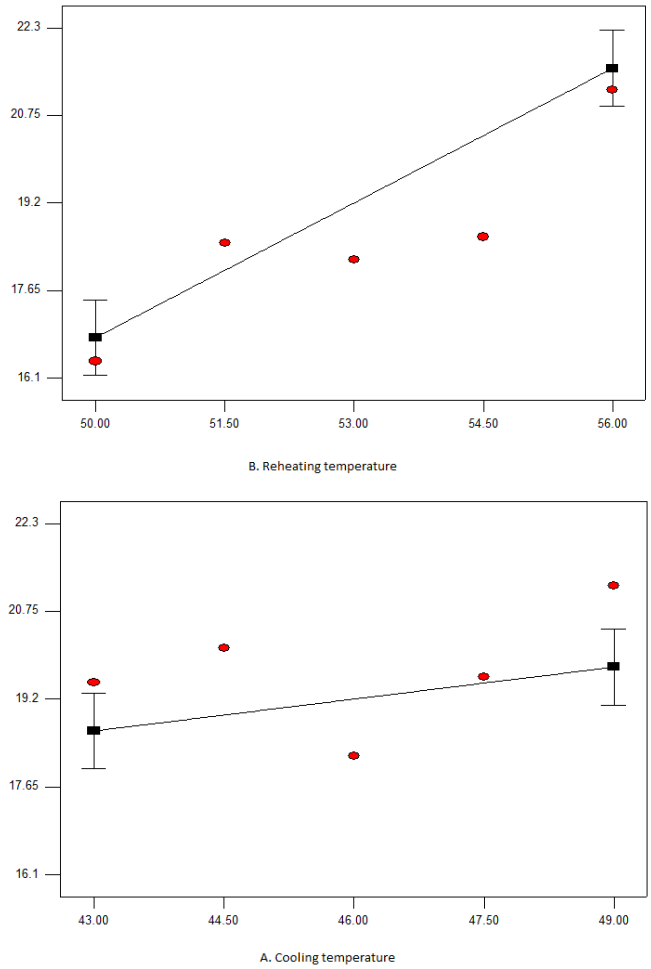

Figure 6. (a) Effect of water% massecuite on purity rise and (b) Effect of water percentage massecuite on DFW magma purity

D-Massecuite cooling optimization

Study of purity drop across continuous crystallizer was conducted by using nutsch analysis at different cooling temperature and time, in order to observe the trend of purity drop with temperature and cooling time, and to determine the optimum values. Cooling temperature is varied by changing the flow rate of cooling water to cooling discs and cooling time is varied by changing the massecuite flow rate to the crystallizer under study. Laboratory analyses were done for different factors level combinations as per the design.

Approach to this experiment

There are two batteries of crystallizers in Metahara sugar factory. One set of crystallizer (1st battery) was used for the study while the 2nd battery was working under accustomed condition. Before starting of the experiment, massecuite and cooling water flow were adjusted at different rates by manipulating the valves on the discharge lines in order to get the desired massecuite cooling temperature at desired cooling time. After several trials, the predetermined values were obtained at different valves openings. The valve opening positions and the water pressure on the cooling water discharge line were noted corresponding to the massecuite cooling temperature and cooling time. The cooling time was calculated from the known volume of the crystallizers and flow capacity of centrifugal machine in terms of current load.

Data analysis for massecuite cooling optimization

Data were modeled by multiple regression analysis and the statistical significance of the terms was examined by analysis of variance for each response. The statistical analysis of the data is performed using Design Expert Software (Stat-Ease). The adequacy of regression model was checked by R^2, Adj R^2, Pred R^2, Adeq Precision and *F*-test.[6] The significance of *F* value was judged at 95 % confidence level. The Model *F*-value of 3.26 implies there is a 6.88 % chance that a "Model *F*-Value" this large could occur due to noise. Values of "Prob > *F*" less than 0.0500 indicate model terms are significant. In this case *A* and *B* are significant model terms. Values greater than 0.1000 indicate the model terms are not significant. If there are many insignificant model terms (not counting those required to support hierarchy), model reduction may improve in model, which presented in Table 5.

Table 5. Post ANOVA test for purity drop D- masscuite cooling.

S.No.	Parameter	Value
1	SD	0.76
2	Mean	4.94
3	C.V. %	15.29
4	Press	11.24
5	R^2	0.3178
6	Adj R^2	0.2203
7	Pred R^2	0.0403
8	Adeq precision	6.124

The Pred R^2 of 0.0403 is in reasonable agreement with the Adj R^2 of 0.2203. Adeq Precision measures the signal to noise ratio. A ratio greater than 4 is desirable. Our ratio of 6.124 indicates an adequate signal. This model can be used to navigate the design space. *SD* stands for standard deviation.

Model equations for purity drop on massecuite cooling

Equation in terms of coded factor:

$$\text{Purity drop} = 4.94+0.6 \times A +0.38 \times B \quad (5)$$

Equation in terms of actual factor:

$$P_D = -5.32033 +0.19856 \times A + 0.0418 \times B \quad (6)$$

where,

A = cooling temperature
B = cooling time

Response surfacep analysis of purity drop on massecuite cooling

Purity drop on massecuite cooling is shown in Fig. 4a and b, the purity drop increases with decrease in cooling temperature and increase in cooling time. The lower the temperature, the lower the solubility of sucrose in the solution and hence less sucrose remain in solution, more sucrose from the solution deposited to the crystal surface.

Optimization solution for D-massecuite cooling

The optimization was to get maximum purity drop at minimum cooling time and maximum cooling temperature as much as possible. Best results are obtained at cooling temperature of 49 ^{0}C and cooling time of 18 h. At these optimum parameters, the purity drop is 5.16129 units with a desirability level of 84.5 %.

Analysis of optimization experiment on D-massecuite reheating. Response 1 - Purity Rise across reheater

Model equation for D-massecuite reheating optimization

Equation in terms of coded factors:

$$P_R = +0.38 - 0.051A - 0.062B + 0.21AB -0.051A^2 + 0.21B^2 - 0.097A^2B - 0.095AB^2 + 0.15A^3 + 0.35B^2 \quad (7)$$

Equation in terms of actual factors:

$$P_R = -1645.41788 + 6.65489 \times T_C + 89.57652 \times T_R - 0.57058 \times T_C^2 - 2.03920 \times T_R^2 - 3.57835 \times 10^{-3} \times T_C^2 \times T_R - 3.50997 \times 10^{-3} \times T_C \times T_R^2 + 5.46755 \times 10^{-3} \times T_C^3 + 0.013991 \times T_R^3 \quad (8)$$

where

P_R = Purity rise on reheater,
A= Coded value of cooling temperature,
B= Coded value of reheating temperature,
T_R= reheating temperature (°C),
T_C= Cooling temperature (°C),
N_P = Nutch purity after reheater.

Response 2 - Surface Plots Analysis for Purity Rise on Reheating

Effect of reheating temperature on purity rise across reheater : Purity rise across the reheater increases with increase in cooling as well as reheating temperatures.

The higher the gap between the cooling and reheating temperature, the higher is the purity rise.[11] This is due to the relatively longer time taken to bring the reheated temperature to the required value.

Model equation for nutch purity after reheater

Equ*ation in terms of coded factors*

$$N_P = 29.31 + 1.97A + 0.56B + 0.39AB + 1.16A^2 + 1.59B^2 \quad (9)$$

Equation in terms of actual factors

$$N_P = 861.65039 - 13.46743T_C - 20.47896R_T + 0.043268TC_{TR} + 0.1266T_C^2 + 0.17619T_R^2 \quad (10)$$

Response surface plots analysis for nutch purity after reheater

Nutch purity after reheating also increases with increase in both reheating and cooling temperature. Increase in temperature leads to dissolution of crystals in the massecuite and hence the purity of mother liquor. The result is representing in Fig. 5a, b and c.

Response - Massecuite Flow Rate (MFR) across reheater
Model equation development across reheater

Equation in terms of coded factor:

$$MFR = +19.20 + 0.56A + 2.38B \quad (11)$$

Equation in terms of actual factor:

$$MFR = -31.53825 + 0.18800T_C + 0.79422T_R \quad (12)$$

Response surface plots analysis for massecuite flow rate

The effect of cooling reheating temperature on massecuite flow rate is shown in Figure 6a and b. The massecuite flow rate increases with increase in temperature due to low viscosity at high temperatures. The figures reveal this fact and show that the effect of reheating temperature is more significant on the massecuite flow rate than cooling temperature. Flow rate sharply increases with increase in reheating temperature up to about 56 ˚C.

Optimization solution for Massecuite Reheating Experiment with maximum desirability is selected. One solution is obtained at desirability of 81.2 %. Minimum purity rise of 0.5346 units is obtained at optimum cooling temperature of 43 °C and reheating temperature of 50 °C.

D-massecuite centrifugal separation optimization

The amount of water was measured by online flow meter on the hot water line and the massecuite flow rate was calculated from the centrifugal machine load current. The load current has a direct relation with flow rate. The following data are generated for optimization across centrifugal machines.

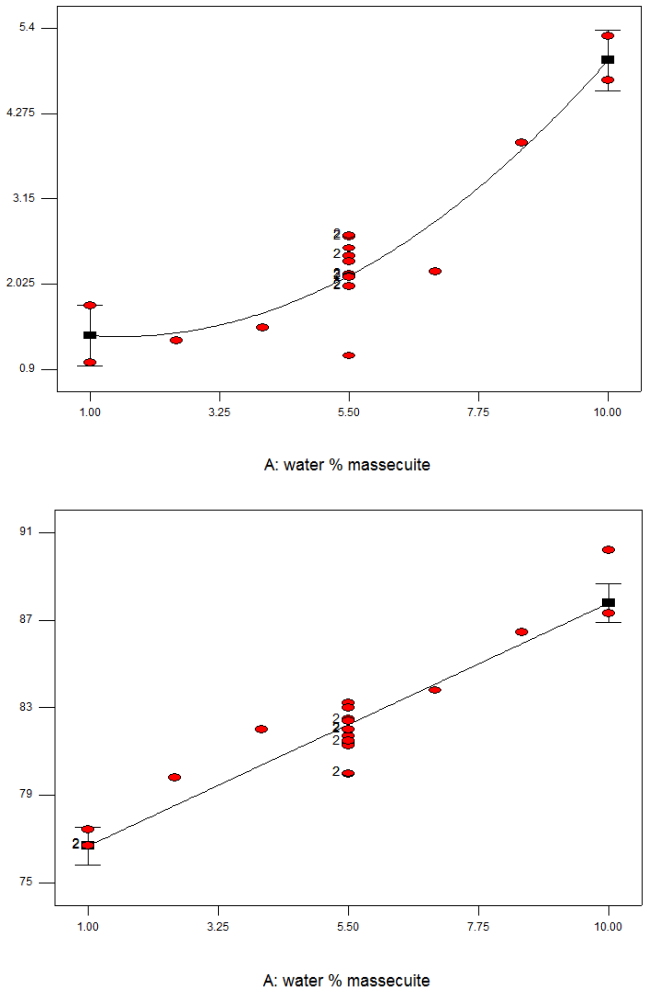

Figure 7. (a) Effect of water percentage massecuite on purity rise and (b)Effect of water percentage massecuite on DFW magma purity

(a) Analysis for optimization experiment on massecuite separation

The Model *F*-value of 57.74 implies the model is significant.There is only a 0.01 % chance that a Model *F*-Value this large could occur due to noise. Values of *Prob* > *F* less than 0.0500 indicate model terms are significant. In this case *A*, A^2 are significant model terms. Values greater than 0.1000 indicate the model terms are not significant. If there are many insignificant model terms (not counting those required to support hierarchy), model reduction may improve the model. The lack of fit *F*-value of 0.74 implies the lack of fit is not significant relative to the pure error. There is a 57.93 % chance that a lack of fit *F*-value this large could occur due to noise. Non-significant lack of fit is good, we want the model to fit.

Model equation for purity rise

Equation in terms of Coded Factors:

$$\text{Purity rise} = 2.14 + 1.82A + 1.03A^2 \quad (13)$$

Equation in terms of Actual Factors*:*

$$\text{Purity rise} = 1.44993 - 0.15377W + 0.050654W^2 \quad (14)$$

Response surface plots analysis for purity rise across centrifugal separation

Effect of water% massecuite on purity rise

There is a second order relationship between purity drop across centrifugal machine and the amount of spray water added, which is shown in Figure 7 (a).

DFW Magma Purity across centrifugal

The Model F-value of 111.43 implies the model is significant. There is only a 0.01 % chance that a Model F-Value, this large could occur due to noise. Values of *Prob > F* less than 0.0500 indicate model terms are significant. In this case A are significant model terms. Values greater than 0.1000 indicate the model terms are not significant. If there are many insignificant model terms (not counting those required to support hierarchy), model reduction may improve the model. The Lack of Fit F-value of 1.57 implies the Lack of Fit is not significant relative to the pure error. There is a 23.73 % chance that a Lack of Fit *F*-value this large could occur due to noise. Non-significant lack of fit is good, we want the model to fit.

Model equation for DFW magma purity

Equation in terms of Coded Factors:

$$DFW\ pty = 82.23 + 5.55\ A \quad (17)$$

Equation in terms of Actual Factors:

$$DFW\ pty = +75.44733+1.2394W \quad (18)$$

Response surface plots analysis for DFW magma purity

The effect of water percentage massecuite on DFW magma purity is shown in Figure 7b. For optimization solutions, one solution with maximum desirability is selected by the software. The solution was obtained with desirability of 59.8 %. The optimum spray water is 7.65 % massecuite. At this spray water, the optimum purity rise and DFW magma purity are 3.23 and 84.889 units respectively.

The higher the purity rise, the higher is the loss of sucrose with final molasses. The lower the purity of DFW magma purity, the higher is recirculation of molasses (non-sucrose) back to the boiling house. Non-sucrose recirculation also needs equal attention since it reduces boiling house efficiency, increase steam consumption and reduce final product quality.

Conclusion

To sum, according to economical point of view that the process optimizations were compared with the factory's existing working norms. D- Massecuite boiling optimization has resulted in nutsch purity reduction of 0.28 units. Similarly, an increase in purity drop of 0.95 (from 4.21 to 5.16) across cooling crystallizers was obtained at optimum cooling time of 18 h and temperature to 49 °C for the existing crystallizer's capacity. The cooling experimental results have indicated that a purity drop of 5.25 units can be achieved if crystallizer capacity of MSF increased so as to give cooling time of 20.3 h and temperature of 49 °C. For the existing reheaters, the optimum reheating temperature was found to be 50 °C which gave a purity rise across reheaters of 0.530 against the value of 0.97 before optimization and the optimum massecuite flow rate of 16.25 t h^{-1}. From the centrifugal separation optimization result, the optimum spray water was found to be 7.65 %, with which massecuite giving a purity rise of 3.238 across centrifugal machines and DFW magma purity of 84.88. The overall effect of process optimization was a reduction in final molasses purity by 0.48 units (from 34.86 to 34.38) for the existing capacity of cooling crystallizer which leads to annual saving of 1428.84 tons sugar, equivalent to 18,574,920 Birr. Additional saving of 4,058,964 Birr per year is expected if enough crystallizer capacity is installed for MSF.

References

[1]Humbert, R.P., *The growing of sugar cane*. Elsevier, **2013**

[2]Heriot, T. H., *Manufacture of sugar from cane and beet. International Common United Methods of Standard Association (ICUMSA), A Methods Book*, Bartens the Sugar and Sweeteners Publishers, England, **2008**.

[3]Jiju, A., *Design of Experiments for Engineers and Scientists*, Elsevier **2014**.

[4]Kulkarni, D. P., *Cane Sugar Manufacturing* in India, The Sugar Technologists' Association of India, **2009**.

[5]Miller, K. F., and D. M. Hogarth. *Sucrose losses in low grade massecuite processing*. in International Society of Sugar Cane Technologists. Proceedings of the XXIV Congress, Brisbane, Australia, 17-21 September 2001. Volume 1., pp. 366-367. Australian Society of Sugar Cane Technologists, **2001**.

[6]Myers, R.H. and Montgomery, D.C., *Response surface methodology*, Willey, New York, **2001**

[7]Mosen, A., *Beet Sugar Handbook*, John Wiley & Sons. **2006**.

[8]Mullin, J. W., *Crystallization*, Butterworth-Heinemann, **2001**.

[9]Naidoo, G., Schoonees, B. M., and Schom, P. M., *SASTA Laboratory Manual including the Official Methods*, July 2005. The South African Sugar Technologists' Association, South African.**2005**

[10]Ninela, M., Rajoo, H., *Proc. S. Afr. Sugar Technol. Ass*., **2006**, *80*, 448-461.

[11]Rein, P.W., Smith, I.A., *Proc. S. Afr. Sugar Technol. Ass*., **1981**, *73*, 85-91.

Received: 23.11.2016
Accepted: 24.12.2016.

SONOCHEMICAL SYNTHESIS AND CHARACTERIZATIONS OF NANOSIZED METAL COORDINATION POLYMERS DERIVED FROM 5-(3-PYRIDYL)-1,3,4-OXADIAZOLE-2-THIOLE AND 2-AMINOTHIAZOLE

Maged S. Al-Fakeh[a, b]

Keywords: Coordination polymers,Nanoparticles, SEM, XRD, thermal studies.

Nanosized coordination polymers of Co(II), Ni(II), Cu(II) and Cd(II) of mixed ligand derived from 5-(3-pyridyl)-1,3,4-oxadiazole-2-thiole (POZT) and 2-aminothiazole (AZ) were synthesized. The compounds were characterized by elemental analysis, IR and electronic spectral studies. Thermogravimetry (TG), derivative thermogravimetry (DTG) and differential thermal analysis (DTA) have been used to study the thermal decomposition steps of the compounds and to calculate the thermodynamic parameters of the nanosized metal coordination polymers. The kinetic parameters have been calculated making use of the Coats-Redfern and Horowitz-Metzger equations. The scanning electron microscope SEM photographs and particle size calculations from the powder XRD data indicate the nano-sized nature of four compounds prepared under ultrasonic irradiation (average size 23-56 nm). The antimicrobial activity of the synthesized compounds was tested against six fungal and five bacterial strains. The majority of compounds were effective against the tested microba.

* Corresponding Authors
E-Mail: alfakehmaged@yahoo.com

[a] Taiz University, Taiz, Republic of Yemen
[b] Department of Chemistry, College of Science, Qassim University, Kingdom of Saudi Arabia

Introduction

Metal-organic frameworks (MOFs) are extensively developed as a new type of functional crystalline materials for a wide range of promising applications in separation, storage, exchange, and heterogeneous catalysis due to their high stability and structural diversity.[1-3] Nanometer-sized particles of metal coordination polymers are of interest to explore, since their unique properties are controlled by the large number of surface molecules, leading to an entirely different environment than those in a bulk crystal.[4] Therefore, they are of potential use as materials for nanotechnological applications. The variety of pyridyl connectors have been extensively applied in this respect.[5] The important role played by organosulfur compounds, in chemical or biological processes are well documented.[6] The pyridyl-oxadiazoles are suitable bridging ligands for the synthesis of coordination polymers and several papers have been published on using cyclized pyridyl 1,3,4-oxadiazoles for the preparation of metal complexes.[7-9] Azoles represent a very interesting class of compounds because of their pharmaceutical, analytical and industrial applications.[10] We now report the preparation and characterization of nanosized Co(II), Ni(II), Cu(II) and Cd(II), 5-(3-pyridyl)-1,3,4-oxadiazole-2-thiole and 2-aminothiazole complexes.

Experimental

High purity 5-(3-pyridyl)-1,3,4-oxadiazole-2-thiole (POZT) and 2-aminothiazole (AZ) were supplied from Sigma Aldrich and Merck. All other chemicals were of AR grade.

Preparation of the coordination polymers

Preparation of the mixed ligand complexes of POZT and AZ with Co(II), Ni(II), Cu(II) and Cd(II) followed essentially the same procedure. The preparation of $[Co(POZT)(AZ)Cl(H_2O)_2]_n$ is given below as a typical example.

To an ethanolic solution (15 mL) of $CoCl_2.6H_2O$ (0.5 mmol), a hot solution (15 mL) of POZT (0.5 mmol) was added dropwise with stirring, and then a solution of AZ (10 mL ethanol, 0.5 mmol) was added to the mixture. The mixture was refluxed and then cooled to room temperature. Subsequently, the solution mixture was stirred for 40 min under ultrasonic irradiation and then the blue precipitate was separated, washed with distilled water and EtOH and dried over $CaCl_2$ in a desiccator.

Physical Measurements

Stoichiometric analyses (C, H, N, S) were performed using Analyischer Funktionstest Vario El Fab-Nr.11982027 elemental analyzer. IR spectra were recorded as KBr disks (400-4000 cm^{-1}) with a FT-IR spectrophotometer model Thermo-Nicolet-6700 FTIR and the electronic spectra were obtained using a Shimadzu UV-2101 PC spectrophotometer. Magnetic susceptibility measurements were done on a magnetic susceptibility balance of the type MSB-Auto. The conductance was measured using a conductivity Meter model 4310 JENWAY. Thermal studies were carried out in dynamic air on a Shimadzu DTG 60-H thermal analyzer at a heating rate 10 °C min^{-1}. XRD-diffraction patterns were recorded on a diffractometer Model PW 1710 control unit Philips, anode material Cu 40 K,V 30 M,aoptics: automatic divergence slit. Scanning electron microscope was of the type JEOL JFC-1100E ION SPUTTERING DEVICE, JEOL JSM-5400LV SEM. SEM specimens were coated with gold to increase the conductivity. For the biological activity, all microbial strains were kindly provided by the Assiut University Mycological Centre (AUMC), Egypt. These

strains are common contaminants of the environment and some of which are involved in human and animal diseases (*Candida albicans*, *Geotrichum candidum*, *Scopulariopsis brevicaulis*, *Aspergillus flavus*, *Staphylococcus aureus*), plant diseases (*Fusarium oxysporum*) or frequently reported from contaminated soil, water and food substances (*Escherichia coli*, *Bacillus cereus*, *Pseudomonas aeruginosa* and *Serratia marcescens*). To prepare inocula for bioassay, bacterial strains were individually cultured for 48 h in 100 mL conical flasks containing 30 mL nutrient broth medium. Fungi were grown for 7 days in 100 mL conicals containing 30 mL Sabouraud's dextrose broth. Bioassay was done in 10 cm sterile plastic Petri plates in which microbial suspension (1 mL/plate) and 15 mL appropriate agar medium (15 mL/plate) were poured. Nutrient agar and Sabouraud's dextrose agar were respectively used for bacteria and fungi. After solidification of the media, 5 mm diameter cavities were cut in the solidified agar (4 cavities/plate) using sterile cork borer. The chemical compounds dissolved in dimethylsulphoxide (DMSO) at 2%w/v (= 20 mg/mL) were pipetted in the cavities (20 ul /cavity). Cultures were then incubated at 28°C for 48 h in case of bacteria and up to 7 days in case of fungi. Results were read as the diameter (in mm) of inhibition zone around cavities.[11]

Result and discussion

The compounds were prepared by the reaction of 5-(3-pyridyl)-1,3,4-oxadiazole-2-thiole, metalchlorides and 2-aminothiazole (dissolved in EtOH). The prepared complexes were found to react in a molar ratio of 1:1:1 of metal, POZT and AZ.The complexes are air-stable, they are insoluble in common organic solvents but partially soluble in DMF and DMSO. The conductivity values, measured in DMSO at room temperature, lie within the range for nonelectrolytes. The compositions of the complexes are supported by the elemental analysis provided in table 1.

Fourier transform infrared spectroscopy (FT-IR)

The main FT-IR frequencies can be seen in table 2. The bands observed in the 1608-1620 cm^{-1} regions are assigned to the υ(C=N) stretching vibration of the 5-(3-pyridyl)-1,3,4-oxadiazole-2-thiole.[12] It is found that the CSC band of the 2-aminothiazole at ~740 cm^{-1} is almost unchanged in the respective complexes, indicating that the thiazole-S is not involved in the bonding.[13] The same is true for the νC=N stretching vibration of the azole for all complexes where no appreciable shift was noticed. However, the stretching vibration of the amino group in the free AZ observed at 3220 cm^{-1} is shifted to a lower wave number, appearing in the range 3150-3172 cm^{-1} in the complexes and suggesting coordination of the amino nitrogen to the metal(II) ions.[14] Furthermore, it is found that the bands at 3445 cm^{-1} in the spectra of compound (**2**) is assigned to νOH of water of crystallization[15] whereas the νOH stretching vibrations of the coordinated water molecules are located in the range 3197-3202 cm^{-1} for all compounds.[16] Metal-oxygen and metal-nitrogen bonding are manifested by the appearance of a band in the 513-543 cm^{-1} and 428-446 cm^{-1} regions, respectively.[17]

Electronic spectra

The UV-Vis spectra of the compounds were recorded in DMSO. The spectra displayed two absorption maxima located in the regions35,714-37,037 and 29,411-31,746 cm^{-1} which are attributed to π→π* and n→π* transitions within the POZT and AZ ligands [18,19]. The Co(II), Ni(II) and Cu(II) coordination polymers exhibit a band at 18,685, 19,801 and 17,518 cm^{-1} respectively corresponding to the d-d transitions. In the visible spectra, there were characteristic bands attributed to the d-d transitions in the complexes typical of octahedral structures. The structure of the coordination polymers can be postulated as follows (Figures 2 and 3).

Magnetic measurements

The magnetic moments of the compounds were measured and it has been found that the cobalt(II) compound (**1**) has a magnetic moment of 4.38 B.M typical for octahedral complexes,[20] whereas the magnetic moment values 2.13 and 1.88 B.M that were found for the Ni(II) and Cu(II) compounds respectively suggest their octahedral structures.[21,22]

Thermal analysis

The thermal decomposition of the compounds has been investigated in dynamic air from ambient temperature to 700 °C. The thermal decomposition data of the compounds are collected in table 3. As a representative example the thermal behaviour of the Co(II) complex (**1**) will be described. The thermogram of the complex shows three decomposition stages. The first stage corresponds to the release of the two water molecules (calc. 8.81 %, found 7.41 %). The DTG curve displays this step at 177 °C and an endothermic peak appears at 179 °C in the DTA trace. The second and third steps correspond to the decomposition products of the ligands. These two steps are manifested by two DTG peaks at 331 and 500 °C and are associated with two exothermic peaks at 333 and 503 °C in the DTA curve, respectively. The final product was identified on the basis of mass loss consideration as CoO (calc. 18.33 %, found 17.61 %) (Scheme 1).

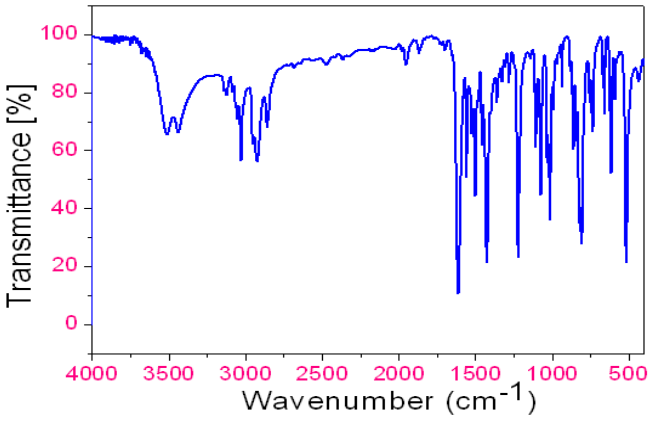

Figure 1. FT-IR spectrum of Ni(II) compound (**2**).

Table 1. Colors, elemental analysis and melting points of the compounds.

Compound	Mol. Wt	Color	Found (Calcd. %)				m.p.°C (decom.)
			C	H	N	S	
$\{[Co(POZT)(AZ)Cl(H_2O)_2]\}_n$ (**1**)	$C_{10}H_{12}CoN_5O_3S_2Cl$, 408.72	Blue	29.10 29.38	2.86 2.95	17.04 17.13	15.49 15.68	274
$\{[Ni(POZT)(AZ)Cl(H_2O)_2].H_2O\}_n$(**2**)	$C_{10}H_{14}NiN_5O_4S_2Cl$, 426.48	Light green	28.02 28.16	3.12 3.30	16.33 16.42	14.95 15.03	281
$\{[Cu(POZT)(AZ)Cl(H_2O)_2]\}_n$ (**3**)	$C_{10}H_{12}CuN_5O_3S_2Cl$, 413.34	Brown	28.97 29.05	2.86 2.90	16.90 16.94	15.48 15.51	269
$\{[Cd(POZT)(AZ)Cl(H_2O)_2]\}_n$ (**4**)	$C_{10}H_{12}CdN_5O_3S_2Cl$, 462.20	White	25.66 25.98	2.50 2.59	15.09 15.15	13.79 13.87	290

Table 2. Infrared spectral data of the coordination polymers.

No.	υ(OH)	υ(NH_2)	υ(C=N)	υ(C-N)	υ(C-S)	υ(M-O)	υ(M-N)
(**1**)	3198	3164	1616	1487	736	543	428
(**2**)	3445, 3200	3150	1620	1456	733	538	437
(**3**)	3197	3158	1608	1470	728	513	446
(**4**)	3202	3172	1615	1483	724	530	431

Table 3. Thermal decomposition data of the compounds.

	Step	TG/DTG			Mass loss (%)
		T_i	T_m	T_f	
(**1**)	1st	33	177	220	7.41
	2nd	221	331	386	23.88
	3rd	387	500	700	51.10
(**2**)	1st	29	60	130	11.77
	2nd	131	213	285	22.15
	3rd	286	394	436	8.08
	4th	437	502	700	41.94
(**4**)	1st	35	109	250	6.98
	2nd	251	321	435	28.75
	3rd	436	583	700	38.13

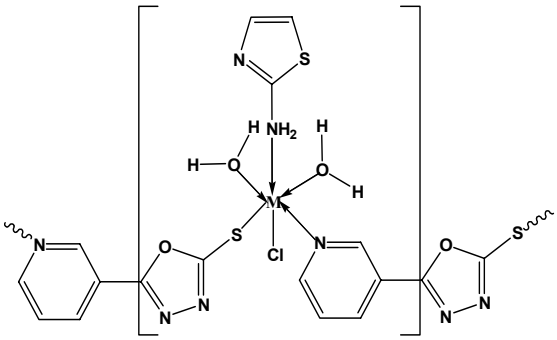

Figure 2. Proposed structure of the metal complex.

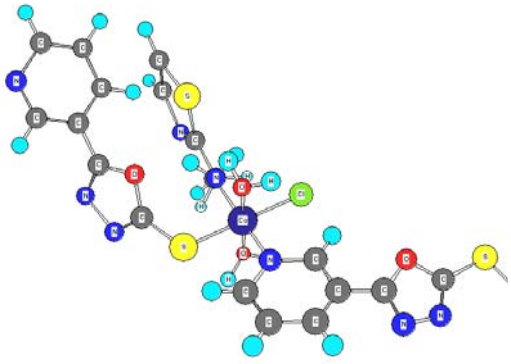

Figure 3. A perspective view of coordination round Co(II).

$[Co(POZT)(AZ)Cl(H_2O)_2]$

1st ↓ 33-220 °C

$[Co(POZT)(AZ)Cl] + 2\ H_2O$

2nd and 3rd ↓ 221-700 °C

Decomposed Product + CoO
(in dynamic air)

Scheme 1. Thermal decomposition of Co-compound

Table 4. Kinetic and thermodynamic parameters for the thermal decomposition of the compounds

Compound	Step	Coats-Redfern equation				ΔS^* J mol^{-1} K^{-1}	ΔH^* kJ mol^{-1}	ΔG^* kJ mol^{-1}
		r	*n*	*E*	10^{-2} *Z*			
(**1**)	1st	1.0000	0.50	55.6	6.52	-192.5	50.53	167.78
(**2**)	1st	0.9997	2.00	126.2	2.54	-186.4	120. 7	244.61
(**4**)	1st	1.0000	0.66	44.6	8.95	-194.1	39.65	155.18

Kinetic analysis

Non-isothermal kinetic analysis of the complexes was carried out applying two different procedures: the Coats-Redfern[23] and the Horowitz-Metzger[24] methods.

Coats-Redfern equation

$$\ln[1-(1-\alpha)^{1-n}/(1-n)T^2] = M/T + B \quad (\text{for } n \neq 1) \qquad (1)$$

$$\ln[-\ln(1-\alpha)/T^2] = M/T + B \qquad (\text{for } n = 1) \qquad (2)$$

where

α is the fraction of material decomposed,

n is the order of the decomposition reaction and

$M=E/R$ and

$B=ZR/\Phi E$;

E, *R*, *Z* and Φ are the activation energy, gas constant, pre-exponential factor and heating rate, respectively.

Horowitz-Metzger equation for $n \neq 1$

$$\ln[1-(1-\alpha)^{1-n}/1-n] = \ln ZRT_s^2/\Phi E - E/RT_s + E\theta/RT_s^2 \qquad (3)$$

for $n = 1$

$$\ln[-\ln(1-\alpha)] = E\theta/RT_s^2 \qquad (4)$$

where $\theta = T-T_s$, T_s is the temperature at the DTG peak.

The correlation coefficient, *r*, is computed using the least squares method for equations (1), (2), (3) and (4). Linear curves were drawn for different values of *n* ranging from 0 to 2. The value of *n*, which gave the best fit, was chosen as the order parameter for the decomposition stage of interest. The kinetic parameters were calculated from the plots of the left hand side of equations (1), (2), against $1/T$ and against θ for equations (3) and (4). The kinetic parameters were calculated according to the above two methods and are cited in Table 4.

The negative ΔS^* values for the different stages of decomposition of the complexes suggest that the activated complex is more ordered than the reactants and that the reactions are slower than normal.[25-27] The more ordered nature may be due to the polarization of bonds in the activated state, which might happen through charge transfer electronic transition.[28] The different values of ΔH^* and ΔG^* of the compounds refer to the effect of the structure of the metal ions on the thermal stability of the complexes.[29] The positive values of ΔG^* indicate that the decomposition reaction is not spontaneous.

X-ray powder diffraction of the compounds

The X-ray powder diffraction patterns were recorded for four of the coordination polymers. The diffraction patterns indicate that the compounds are crystalline. The crystal lattice parameters were computed with the aid of the computer program TREOR. The crystal data for Co(II), Ni(II), Cu(II) and Cd(II) metal mixed-ligand compounds belong to the crystal system triclinic. The significant broadening of the diffraction patterns suggests that the particles are of nanometer dimensions. Scherrer's equation (eqn. 5) was applied to estimate the particle size of the coordination polymers.

$$D = \frac{K\lambda}{\beta \cos\theta} \qquad (5)$$

Table 5. X-ray diffraction crystal data of the compounds

Parameters	(1)	(2)	(3)	(4)
Mol. Wt.	408.72	645.67	413.34	462.20
Crystal system	Triclinic	Triclinic	Triclinic	Triclinic
a (Å)	7.34	8.53	9.02	3.47
b (Å)	10.05	9.00	8.53	6.37
c (Å)	11.96	10.98	13.75	7.51
α (°)	103.81	86.19	90.00	65.80
β(°)	117.00	65.09	52.67	110.31
γ(°)	82.44	59.21	120.74	62.92
Volume of unit cell (Å^3)	763.97	645.67	646.18	102.09
Particle size (nm)	35	60	23	56

Scanning electron microscopy

The scanning electron micrographs of the Co(II), Ni(II), Cu(II) and Cd(II) ternary coordination polymer prepared bysonication is illustrated in Figures (6-9). The micrograph shows the morphology of this nanostructured compounds. The nano crystals aggregate to a great extent in the form of cornel reefs for cadmium compound.

The particle size of the compounds are in the range 38-60 nm. These results are in a good agreement with the size determined from XRD analysis by the Scherrer's equation (Table 4).

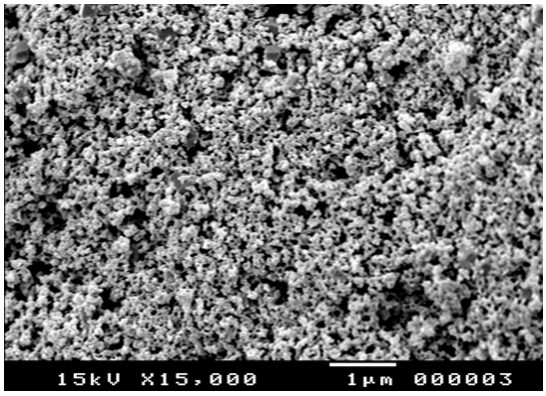

Figure 5. SEM picture of Cu(II) compound.

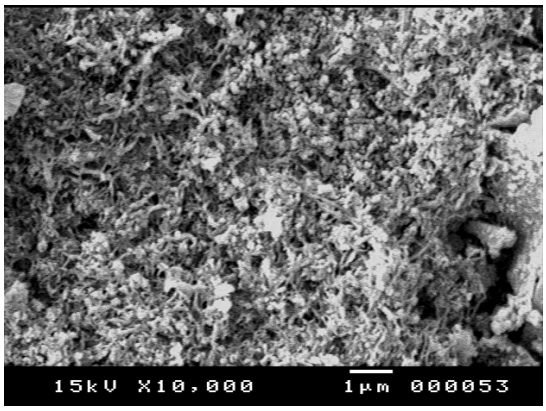

Figure 6. SEM picture of Ni(II) compound.

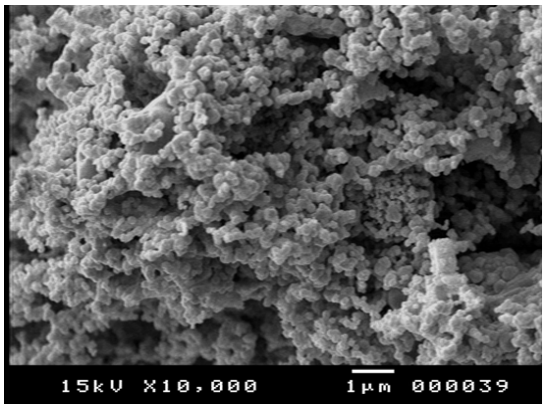

Figure 7. SEM picture of Co(II) compound.

Biological Activity

For testing the antibacterial and antifungal activity of these compounds we used more than one test organism to increase the chance of detecting the antibiotic property of the tested materials. The data showed that in some cases the ligand has a higher or similar antimicrobial and antifungal activity than the selected standards (chloramphenicol and clotrimazole). Also, the complexes of certain metal ions possessed enhanced antimicrobial activity and in some cases activity similar to the selected standards (Table 6).

Table 6. Microbiological screening of the compounds.

aMicrob	Compound			
	(1)	(2)	(3)	(4)
B. cereus (G+ve)	10	16	12	18
S. aureus (G+ve)	10	12	10	14
S. aureus (G-ve)	10	11	8	16
E. coli (G-ve)	10	12	11	18
P. aeruginosa (G-ve)	10	12	10	14
T. rubrum	8	8	10	12
A. flavus	0	0	0	10
C. albicans	8	0	0	12
F. oxysporm	0	8	0	10
G. candidum	10	0	11	18
S. brevicaulis	0	8	8	12

The toxic action of the prepared coordination polymers against the growth of bacteria and fungi studied may be due to thiols, which are the vital constituents in the living cells, having a reduction potential for disulfide form at or below -200 mV, may be oxidized by the metals complexes. The complexes may cause disturbance in the respiration process due to the presence of (C=S) group in the azole complexes.[30-32]

Conclusion

The results presented in this work showed that synthesis of nanosized metal (II) coordination polymers derived from 5-(3-pyridyl)-1,3,4-oxadiazole-2-thiole and 2-aminothiazole can be achieved via the sonochemical method. Some of the complexes show a remarkable biological activity against bacteria and fungi indicating that they can be as potential antibacterial or antifungal drugs.

References

[1]Batten, S. R., Murray, K. S., *Coord. Chem. Rev*., **2003**, *246*, 103.

[2]Zou, R. Q., Sakurai, H., Xu, Q., *Angew. Chem. Int. Ed*., **2006**, *45*, 2542-2546.

[3]Brammer, L., *Chem. Soc. Rev*., **2004,** *33*, 476-489.

[4]Sadeghzadeh, H., Morsali, A., Yilmaz, V., *Ultra. Sonochem*., 2010, *17*, 592-597.

[5]Zhang, Z. H., Tian, Y. L., Guo, Y. M., *Inorg. Chim. Acta*, **2007,** *360*, 2783-2788.

[6]Oae, S., *Organic Sulfur Chemistry*, CRC Press Boca Raton, U. S. A., **1992**.

[7]Maged. S. A.-F., Aref, A. M. A., Mahmoud, A. G., *Mater. Sci*., **2014**,*10*, 192,

[8]Aref, A. M. A., Mahmoud, A. G., Bahaa, M. A.-Z., Maged. S. A.-F., *J. Environ. Anal. Toxicol*., **2012**, *2*, 2.

[9]Wang, Y. T., Tang, G. M., Qiang, Z. W., *Polyhedron*, **2007**, *26*, 4542-455.

[10]Agarwal, N., Kumar, K., *Indian J. Het. Chem*., **1997**, *6*, 291

[11]Kwon-Chung, J., Bennett, J. E., *Medical Mycology*, Lea and Febiger, 1992, 866 p.

[12]Singh, M., Butcher, R. J., Singh, N. K., *Polyhedron*, **2008**, *27*, 3151-3159.

[13]Maurya, R. C., Verma, R., Singh, H., *Synth. React. Inorg. Met.-Org. Chem.*, **2003**, *33*, 1063-1066.

[14]Lane, T. J., Nakagawa, I., Walter, J. L., Kandathil, A., *J. Inorg. Chem*., **1962**, *1*, 267-270.

[15]Aly, A. A. M., El-Meligy, M. S., Zidan, A. S., El-Shabasy, M., *Anal. Quim*., **1990**, *86*, 19-23.

[16]Bravo, A., Anacona, J. R., *Trans. Met.* Chem. **2001**, *26*, 20-25.

[17]Rakha, T. H., *Synth. React. Inorg. Met.-Org. Chem.*, **2000**, *30*, 205-208.

[18]A. Bharti, M.K. Bharty, S. Kashyap, U.P. Singh, R.J. Butcher, N.K. Singh, Polyhedron 50 (2013) 582–591.

[19]Al-Jibouri, M. N., Hafidh, F. R., Rasheed, A. M., *Eur. Chem. Bull*., **2014**, *3(6)*, 559-562.

[20]Lever, A. B. P., *Inorganic Electronic Spectroscopy*, 2nd Ed., Elsevier Amsterdam, **1984**.

[21]El-Asmy, A. A., Mounir, M., *Transit. Met. Chem*., **1988**, *13*, 143-146.

[22]Anacona, J. R., Toledo, C., *Transit. Met Chem*., **2001**, *26*, 228-231.

[23]Coats, A., Redfern, J., *Nature*, **1964**, *20*, 68.

[24]Horowitz, H., Metzger, G., () *Anal. Chem*., **1963**, *35*, 1464.

[25]Mohamed, G. G., Hosny, W. M., Abd El-Rahim, M. A., *Synth. React. Inorg. Met.-Org. Chem*., **2000**, *32*, 1501-1519.

[26]Beg, M. A., Qaiser, M. A., *Thermochim. Acta*, **1998**, *210*, 123-132.

[27]Pandey, O. P., Sengupta, S. K., Tripathi, S. C., Rev. Inorg. Chem., **1985**, *96*, 155-167.

[28]Yusuff, K. M., Karthikeyan, A. R., *Thermochim. Acta*. **1992**, *207*, 193-199.

[29]Emam, M. E., Kanawy, M., Hafe, M. H., *J. Therm. Anal. Calorim*., **2001**, *63*, 75-83.

[30]Callan, A., (1957) *Proceedings of the Plant Protection Conference*, Butterworths, London, **1957**.

[31]Miller, O., Callan, S., *J. Agric. Food Chem*., **1957**, *5*, 1169.

[32]Anjaneyulu, Y., *Synth. React. Inorg. Met.-Org. Chem.*, **1986**, *16*, 257.

Received: 25.11.2016.
Accepted: 26.12.2016.

SYNTHESIS, CHARACTERIZATION, THEORETICAL STUDIES AND PHOTOSTABILIZATION OF MEFENAMIC ACID DERIVATIVE WITH SOME DIVALENT METAL IONS

Adil Ahmed A. Al-Dulimia[a]*, Rehab A. M. Al-Hasani[a] and Emad A. Yousif [b]

Keywords: Triazole; photochemistry; mefenamic acid metal complexes; UV light; photostabilization; semi-empirical calculations.

A new mefenamic acid derivative, (4-amino-5-(2-(2,3-dimethylphenyl)aminophenyl)-1,2,4-triazole-3-thion (**L**), has been synthesized and characterized by spectroscopic and elemental analysis. The ligand (**L**) has been used as a chelating agent to prepare complexes of Co(II), Ni(II), Cu(II), Zn(II) and Cd(II) ions. The structure of the complexes, in solid state, has been suggested. The theoretical treatment of the complexes, in the gas phase, has been studied using the Hyperchem-8 program for the molecular mechanics and semi-empirical calculations. The heat of formation (ΔH_f°) and binding energy (ΔE_b) for the ligand and their complexes were calculated by PM3 method. The electrostatic potential of the ligand (**L**) has been calculated to investigate the reactive sites of the molecule. Photostabilization of PVC film in air was investigated in the absence and presence of the ligand **L** and theirs complexes by accelerated weathering tester. It was found that various indices values increased with irradiation time and this increase depend on the type of additives.

* Corresponding Authors
Tel.: 009647507760299
E-Mail: adel80200999@yahoo.com
[a] Al-Mustansirya University, College of Science, Department of Chemistry, Baghdad, Iraq.
[b] Al-Nahrain University, College of Science, Department of Chemistry, Baghdad, Iraq.

Introduction

1,2,4-Triazole constitute an interesting group of heterocyclic compounds containing three N atoms in a 5-membered ring and its derivatives represent some of the most biologically active classes of compounds possessing a wide spectrum of biological and pharmacological properties.[1-6] There are known drugs containing the 1,2,4-triazole group e.g. Triazolam,[7] Alprazolam,[8] Etizolam and Furacylin.[9] N4-amino and 3-thione of 1,2,4-triazoles with substitution at 5-position have been studies as anti-inflammatory and antimicrobial agents.[10] An important and versatile class of well-established biologically active compounds are those with the –N-C=S moiety (" soft" sulfur atom besides the "hard" nitrogen). This group is found in many basic structures of drugs either to be part of an open chain, e.g. thiocarbamates, isothiocynates and thiosemicarbazides or involved in heterocyclic ring, e.g. mercapto derivatives of triazoles, oxadizoles and thiodiazoles.[11-13]

In this work, we report the preparation of 4-amino-5-(2-(2,3-dimethylphenyl) aminophnyl-1,2,4-triazole-3-thion (**L**) as a ligand, in an attempt to prepare a new ligand with a 4-amino-3-thione-1,2,4-triazole ring , substituted at 5-position with mefenamic acid residue, and to investigate the coordination behaviour of the prepared new ligand towards Co(II), Ni(II), Cu(II), Zn(II) and Cd(II) ions. Theoretical study, in the gas phase, by using semi-empirical method has been performed in order to show the most stable conformation and to compare these results with the experimental data. Also the prepared complexes of (**L**) were used to enhance the photostabilization of polymer polyvinyl chloride (PVC). The photostabilization activity of these compounds was determined by monitoring the carbonyl (I_{CO}), polyene (I_{PO}) and hydroxyl (I_{OH}) indices, weight loss method with irradiation time. It was found that the (I_{CO}), (I_{PO}) and (I_{OH}) indices values increased with irradiation time and this increase depend on the type of additives.[14,15]

Experimental

Instrumentation

Melting points were recorded on a Gallenkamp MF B600 010F melting point apparatus Elemental analyses were obtained using EA-034 for the ligand and their metal complexes. Metal contents of complexes were estimated spectrophotometrically using Flame atomic absorption Shimadzu-670 AA Spectrophotometer. Bruker Spectrophotometer model ultra-shield was used at 300 MHz for `H- and ^{13}C- NMR. IR spectra were recorded using FT-IR-8300 Shimadzu in the range of 4000-400 cm^{-1}. Electronic spectra were obtained using UV-1650PC-Shimadzu spectrophotometer at room temperature, the measurement were recorded using a solution of 10^{-3}M concentration of (**L**) ligand and its metal complexes in DMF as a solvent.

Magnetic susceptibilities of samples in the solid state were measured by using a Bruker BM6 magnetic balance. The molar conductivity was measured by using Electrolytic Conductivity Measuring set Model MC-1-Mark V by using platinum electrode (EDC 304) with cell constant (1 cm^{-1}), concentration (10^{-3} M) in DMF as solvent at room temperature.

Synthesis of ligand (L)

The ligand (**L**) was prepared starting from mefenamic acid (MFA) according to the following general steps can be seen on Scheme 1.[16-18]

Preparation of (2-(2,3-dimethyl phenyl)amino ethyl benzoate (G1)

Sulphuric acid (8 mL) was added dropwise with continuous stirring to a solution of MFA **(**0.1 mol) in 200 mL ethanol. The mixture was heated under reflux for 10 h. After cooling, the mixture was poured on to crushed ice, the precipitated crystalline solid was filtered, washed successively with water, 10% $NaHCO_3$ solution and water. The crude product was recrystallized from ethanol, to give compound **G1** as off white crystals, in 84 % yield, m. p. = 108-110 ˚C.

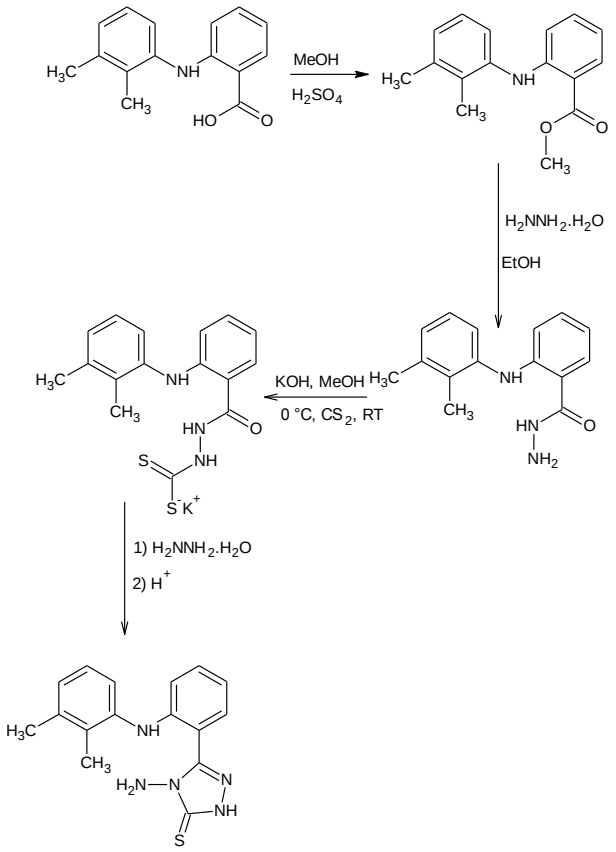

Scheme 1. Synthesis of the ligand **L**.

Preparation of(2-(2,3-dimethyl phenyl)amino ethyl benzohydrazide (G2)

Ester of **G1** (0.1 mol) was dissolved in absolute ethanol (50 mL). To the above solution was added 80 % hydrazine hydrate (0.1 mol). The resulting reaction mixture was refluxed on a steam bath for 10-12 h. After cooling, cold water (150 mL) was added to the mixture and the separated white crystalline solid was filtered, washed with cold water, dried and recrystallized from ethanol to give 82 % yield of **G2**, white colour, m p. 156-158 ˚C.

Preparation of (2-(2,3-dimethyl phenyl)amino ethyl benzoyl)hydrazine carbodithioate (G3)

Compound **G2** (0.05 mol) was treated with a solution of potassium hydroxide (0.0643 mol) in ethanol (70 mL) at 0˚C with stirring, then 7 mL of carbon disulfide was added dropwise and the reaction mixture was stirred overnight at room temperature. The solid product (**G3**) was filtered, washed with cold methanol and dried.

Preparation of 4-amino-5-(2-(2,3-dimethylphenyl)aminophenyl)-1,2,4-triazole-3-thion (L)

A mixture of compound **G3** (0.05 mol) and 80 % hydrazine hydrate (10 mL) was heated under reflux till the evolution of hydrogen sulphide completely ceases (about 6 h). After cooling, water (200 mL) was added and the mixture was neutralized with 10 % HCl and allowed to stand for three h. The separated crude product was filtered, washed with water, dried and recrystallized from ethanol to give 80 %)yield of compound **L**, as white powder with melting point 215-217 ˚C.

Preparation of metal complexes (A1–A5)

Suitable amounts of $Co(CH_3COO)_2.4H_2O$, $Ni(CH_3COO)_2.4H_2O$, $Cu(CH_3COO)_2.H_2O$, $Zn(CH_3COO)_2.2H_2O$ and $Cd(CH_3COO)_2.2H_2O$ were dissolved in ethanol and added to an ethanolic solution of **L** in 1:2 mole ratio of metal : ligand with stirring. The reaction mixture was heated under reflux for 4 h, during this time a precipitate was formed. The product was filtered off, washed with hot ethanol, followed by cold water and then dried under vacuum. All complexes were identified by elemental analysis, flame atomic absorption, FT-IR and UV-VIS spectroscopy, magnetic and conductivity measurements.

Computational methods

Four types of calculations, viz., single point, geometry optimization, vibrational frequency and bond length, were carried out, using Hyperchem-8, a sophisticated molecular modeler editor and powerful computational package. This program known for its quality, flexibility and ease of use, uniting 3D visualization and animation with quantum chemical calculations, mechanic and dynamic.[19,20] Hyperchem offers ten semi-empirical molecular orbital methods, with options for organic and main group compounds for transition metal complexes and spectral simulation.[21,22] We chose parameterization model version 3 (PM3) which including transition metals. PM3 were used for the calculation of heat of formation, binding energy, total energy and bond length for all metal complexes.

Photostabilization of polymer

Commercial PVC supplied by Petkim Company(Turkey) was re-precipitated from THF solution and finally dried under vacuum at room temperature for 24 h. Fixed concentrations of PVC solution (5 g 100 mL^{-1}) in THF were used to prepare polymer films with 40 μm thickness (measured by a micrometer type 2610 A, Germany). The films were prepared by evaporation technique at room temperature for 24 h.[6,23] To remove the possible residual THF solvent, film samples were further dried at room temperature for three h under reduced pressure. The films were fixed on stands specially used for irradiation. The stand is provided with an aluminium plate (0.6 mm in thickness) supplied by Q-panel company.

Irradiation experiments

Accelerated weatherometer Q.U.V. tester (Q. panel, company, USA), was used for irradiation of PVC films. The accelerated weathering tester contains stainless steel plate, which has two holes in the front side and a third one behind. Each side contains a lamp (type Fluorescent Ultraviolet Lights) 40 Watt each. These lamps are of the type UV-B 313 giving spectrum range between 290–360 nm with a maximum wavelength at 313 nm. The polymer film samples were vertically fixed parallel to the lamps to make sure that the UV incident radiation is perpendicular to the samples. The irradiated samples were rotated from time to time to ensure that the intensity of light incident on all samples is the same.

The degree of photodegradation of polymer film samples was followed by monitoring FT-IR spectra in the range 4000–400 cm^{-1} using FT-IR 8300 Shimadzu Spectrophotometer. The position of carbonyl absorption is specified at 1720 cm^{-1}, the hydroxyl group at 3450 cm^{-1} and 1604 cm^{-1} is due to polyene group. The progress of photodegradation during different irradiation times was followed by observing the changes in carbonyl and hydroxyl peaks. Then carbonyl and hydroxyl indices were calculated by comparison of the FTIR absorption peak at 1720, 3450 and 1604 cm^{-1} with reference peak at 1450 cm^{-1}, respectively. This method is called band index method which includes as shown in eqn. (1).

$$I_s = \frac{A_s}{A_r} \quad (1)$$

where

A_s= Absorbance of peak under study,

A_r = Absorbance of reference peak,

I_s = Index of group under study.

Actual absorbance, the difference between the absorbance of top peak and base line ($A_{\text{Top peak}} - A_{\text{Base line}}$) is calculated using the base line method.

Determination of average molecular weight using viscometry method

The viscosity property was used to determine the average molecular weight (M_{av}) of the polymer, using the Mark-Houwink relation (eqn. 2).

$$[\eta] = KM^{\alpha} \quad (2)$$

where

$[\eta]$ is the intrinsic viscosity,

K and α are constants depending upon the polymer-solvent.

The intrinsic viscosity of a polymer solution was measured with an Ostwald U-tube viscometer. Solutions were made by dissolving the polymer in a solvent (g 100 mL^{-1}) and the flow times of polymer solution and pure solvent are designated as t and t_0 respectively. Specific viscosity (η_{sp}) was calculated by eqns. (3) and (4).

$$\eta_{re} = \frac{t}{t_0} \quad (3)$$

where η_{re} = relative viscosity.

$$\eta_{sp} = \eta_{re} - 1 \quad (4)$$

The single-point measurements were converted to intrinsic viscosities by the eqn. (5).

$$[\eta] = \left(\sqrt{2/c}\right)\left(\eta_{sp} - \ln \eta_{re}\right)^{1/2} \quad (5)$$

where c = concentration of polymer solution in g 100 mL^{-1}).

By applying eqn. (5), the molecular weight of degraded and un-degraded polymer can be calculated. Molecular weights of PVC with and without additives were calculated from intrinsic viscosities measured in THF solutions using eqn. (6).

$$[\eta]=4.17x10^{-4}M_{av}^{0.6} \quad (6)$$

Results and discussion

Study of the complexes in solid state

The physical and analytical data of the ligand (**L**) and its metal complexes are given in Table 1. The results obtained from elemental analysis are in satisfactory agreement with the calculated values. The suggested molecular formula was also supported by spectral measurement as well as magnetic moment. The ligand **L** is soluble in common organic solvents such as (ethanol, acetone and methanol), whereas the new complexes are coloured crystalline solids, soluble in chloroform, DMF and DMSO.

The nuclear magnetic resonance spectra of **L** gave satisfactory spectra data and the molecular structure was assigned on the basis of ^{1}H-NHR spectrum. The spectra were obtained in DMSO-d_6 solution as an internal reference. According to the results obtained from the spectrum (Figure 1), the molecular structure of the ligand can be illustrated $\delta H_{(1,2)}$ = 2.095-2.281 ppm (6H, s, CH_3), $\delta H_{(3)}$ = 5.3 ppm (2H, s, NH_2), $\delta H_{(4)}$ = 9.47 ppm (1H, s, NH), $\delta H_{(5)}$ = 12.41 ppm (1H, s, NH), δPh = 6.706-7.89 ppm (7H).

Table 1. Physical data for Ligand (**L**) and its metal complexes (**A1**-**A5**).

Comp. No.	Color	M. P.	Yield %	Analysis found/calculated					Suggested formula
				C%	H%	N%	S%	M%	
L	White	215-	80	61.73	5.47	22.51	10.29	-	$(C_{16}H_{17}N_5S)$
A1	Brown	234d	90	54.07	5.01	17.52	8.01	7.37	$[Co(C_{32}H_{34}N_{10}S_2)(CH_3COO)_2]$
A2	Yellowish	260d	78	54.09	5.01	17.53	8.01	7.35	$[Ni(C_{32}H_{34}N_{10}S_2)(CH_3COO)_2]$
A3	Dark green	250d	88	53.	4.98	17.42	7.97	7.90	$[Cu(C_{32}H_{34}N_{10}S_2)](CH_3COO)_2$
A4	Off white	200d	90	53.64	4.97	17.38	7.95	8.12	$[Zn(C_{32}H_{34}N_{10}S_2)](CH_3COO)_2$
A5	Off white	270d	85	50.62	4.69	16.40	7.49	13.17	$[Cd(C_{32}H_{34}N_{10}S_2)](CH_3COO)_2$

Table 2. Stretching vibrational frequencies (cm^{-1}) located in the FT-IR spectra of (**L**) and their metal complexes.

Comp. No.	$\nu_{C=S}$	$\nu_{C=N}$	νNH_2 (as,s)	ν_{NH}	ν_{COO^-} (as,s)(coord.)	ν_{COO^-} uncoord.	M-N	M-S	M-O
L	1041	1643	3269,3209	3439	-	-	-	-	-
A1	1020	1640	3252,3212	3441	1537, 1305	-	530	459	523
A2	1030	1643	3263,3211	3440	1512, 1302	-	532	457	540
A3	1030	1640	3252,3200	3439	-	1665	529	460	-
A4	1022	1640	3252,3194	3440	-	1655	530	455	-
A5	1030	1645	3240,3155	3442	-	1660	533	454	-

The ^{13}C-NMR spectrum for **L** showed the following peaks. $C_{(1)}$ = 169.615, $C_{(2)}$ = 161, $C_{(3)}$ = 148, $C_{(4)}$ = 138, $C_{(5)}$ = 137, $C_{(6)}$= 134, $C_{(7)}$ = 131.64, $C_{(8)}$ = 131.17, $C_{(9)}$ = 126.18, $C_{(10)}$ = 125.94, $C_{(11)}$ = 122.13, $C_{(12)}$ = 116.55, $C_{(13)}$ = 113.02, $C_{(14)}$ = 111.29, $C_{(15)}$ = 20.16, $C_{(16)}$ = 14.37 (Figure 2).

The characteristic stretching vibration modes concerning **L** and its metal complexes (**A1 – A5**) are presented in Table 2. In all complexes (A_1-A_5), the ligand (L) behave as a bidentate coordinating with metal through sulfur of thiocarbonyl and nitrogen of amino group, therefore the bands due to $\nu_{(C=S)}$, (ν_s and ν_{as} of NH_2) and four (I-IV) thioamide bands were shifted to a lower frequency as it can be seen in Table, as well as the new bands for complexes (A_1 and A_2) in the region of 1521, 1537 cm^{-1}, which may be assigned to the asymmetric vibration of coordinated carboxylate groups ($\nu_{as}coo^-$) and the bands in the region of 1302-1305v cm^{-1} may be attributed to the symmetric vibration of carboxylate group ($\nu_s coo^-$).[24, 25]

The large differences between the frequencies of [$\nu_{as}(coo^-)$] and [$\nu_s(coo^-)$], (Δv>200cm^{-1}) in (**A1**) and (**A2**) complexes are indicative of the involvement of the coordination of the carboxylate groups to the metal ion in a monodentate fashion.[24,26] In contrast to (**A1**) and (**A2**) complexes, the complexes (**A3**), (**A4**) and (**A5**) show appearance of new bands in the region of 1655-1665 cm^{-1} which may be assigned to the vibration of uncoordinated carboxylate groups. Other low intensity bands observed in the region of 445-460, 518-520 and 523-544 cm^{-1} may be attributed to ν_{M-S} and ν_{M-N} respectively, in the all complexes and ν_{M-O} in the case of (**A1**) and (**A2**) complexes, respectively.[26,27]

The electronic spectra of the free ligands (**L**) and their complexes (**A1**– **A5**) were recorded in chloroform solution. The spectrum of **L** shows a strong band at 42194 cm^{-1}, which is attributed to $\pi\rightarrow\pi^*$ and others at 31545, 29411 cm^{-1}, due to $n\rightarrow\pi^*$.

The measured magnetic moment of A**1** is 4.2 B.M, this indicated that the cobalt ion in the complex is typical of d^7 system with three unpaired electrons indicating a quartet state and suggest high spin octahedral geometry. The electronic spectrum of **A1** in chloroform exhibited two bands at 15384 and 18691 cm^{-1}, assignable to $^4T_1g\rightarrow{}^4A_2g_{(F)}$ and $^4T_1g\rightarrow{}^4T_1g_{(P)}$ transitions respectively for an octahedral geometry of Co(II). The value of various ligand filed parameters ν_1, B^-, β and Dq have been calculated using Tanabe-Sugano diagram for d^7 system and found to be 7039.9, 623,0.642 and 934.5 respectively. The molar conductivity measurement in DMF showed that the complex is non electrolyte (Table 3).

The light green **A2** complex in chloroform exhibited bands at 15267 and 25974 cm^{-1} assigned to $^3A_2g\rightarrow{}^3T_1g_{(F)}$ (ν_2) and $^3A_2g\rightarrow{}^3T_1g_{(P)}$ (ν_3) transitions respectively, which indicate octahedral geometry of Ni(II). The absence of any band below 10000 cm^{-1} eliminates the possibility of tetrahedral environment in this complex. The different ligand field parameters B^-, β and Dq have been calculated using the same diagram and found to be 611, 0.54 and 1099.224 respectively indicating that Ni-**L** bond is covalent. Magnetic moment, 3.09 B.M, of the solid complex showed a higher orbital contribution. Conductivity measurement in DMF showed that the complex was nonionic.

Table 3. Electronic spectra, magnetic moment and conductance in for the metal complexes

Symb.	λ_{max} cm^{-1}	Band assignment	10Dq	Molar Cond. $S.cm^2.mol^{-1}$	μeff. B.M	Suggested geometry
A1	7039.9 (Cal.) 1538.4 1869.1	$^4T_1g \rightarrow {}^4T_2g_{(F)}$ $^4T_1g \rightarrow {}^4A_2g_{(F)}$ $^4T_1g \rightarrow {}^4T_1g_{(P)}$	9337.6	15.65	4.2	OC-6
A2	10992.24 (Cal.) 15267 25974 33112	$^3A_2g \rightarrow {}^3T_2g_{(F)}$ $^3A_2g \rightarrow {}^3T_1g_{(F)}$ $^3A_2g \rightarrow {}^3T_1g_{(P)}$ C.T	10976	18.09	3.09	OC-6
A3	14084 25773	$^2B_1g \rightarrow {}^2A_1g$ $^2B_1g \rightarrow {}^2B_2g + {}^2Eg$	-	168.22	1.92	SP-4
A4	32258 38167 47619	ILCT	-	166.86	0.0	T-4
A5	31055 34482 47169	ILCT	-	170.9	0.0	T-4

The measured magnetic moment of **A3** is 1.92 B.M showing that the Cu(II) ion in the dark green complex is a d^9 system. Electronic spectrum in chloroform, shows one broad band at 14084cm^{-1} which corresponds to $^2B_1g \rightarrow {}^2A_1g$ transition, and a shoulder band at 25773cm^{-1} which is assigned to $^2B_1g \rightarrow {}^2B_2g + {}^2Eg$ transition. The position of these bands is in a good agreement with that reported for highly distorted octahedral geometry. Conductivity measurement in DMF showed that the complex was highly ionic.

The two complexes (**A4**) and (**A5**) are colourless in chloroform solution, so there is no d-d transition in the visible region, The complexes are diamagnetic as is expected for d^{10} ions. The conductivity measurements indicate ionic behaviour of the complexes.

Stereochemical structure of the complexes

According to the results obtained from the elemental analysis, spectral studies, magnetic and conductivity measurements, the suggested general structure of the complexes (**A1–A2**) can be illustrated as Figure 3. The Complexes **A3** and **A4** has tetrahedral and **A5** square-planar structure with the same coordination sites of the ligand **L**.

Theoretical studies of the ligand and their metal complexes

The electrostatic potential (EP) describes the interaction of energy of the molecular system with a positive point charge. EP is useful for finding sites of reaction in a molecule. Positively charged species tend to attack a molecule where the electro static potential is strongly negative (electrophonic attack). The EP of the free ligand was calculated and plotted as 3D and 2D contour to investigate the reactive sites of the molecules (Figure 4). The results of calculations show that the LUMO of transition metal ions prefer to react with the HOMO of sulfur and nitrogen atoms of the free ligand.

The conformations of the free ligand and its complexes obtained from the semi-empirical and molecular mechanics calculations that were fully re-optimized to estimate the heat of formation (ΔH_f^o) and binding energy (ΔE_b) by using the PM3 method for free ligand (**L**) and its metal complexes (Table 4).

The vibrational spectra of (**L**) and its metal complexes have been calculated (Supplementary Material). The theoretically calculated wave numbers showed that some deviations from the experimental values but these deviations are within the generally acceptable limits in theoretical calculations.[28]

The Gaussian suite of software was employed throughout this study for bond length measurements. Optimizations were carried out for the model systems represented in the Supplementary Material. The initial state for structure did not give bond lengths naturally so that the geometry optimization was used for correct bond lengths. Calculation parameters were optimized of bond lengths for the free ligand and its metal complexes by using the semi-empirical PM3 method, at geometry optimization of 0.001 kcal mol^{-1}, to give excellent agreement with the experimental data,[29] as it shown in Table 5.

Photostabilization study

The complexes of Co(II), Cd(II), Ni(II), Zn(II) and Cu(II) with (**L**) were used as additives for the photostabilization of PVC films. To study the photochemical activity of these additives for the photostabilization of PVC films, the carbonyl, hydroxyl and polyene indices were monitored with irradiation time using IR spectrophotometry.

The irradiation of PVC films with UV light of wavelength λ=313 nm led to a clear change in the FT-IR spectrum. The appearance of bands in 1720 cm^{-1} has been attributed to the formation of carbonyl groups related to aliphatic ketone. The hydroxyl band that appeared at 3450 cm^{-1} was annotated to the hydroxyl group and 1604 cm^{-1} is due to polyene group.[30] The absorption of the carbonyl, hydroxyl and polyene groups was used to follow the extent of polymer degradation during irradiation. This absorption was calculated as carbonyl index (Ico), hydroxyl index (I_{OH}) and polyene index (I_{PO}).

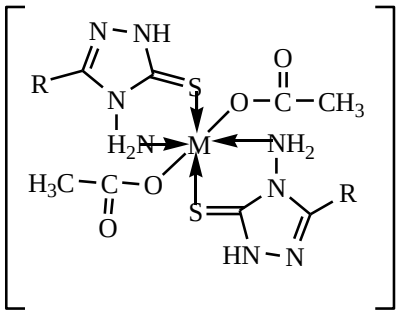

Figure 3. Suggested structure of the complexes A1 and A2.

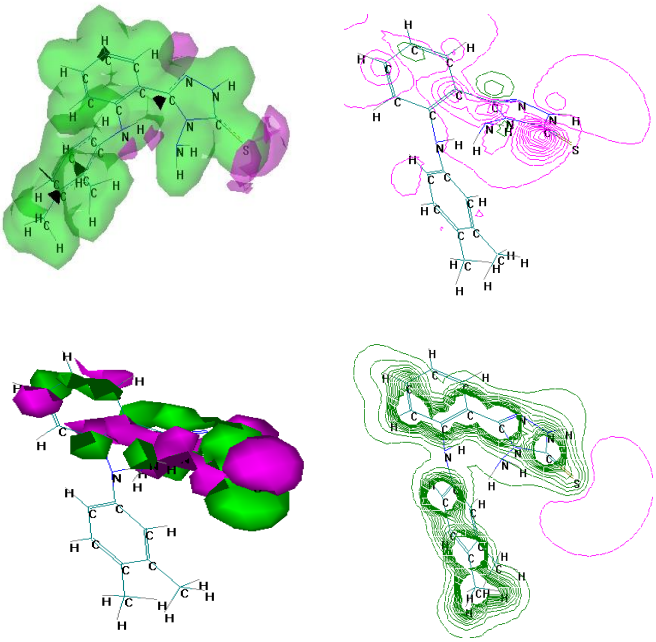

Figure 4. HOMO and LUMO 3D (a) and 2D (b) and electrostatic potential 3D (c) and 2D (d) contours for **L**.

Table 4. Conformation energetic (in kJ mol^{-1}) for the ligand and its metal complexes.

Compound	PM3	
	ΔH^{o}_{f}	ΔE_{b}
L	532.958	-17237.78
A1	-82634.277	-241013.37
A2	-781.116	-41912.129
A3	211.67	-35667.124
A4	855.52	-34816.181
A5	1005.164	-34647.978

It is reasonable to assume that the growth of carbonyl index is a measure to the extent of degradation. However, in Figure 6, the Ico of **L>A3>A4>A5>A1>A2** showed lower growth rate with irradiation time with respect to the PVC control film without additives.

Table 5. Selected bond lengths (A^0) for ligand (**L**) and its metal complexes.

Compounds	C=S	N-NH$_2$	M-S	M-N	M-O
L	1.634	1.430	-	-	-
A1	1.758	1.821	2.277	1.873	1.373
A2	1.762	1.488	2.284	1.882	1.282
A3	1.732	1.870	2.468	2.132	-
A4	1.771	2.754	2.137	1.8457	-
A5	1.751	3.345	2.270	1.956	-

Because the growth of carbonyl index with irradiation time is lower than PVC control, as seen in figure 7, it is reasonable to conclude that these additives might be considered as photostabilizers of PVC polymer. Efficient photostabilizer shows a longer induction period. Therefore, the **A2** is the most active photostabilizer, followed by **A1**, **A5**, **A4**, **A3**, and **L** which is the least active. Just like carbonyl, hydroxyl and polyene compounds are also produced during photodegradation of PVC. Therefore, I_{OH} and I_{PO} could also be monitored with irradiation time in the presence and absence of these additives. Results are shown in Figures 7 and 8.

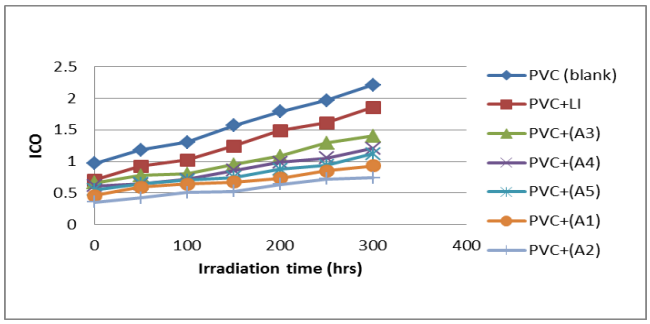

Figure 6. Relationship between the I_{CO} and irradiation time of PVC films of 40 μm thickness.

The photodegradation of PVC is commonly known to be accompanied by a dehydrochlorination process (the evolution of HCl gas) consequently, weight loss occurs, which increases with increasing irradiation time. The stabilizing efficiency was determined by measuring the % weight loss of photodegraded PVC films in the absence and in the presence of additives. The weight loss percentage as a function of the irradiation time can be used as a good measure of the degree of degradation and consequently can measure the stabilizing potency of the stabilizer and how long that stabilizer would protect the polymer.[31] The results of the weight loss as a function of the irradiation time is shown in Figure 9. The results clearly showed the low extent of weight loss (i.e., the low extent of dehydrochlorination as evolved HCl is the main degradative product) of photodegraded PVC stabilized by the complexes of (**L**) in comparison with the weight loss of photodegraded unstabilized PVC. The stabilizing efficiency of the investigated photostabilizers was found to follow the order: PVC >**L>A3>A4>A5>A1>A2**.

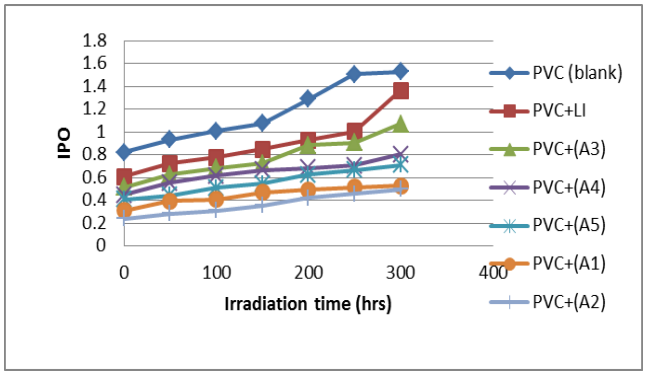

Figure 7. Relationship between the I_{po} and irradiation time of PVC films (40 µm) thickness containing 0.5 % additives.

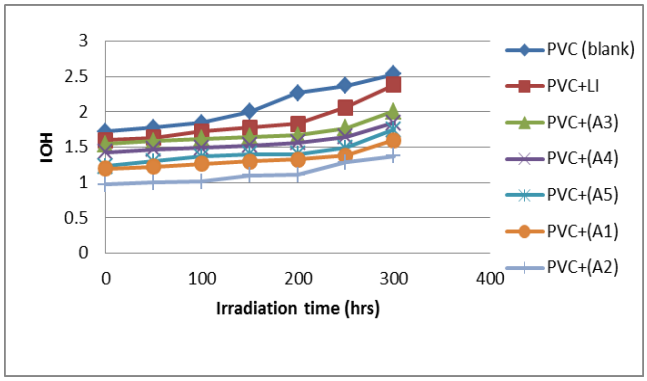

Figure 8. Relationship between the I_{OH} and irradiation time for PVC films of 40 µm thickness.

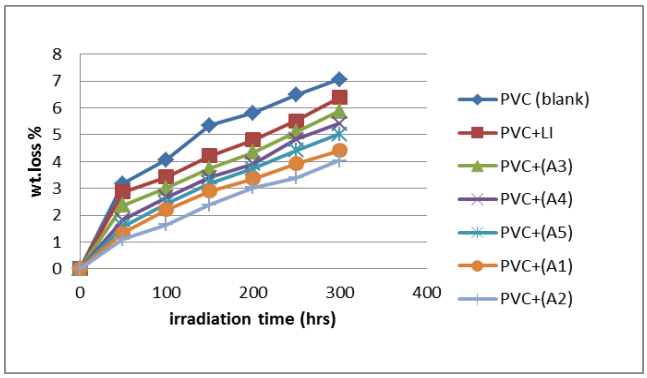

Figure 9. Variation of the weight loss of PVC films of 40 µm thickness with the irradiation time.

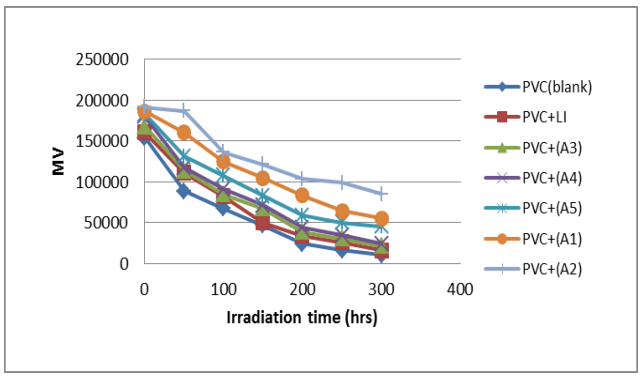

Figure 10. Variation of the viscosity average molecular weight with irradiation time of PVC films of 40 µm thickness.

The analysis of relative changes in viscosity–average molecular weight (*M*av) has been shown to provide a versatile test for random chain scission. Figure 10 shows the plot of (*M*av) versus irradiation time, with absorbed light intensity of 1.052×10^{-8} ein dm^{-3} s^{-1}, for PVC film with and without 0.5% (wt/wt) of the selected additives. *M*av is measured using eqn. (3) with THF as a solvent at 25 ^{0}C. It is worth mentioning that traces of the films with additives are not soluble in THF, indicating that crosslinking or branching in the PVC chain does occur during the course of photolysis.[30,32] For better support of this view, the number of average chainscission (*S*; average number cut per single chain) was calculated using eqn. (7).

$$S = \frac{M_{av,0}}{M_{av,t}} - 1 \qquad (7)$$

where $M_{av,o}$ and $M_{av,t}$ are viscosity–average molecular weights at initial (zero) and at irradiation time (t), respectively. The plot of *S* versus time is shown in Figure 11. The curve indicates an increase in the degree of branching such as that might arise from crosslinking occurrence. It is observed that insoluble material was formed during irradiation, which provided an additional evidence to the idea that crosslinking does occur.

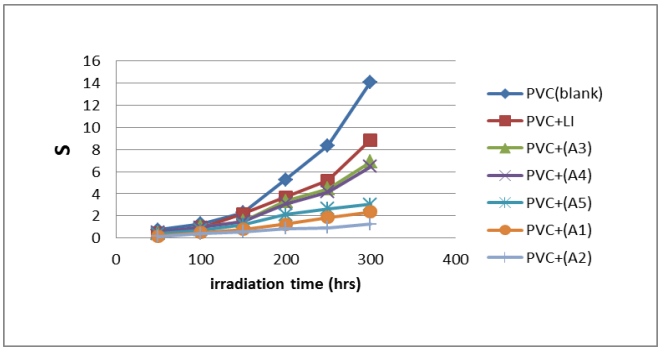

Figure 11. Changes in the main chain scission (*S*) during irradiation of PVC films of 40 µm thickness.

For randomly distributed weak bond links, which rapidly break in the initial stages of photodegradation, the degree of deterioration α is given by eqn.(8).

$$\alpha = \frac{mS}{M_{av}} \qquad (8)$$

where *m* is the initial molecular weight.

The plot of α as a function of irradiation time is shown in Figure 12.The values of α of the irradiated samples are higher when additives are absent and lower in the presence of additives when compared with the corresponding values of the additive-free PVC. In the initial stages of photodegradation of PVC, the value of α increase rapidly with time; these indicators indicate a random breaking of bonds in the polymer chain.

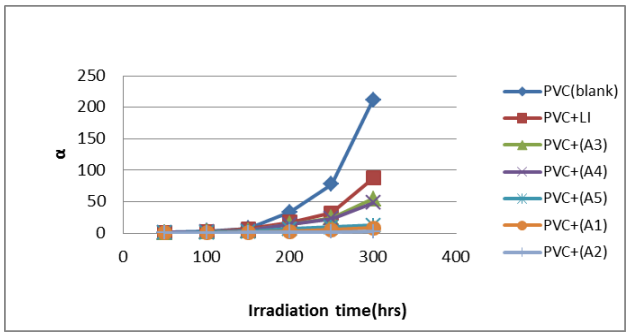

Figure 13. Changes in the degree of deterioration (α) during irradiation of PVC films of 40 μm thickness.

Mechanism of the photostabilization

Depending on the overall results obtained, the efficiency of the complexes as stabilizer for PVC films can be arranged according to the changes in the carbonyl and hydroxyl concentration as a reference for comparison and the efficiency is **A2**>**A1**>**A5**>**A4**>**A3**>**L**. Metal chelate are generally known as photostabilizers for PVC through both peroxide decomposer and excited-state quencher. Therefore, it is expected that these complexes act as peroxide decomposer (Scheme 2).[30,32] The ring of benzothiazol in this compound plays an important role in the mechanism of stabilizing process by acting as UV absorber. The UV light absorption by these additives containing benzothiazol dissipates the UV energy to harmless heat energy (Scheme 3). This mechanism is in agreement with that reported ones.[32,33]

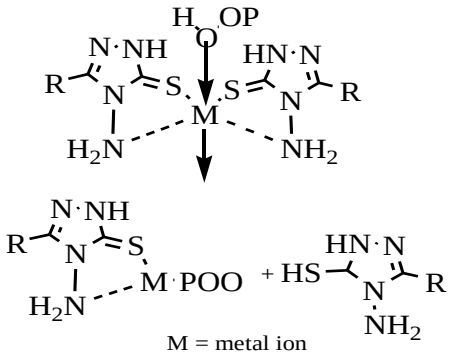

Scheme 2. Suggested mechanism of photostabilization of complexes as peroxide decomposer.

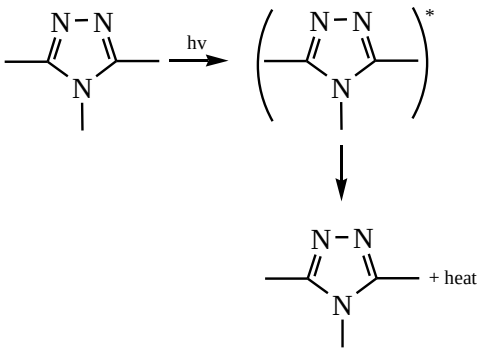

Scheme 3. Suggested mechanism of photostabilization of triazole as UV-absorber.

References

[1]Jones,D. H., Slack, R. S.,Woolridge, K. R. H., *J. Med. Chem.*, **1965**, *8*, 676.

[2]Goswami, B. N., Katiki, J. C. S., Baruah, J. N., *J. Heterocyclic Chem.*, **1984**, *2*, 225.

[3]Holla, B. S., Kallurya, B., Sridhar, K. R., *Current Sci*., **1987**, *56*, 236.

[4]Abdon, N. A., Amin, F. M., Mansura. A, J., *Pharm. Sci*., **1990**, *6*, 25.

[5]Mishra, R. K., Tiwari, R. K., Srivastava, S. K., Bahel, S. C., *J. Indian Chem. Soc*., **1991**, *68*, 110.

[6]Street, L. J., Baker, R., Baker, W. B., Davey, W. B., Guibin, A. R., Jelley, R. A., *J. Med. Chem.*, **1995**, 38, 1799

[7]Brucato, A. , Coppola, A. , Gianguzza, S., Provenzano, P. , *Boll. Soc. Ital. Biol. Sper*., **1978**, *54*, 1051-1057.

[8]Raslan, M. A., Khalil, M. A., *J. Heteroatom Chem*., **2003**, *14*, 114-120.

[9]Singha, T., Singh, J., Naskar, A., Ghosh, T., Mondal, A., Kundu, M., Harwansh, R. K., Maity, T. K., *Indian J. Pharm. Educ. Res*., **2012**, *46 (4)*, 346-351.

[10]Awad, I., Abdel-Rahman, A., Bakite, E., *J. Chem. Technol. Biotechnol*., **2008**, *51*, 483–486.

[11]Guveli, S., Ulkuseven, B., *Polyhedron*, **2011**, *30 (8)*, 1385-1388.

[12]Alagöz, C. D., Brauer, J., Mohr F., *J. Organomet. Chem*., **2009**, *694*, 1283-1288.

[13]Jaiswal, N., Singh, A. K., Singh, D., Ahmad, T, Int. Res. J. Pharm., **2012**, *3(3)*, 83–89

[14]Grassie, N., Scott, G., *Polymer Degradation and Stabilization*, Cambridge University Press, London, UK, **1985.**

[15]Andrady, A. L., Hamid, S. H., Hu, X., Torikai, A., *J. Photochem. Photobiol.B*., **1988**, *46*. 96–103.

[16]Boehner, B., Dawes, D., Meyer, W., Sturm, E., DE2500485, 1975.

[17]Mahajan, D. P., Bendre, R. S., *J. Drug Design Discov,*, **2011**, *2(2)*, 464.

[18]Mandal, V., Sen, S. K., Mandal, N., *Indian J. Microbiol*., **2011**, *51*, 22-29

[19]Stewart, J. J., Lipkowitz, K. B., Boyd, D. B., (eds.), *Reviews in Computational Chemistry*, John Wiley & Sons, **1996**, 72-80.

[20]Cook, D. B., *Handbook of Computational Quantum Chemistry*, Oxford University Press, Oxford, **1998**, 149.

[21]Choinacki, H., Pruchnik, F., *Int. J. Mol. Sci*., **2001**, *2(44)*, 11-17.

[22]Nahari, T. T., ISESCO Sci. Tech. Vision, **2007**, *3(3)*, 32-40.

[23]Rabek, J. F, *Photostabilization of Polymers:Principles and Application*, Elsevier, England, 19990.

[24]Silvertein, R., Bassler, G., *Spectrometric identification of organic compounds*, 5th Edition, John Wiley & Sons, New York, **1980**.

[25]Sliverstein, R., Bassler, G., Morrill, T., *Spectrometric Identification of Organic Compounds*, 7th Edition, John Wiley & Sons, New York, **2005**.

[26]Nakamoto, K., *Infrared and Raman Spectra of Inorganic and Coordination Compounds*, 6th Edition, JohnWiley & sons, New York, **1997**.

[27]Qurban, S., *J. Pure Sci*., **2011**, *7 (2)*, 94–104.

[28]Thakar, A. S., Simgh, K .K., Joshi, K. T., *Eur. J. Chem*., **2010**, *1*, 1396-1406.

[29]Atlas, M. R., Alfres, E., Alfres, B., Lawrence, C. P., *Laboratory manual. Experimental Microbiology*, Mosby- Year Book, Inc., **1995**.

[30]Yousif, E. A., Aliwi, S. M., Ameer, A. A., Ukal, J.R., *Turk. J. Chem*., **2009**, *33*, 39–410.

[31]Yousif, E., Salimon, J., Salih, N.,. *Arabian J. Chem*., **2014**, *7*, 306-311.

[32]Gugumus, F., *Mechanism of Polymer Degradation and Stabilization*, Elsevier, Amsterdam, **1990**.

[33]Adil, H., Yousif, E., Salimon, J., *New Stabilizers for PVC Based on Benzothiazole Complexes*, LAMBERT Academic Publishing, Germany, **2011**.

Received: 03.10.2016.
Accepted: 26.12.2016.